Effective Interactions, Global Dynamics and Cluster Formation in Protein Solutions

Dissertation

der Mathematisch-Naturwissenschaftlichen Fakultät

der Eberhard Karls Universität Tübingen

zur Erlangung des Grades eines

Doktors der Naturwissenschaften

(Dr. rer. nat.)

vorgelegt von

Michal Katharina Braun

aus Tübingen

Tübingen

2018

Gedruckt mit Genehmigung der Mathematisch-Naturwissenschaftlichen Fakultät der Eberhard Karls Universität Tübingen.

Tag der mündlichen Qualifikation: 23. 07. 2018

Dekan: Prof. Dr. Wolfgang Rosenstiel

1. Berichterstatter: Prof. Dr. Frank Schreiber

2. Berichterstatter: PD Dr. Fajun Zhang

Contents

Deutsche Zusammenfassung

Proteine in Lösung wechselwirken über verschiedene Mechanismen. Beispiele sind Van-der-Waals-Wechselwirkungen, Coulomb-Wechselwirkungen sowie hydrophobe Wechselwirkungen. Desweiteren können sich Proteine über Ionenbrücken oder kovalente Bindungen verbinden. Die mikroskopischen Wechselwirkungen manifestieren sich in einem makroskopisch beobachtbaren Phasenverhalten. Ein aktuelles Forschungsfeld stellen Systeme mit konkurrierenden Wechselwirkungen dar. Eine konkurrierende Wechselwirkung setzt sich aus einem kurzreichweitigen attraktiven Teil und einem langreichweitigen repulsiven Teil zusammen. Diese Kombination von Attraktion und Repulsion kann zu Cluster-Bildung führen.

In der vorliegenden Arbeit wird ein Modellsystem untersucht, das aus dem globulären Protein Rinderserumalbumin (BSA) und einem trivalenten Salz in wässriger Lösung besteht. In diesem System werden die effektiven Wechselwirkungen sowie die Cluster-Bildung untersucht. Die Cluster-Bildung wird weiterhin in β-lactoglobulin (BLG) - Lösungen studiert. Dieses System dient auch dazu, eine neue Methodik zu entwickeln, die statische und dynamische Messmethoden kombiniert.

Lösungen mit BSA und einem trivalenten Salz zeigen ein sogenanntes "reentrant condensation (RC)" Phasenverhalten[1;2]. Ins Deutsche übersetzt bedeutet "reentrant condensation" wiedereintretende Kondensation. Dieser Begriff ist allerdings irreführend. RC bedeutet, dass bei konstanter Proteinkonzentration c_p die Proben erst klar sind, dann trüb und schließlich wieder klar werden, wenn man die Salzkonzentration c_s erhöht. Das Phasendiagramm kann demnach in drei Regimes unterteilt werden.

Messmethoden, die die Proteindynamik erkunden, erfordern teilweise die Verwendung von schwerem Wasser, D_2O, als Lösungsmittel. Der erste Teil der Arbeit befasst sich deshalb mit dem Einfluss des Lösungsmittelisotops auf das Phasenverhalten der Proteinlösungen. Die makroskopische Erscheinung von BSA-Lösungen mit $LaCl_3$ in H_2O und D_2O bei Raumtemperatur ist in Abb. 4.1 zu sehen. In D_2O ist c^{**} zu höheren Salzkonzentrationen verschoben und damit Regime II breiter. Weiter zeigen in D_2O einige Lösungen Flüssig-Flüssig-Phasentrennung (LLPS) während in H_2O bei Raumtemperatur keine LLPS zu finden ist. Diese Beobachtungen deuten auf eine stärkere effektive Attraktion in D_2O hin. Die Veränderung der kritischen Temperatur mit steigendem D_2O-Lösungsmittelanteil ist in Abb. 4.2 zusammengefasst. Abb. 4.2a zeigt die Absorbanz für 80 mg/ml BSA und 13 mM $LaCl_3$ mit verschiedenen D_2O-Lösungsmittelanteilen bei steigender Temperatur. Abb. 4.2c zeigt die aus den Absorbanzkurven ermittelten Werte für die kritische Temperatur bei steigendem D_2O-Lösungsmittelanteil. Im experimentell zugänglichen Bereich sinkt die kritische Temperatur linear mit steigendem D_2O-Lösungsmittelanteil. Die kri-

tische Temperatur für den höchsten D_2O-Lösungsmittelanteil lässt vermuten, dass bei höherem D_2O-Lösungsmittelanteil das Verhalten nicht mehr linear ist. Um die Wechselwirkungen zwischen den Proteinmolekülen zu quantifizieren, wurden Klein-Winkel-Röntgenstreuungs-Messungen (SAXS-Messungen) durchgeführt. Die gemessene Intensität ist in Abb 4.3 zusammen mit Modell-Fits aufgetragen. Die Modell-Fits basieren auf dem Sticky-Hard-Sphere (SHS) Potential (siehe Gleichung 4.1). Die deutsche Bedeutung von *Sticky-Hard-Sphere* ist "klebrige harte Kugel". Der Klebrigkeitsparameter τ steht mit dem zweiten Virialkoeffizienten B_2 in Beziehung (Gleichung 4.2). Die sich ergebenden reduzierten zweiten Virialkoeffizienten B_2/B_2^{HS} werden in Abb. 4.4 gezeigt. B_2^{HS} ist der zweite Virialkoeffizient einer harten Kugel. Die Vermutung einer stärkeren Attraktion in D_2O wird durch diese Ergebnisse bestätigt. Die B_2/B_2^{HS}-Werte in D_2O sind, verglichen zu den Werten in H_2O, nach unten verschoben. Zusätzlich zum System mit BSA und $LaCl_3$ wurde der Isotopeneffekt im System mit BSA und YCl_3 untersucht (Abb. 4.5). Auch in diesem System steigt c^{**} mit zunehmendem D_2O-Lösungsmittelanteil. Bis zu einem D_2O-Lösungsmittelanteil von 0.6 wird LLPS beoachtet. Darüber wird keine LLPS mehr beobachtet. In diesem Fall ist die Attraktion zu stark für LLPS.

Im vierten Teil der Arbeit wird der Einfluss zweier Anionen auf das Phasenverhalten von BSA Lösungen mit trivalentem Salz verglichen. Die untersuchten Anionen sind NO_3^- und Cl^-. Der makroskopisch beobachtbare Effekt des Austauschs von Cl^- mit NO_3^- ist in Abb. 7.1 dargestellt. Die Phasendiagramme von BSA mit YCl_3 und $LaCl_3$ werden weiter unten diskutiert. Abb. 7.1b zeigt das makroskopische Erscheinungsbild von Lösungen mit BSA und $La(NO_3)_3$. Verglichen mit dem Phasendiagramm von BSA und $LaCl_3$ ist das zweite Regime in BSA mit $La(NO_3)_3$ breiter. Zudem fällt auf, dass die RC nur noch bei niedrigen Konzentrationen auftritt. In BSA mit $La(NO_3)_3$ ist bei Raumtemperatur auch ein LLPS Bereich zu finden. Das makroskopisch beobachtbare Verhalten wird durch SAXS Messungen, die Aufschluss über die mikroskopischen Wechselwirkungen geben, bestätigt (Abb. 7.5). Mit $La(NO_3)_3$ sind die Wechselwirkungen allerdings schwach genug, dass mit Hilfe von UV-vis Spektroskopie nach Zentrifugation der Proben ein Ansteigen der Proteinkonzentration in der dünnen Phase beobachtbar ist (Abb. 7.2). Obwohl NO_3^- und Cl^- in der Hofmeisterreihe nahe beieinander stehen, stellt sich also heraus, dass sich die effektive Attraktionsstärke stark unterscheidet, wenn NO_3^- anstelle von Cl^- verwendet wird.

Proteinclusterbildung in einem reinen Proteinsystem (β-Lactoglobulin, BLG) ohne zusätzliches Salz wird im zweiten Teil der Arbeit behandelt. Statische und dynamische Methoden werden auf eine neue Art und Weise kombiniert. Außerdem wird das "Self-crowding" von BLG studiert. Biochemische Reaktionen in der Zelle finden bei hoher Makromolekülkonzentration statt. "Crowding" ahmt diese hohen Makromolekülkonzentrationen nach. Der Begriff "crowding" bezeichnet das Zusammenrücken der Moleküle bei hohen Konzentrationen. "Self-crowding" meint das Zusammenrücken wenn nur eine Molekülart vorhanden ist. Abb. 5.1 zeigt SAXS Streuintensitäten für β-lactoglobulin (BLG) Lösungen. In Teil C der Abbildung ist

die Volumenfraktionsabhängigkeit der Position q_c des Korrelationspeaks zu sehen. Die verschiedenen Symbole stehen für unterschiedliche Methoden, den Korrelationspeak zu bestimmen. Zum einen wurde der Korrelationspeak aus der Intensität bestimmt, für die ein Beispieldatenset in Abb. 5.1A gezeigt ist (blaue Quadrate). Desweiteren wurde die Position des Korrelationspeaks aus dem experimentellen Strukturfaktor bestimmt, für den ein Beispieldatenset in Abb. 5.1B zu sehen ist (gelbe Dreiecke). Schließlich wurde der Strukturfaktor aus Datenfits berechnet. Dabei wurde einmal das *Screened Coulobmic (SC)* und einmal das *Two-Yukawa (2Y)* Potential verwendet. Die mit orangen Kreisen markierten Peakpositionen stammen von den SC-Strukturfaktoren, die lila Diamenten markieren die Peakpositionen aus den 2Y-Strukturfaktoren. Interessanterweise fallen die Peakpositionen aus experimentellen Strukturfaktoren und aus 2Y-Strukturfaktoren zusammen. Auch die beiden schwarzen Sterne bestätigen diese Ergebnisse. Diese beiden Datenpunkte sind die Peakpositionen in den Strukturfaktoren, die mit Hilfe von Neutronen-Spin-Echo (NSE) gemessen wurden (Abb. 5.2). In Tabelle 11.1 im Anhang zu Publikation B sind die Parameter der Fits von q_c vs. Proteinvolumenfraktion φ aufgelistet. Der Exponent b ist sowohl für den experimentellen als auch für den 2Y-Strukturfaktor etwa 0.1. Dieser Exponent kleiner als 0.3 deutet auf Clusterbildung hin. Ergänzt werden die statischen Messmethoden durch dynamische Messmethoden, die die Diffusion der Proteinmoleküle und Proteincluster ergründen. In Abb. 5.2 sind die Ergebnisse der dynamischen Messmethoden Neutronen-Spin-Echo (NSE) und Neutronen-Rückstreuung dargestellt. Abb. 5.2C zeigt die Diffusionskoeffizienten, die mit Hilfe von NSE (Kreise) und NBS (Dreiecke) ermittelt wurden. Die Selbstdiffusionskoeffizienten aus NBS sind in Abb.5.2D als Funktion von φ aufgetragen. Die gestrichelte Linie beschreibt die theoretische Selbstdiffusion eines BLG-Dimers. Die gepunktete Linie beschreibt die theoretische Selbstdiffusion eines Clusters aus vier BLG-Dimeren. Die experimentellen Selbstdiffusionskoeffizienten liegen unterhalb der theoretischen Kurve für das BLG-Dimer und nähern sich bei hoher Proteinvolumenfraktion der Kurve für das Cluster aus vier BLG-Dimeren an. Aus den NBS-Selbstdiffusionskoeffizienten wurde der hydrodynamische Radius R_h der Cluster berechnet. Die Anzahl der Dimere pro Cluster kann aus der $q_c(\varphi)$-Abhängigkeit und der Menge des jeweils eingewogenen Proteins berechnet werden. Bei der höchsten untersuchten Proteinkonzentration ist die Zahl der Dimere pro Cluster N_{dimers} etwa 3.7. R_h ist proportional zu $N_{dimers}^{0.32\pm0.02}$. Dies impliziert eine kompakte Clusterform. Die Messungen zeigen weiterhin, dass sich in BLG-Lösungen statische Cluster mit einer Mindestlebenszeit von 50 ns bilden.

In dem System aus BSA und trivalentem Salz wurde bisher sowohl Selbstdiffusion als auch kollektive Diffusion nur in Regime I mit YCl_3 gemessen. In Teil drei dieser Arbeit werden Ergebnisse von Messungen der kollektiven Diffusion in Regimes II und III diskutiert. Die Messungen in allen drei Regimes werden zudem auf Lösungen mit $LaCl_3$ erweitert. Abb. 6.1 zeigt die Phasendiagramme für BSA mit $LaCl_3$ sowie für BSA mit YCl_3 in H_2O. Die schwarz gestrichelte Ellipse markiert die LLPS-Region in BSA mit YCl_3. Die schwarzen Quadrate geben die Protein- und Salzkonzentrat-

ion in der dünnen Phase der LLPS Proben an. Die Daten für BSA mit YCl_3 wurden von M. Wolf aufgenommen. Ähnlich wie für H_2O und D_2O ist Regime II mit $LaCl_3$ schmäler als mit YCl_3. SAXS Messungen wurden für Proben mit 84 mg/ml BSA durchgeführt (Abb. 6.2). Bei beiden Salzen steigt die Intensität $I(q)$ bei niedrigem q erst und sinkt dann langsam wieder. Bei gleicher Salzkonzentration (ab 6 mM) ist die Intensität bei kleinem q, $I(q \to 0)$, für YCl_3 höher als für $LaCl_3$. Das Verhalten von $1/I(q)$ spiegelt sich auch in den aus dem SHS Potential berechneten B_2/B_2^{HS}-Werten wieder. B_2/B_2^{HS} ist der reduzierte zweite Virialkoeffizient. Sowohl $I(q \to 0)$ als auch B_2/B_2^{HS} sind in Abb. 6.3 dargestellt. In beiden Systemen wurde die kollektive Diffusion gemessen. Abb. 6.5 präsentiert die Ergebnisse. Die gefüllten Symbole sind die Ergebnisse für BSA mit $LaCl_3$, die offenen Symbole sind für BSA mit YCl_3. Die Daten für BSA mit YCl_3 im linken Teil der Abbildung wurden von D. Soraruf gemessen und sind bereits veröffentlicht[3]. Die intermediäre Streufunktion, die mit dynamischer Lichtstreuung gemessen wird, besitzt in den beiden Systemen bei niedriger Proteinkonzentration zwei Moden. Die erste Mode (schnelle Diffusion) wird charakterisiert durch D_1, die zweite Mode (langsame Diffusion) durch D_2. A_2 ist der Beitrag der langsamen Diffusion zum Gesamtsignal. In dieser Arbeit wird die schnelle Diffusion der Diffusion von Protein-Monomeren zugeschrieben, während die langsame Diffusion der Diffusion von Protein-Clustern zugeschrieben wird. Der Verlauf der kollektiven Diffusion ist in beiden Systemen derselbe. Die Daten für BSA mit $LaCl_3$ legen ein Abflachen der Diffusionskoeffizienten im zweiten Regime nahe. Der grüne Bereich markiert Anfang und Ende des zweiten Regimes. (Die Daten im zweiten Regime sind nicht komplett dargestellt.) Das Abflachen der schnellen Diffusion würde bedeuten, dass c^* keine Spinodale darstellt. Aufgrund von möglicher Mehrfachstreuung in Regime II ist bei der Interpretation der Daten in Regime II allerdings Vorsicht geboten. Konsistent mit dem schmäleren Regime II in BSA mit $LaCl_3$, sinkt der Beitrag der langsamen Diffusion in Regime III wieder. Für BSA mit YCl_3 ist er bei diesem Salz-Protein-Verhältnis c_s/c_p ($\sim$ 60-70) noch nahezu 1.

Zusammenfassend zeigen die Ergebnisse in der vorliegenden Arbeit, dass sowohl das Lösungsmittelisotop als auch die verwendeten Kationen und Anionen einen starken Einfluss auf das Phasenverhalten von BSA - L¨sungen mit trivalenten Salzen haben. Das makroskopisch beobachtbare Phasenverhalten spiegelt sich auch in den Messungen der kollektiven Diffusion wieder. Die Ergebnisse zeigen weiter, dass sich in BLG - Lösungen bei erhöhen der Konzentration statische Cluster mit einer Mindestlebensdauer von 50 ns bilden.

Als kleiner Ausblick, kann in zukünftigen Untersuchungen der mikroskopische Grund für den starken Einfluss des Lösungsmittelisotops auf die effektive Attraktion erforscht werden. Interessant wäre beispielsweise eine vergleichende Kalorimetrie-Studie in H_2O und D_2O. Um den Anioneneffekt besser zu verstehen, könnten Zetapotential-Messungen mit einem Chlorid- und einem Nitratsalz durchgeführt werden. Die neu entwickelte Methode zur Erforschung von Proteinclusterbildung kann in Zukunft auch auf andere Proteinsysteme wie das System aus BSA und trivalentem Salz angewendet werden.

Abstract

Proteins are essential for life. Both in vitro and in vivo their behavior is goverend by the interactions which they are subject to. Models from colloid theory quantitatively characterize the effective interaction potential between protein molecules in solution. This allows to better understand the mechanisms behind protein aggregation, cluster formation and crystallization. Protein aggregation is the reason for diseases such as e.g. sickle cell anemia. Protein crystals are grown in order to elucidate the structure and function of proteins. Protein clusters are possible precursors for protein crystals. Moreover, the study of protein clusters is relevant for antibody drug delivery. Clusters tend to form when there is a competition between a short-range attractive and a long-range repulsive potential. At present, cluster formation in systems with competing interactions is an active research field in experiment, simulation and theory.

In our group we study cluster formation in a model protein-salt system with a rich phase behavior. The model system of interest is the globular protein bovine serum albumin (BSA) in solution with a trivalent salt (here either $LaCl_3$, $La(NO_3)_3$ or YCl_3). When the salt concentration c_s in this system is increased at a fixed protein concentration c_p, a reentrant condensation (RC) behavior is found which is due to charge inversion on the protein surface. The protein solutions are clear up to the lower salt concentration boundary of the RC (c^*) where they become turbid. Above the upper salt concentration boundary of the RC (c^{**}) the protein solutions turn clear again. The c_s-c_p phase diagram is accordingly divided into regimes I, II and III. This system further shows a liquid-liquid phase separation (LLPS) that occurs in the condensed regime when temperature is increased. This phase separation is driven by entropy. The microscopic reason for the attraction between the protein molecules is believed to be the formation of ion bridges.

So far, dynamic investigations both by light and neutron scattering were limited to regime I. Part B of this thesis presents a dynamic study on a pure protein system. The method applied there can in the future also be applied to the model system of BSA and trivalent salt. In part C of the thesis the light scattering measurements are extended to regimes II and III. Dynamic methods using neutrons, as in part B of this thesis, require the usage of D_2O. Therefore the effect of the solvent isotope on the phase behavior is important. Generally it is assumed in neutron scattering and nuclear magnetic resonance experiments that the solvent isotope does not change the properties of the protein studied. Part A of this thesis investigates the influence of the solvent isotope in the model system of BSA and trivalent salt. Contrary to the general assumption, it is found that the effective attraction is much stronger in

D_2O compared to H_2O. This is observed consistently by visual inspection of sample solutions as well as by characterizing the interaction using model fits to small-angle X-ray scattering (SAXS) data.

As already shortly mentioned, part B of this thesis presents a framework that combines static and dynamic methods to study cluster formation in pure β-lactoglobulin (BLG) solutions. The effect of crowding on protein cluster formation is studied. Crowding plays an important role in the cell where proteins move in an environment with a high concentration of macromolecules. The study in this thesis addresses the question whether under (self-)crowded conditions the proteins still move as monomers or as clusters. By neutron backscattering (NBS) the self-diffusion coefficient is measured. Assuming Brownian diffusion, the hydrodynamic radius of the diffusing entity is obtained. It is found to increase with increasing protein concentration. The analysis of neutron spin echo (NSE) and SAXS data yields the number of dimers per cluster. The combination of NBS, NSE and SAXS shows that the clusters are compact. At 300 mg/ml 3 to 4 protein dimers move together in one cluster. The NSE data further shows that the lifetime of the clustes is above 50 ns. In terms of a model potential, the Two-Yukawa model proves to be suitable to describe the effective interactions. The unique way to study cluster formation in pure protein solutions by combining statics and dynamic may in the future help to study cluster formation in more complicated systems as, for instance, in the BSA-trivalent salt model system.

Part C of the thesis describes cluster formation in the model system of BSA and trivalent salt. An existing study on collective diffusion in BSA with YCl_3 in regime I is extended to BSA with $LaCl_3$ and to regime III. Solutions with BSA and $LaCl_3$ are also measured in regime II. Cluster formation is studied by dynamic light scattering (DLS). The concentrations investigated are between 5 and 25 mg/ml. In this concentration range, the intermediate scattering function has two modes which belong to fast and slow diffusion. The fast diffusion mode can tentatively be assigned to monomers and the slow one to clusters. The lifetime of these clusters that are visible in dynamic light scattering is in the range of approximately 1 to 100 ms which is very long compared to the clusters which were observed using NBS. The observation time scale of the NBS instrument is around 4 ns. As outlined above, using NSE, the time scale was extended to $\sim$50 ns. The DLS results in BSA with $LaCl_3$ show the same trends as in the system with BSA and YCl_3. The collective diffusion coefficients and the contribution of clusters to the scattering signal reflect the effective interactions quantified by SAXS measurements as well as the observations made by visual inspection of the protein solutions.

To further characterize the BSA-trivalent salt system, the effect of two anions on the phase behavior is investigated in part D of the thesis. The employed anions are Cl^- and NO_3^-. These two anions are very close in the Hofmeister series. Nevertheless it is found that NO_3^- strongly enhances the attraction in comparison to Cl^-. This is found both by visual inspection of the sample solutions and by quantitative analysis of SAXS data.

Part I

Fundamentals

Chapter 1

Introduction

There are various possible mechanisms by which proteins in solution can interact. There are van der Waals interactions, Coulomb interactions due to the charges on the protein, hydrophobic and hydrophilic interactions, and formation of ion bridges or covalent bonds. Each different type of microscopic interaction leads to a corresponding macroscopic phase behavior. An active research field is the study of systems with competing interactions where both a short-range attraction and a long-range repulsion are present. The combination of attraction and repulsion can lead to cluster formation. The model system of interest in this thesis is the globular protein bovine serum albumin (BSA) in solution with trivalent salts (YCl_3, $LaCl_3$ and $La(NO_3)_3$). Effective interactions as well as protein cluster formation are studied in this system.

Dynamic measurements using neutrons require the usage of D_2O as solvent. The first part of the thesis is concerned with the effect of the solvent isotope on the phase behaviour. Contrary to the general assumption in the fields of neutron scattering and neutron magnetic resonance, the solvent isotope is found to change the attraction strength in the studied model system.

The second part of the thesis addresses protein cluster formation in a pure protein system. Static and dynamic methods are combined in a unique way. The established framework can in the future be applied to other systems as for example to the BSA-trivalent salt system. Apart from providing a framework for future studies, self-crowding in pure β-lactoglobulin (BLG) solutions is also of interest on its own. The concentration of macromolecules in the cell is high, in the order of 200-300 mg/ml[4]. The study thus elucidates the conditions for biochemical reactions in vivo.

Solutions of BSA and trivalent salts show a reentrant condensation (RC) phase behavior. As further explained in section 1.2, the phase diagram can be divided into three regimes. So far, collective and self-diffusion were measured for BSA with YCl_3 in regime I[3;5]. In part three the collective diffusion measurements are extended to BSA with $LaCl_3$ and to regime III. In solutions with BSA and $LaCl_3$ the collective diffusion is also measured in regime II.

As a further parameter, the effect of the anion on the phase behavior is studied in the fourth part of the thesis. The difference between NO_3^- and Cl^- is investigated. These two anions are close in the Hofmeister series. Nevertheless, in the studied system they lead to a strong difference in the attraction strength.

The remainder of this introductory chapter presents an overview on literature

regarding clusters. Some of the literature that is presented was published in a special issue of the Journal of Physical Chemistry B in 2011 with the title *Clusters in Complex Fluids*. Following this overview, the protein solutions with trivalent salts and their phase behavior are introduced.

1.1 Overview of literature regarding clusters

1.1.1 Clusters of various types in different protein systems

Cluster formation has been observed in various protein systems. There are clusters in aqueous protein solutions, sometimes with added salt. The types of clusters that were observed in protein solutions differ in size and morphology. Protein clusters were discussed as possible precursors for protein crystals. In some systems the clusters preceded gelation. Moreover, protein clusters formed in artificial cell membranes.

Covalently cross-linked clusters were observed in a food technology study. Enzymes were used to covalently cross-link the protein molecules. This crosslinking is needed to e. g. produce gels and thickeners. In one study the crosslinking process of α-lactalbumin was monitored. Gelation occured already at rather low protein concentrations between 3 and 4 % (w/v), which corresponds to 30 to 40 mg/ml. At even lower protein concentrations but constant ratios of protein and enzyme, covalent clusters formed. Due to the low concentration at which gelation occured, these clusters were assumed to have an open structure[6].

Non-covalently bound protein clusters were observed in aqueous solution in the presence of salts. In 1998, the formation of human serum albumin and ovalbumin clusters was observed in the presence of heavy metal ions. Light scattering was applied to monitor the pH dependencies of the second virial coefficient and of the mass of the scattering particles. Close to the isoelectric point, the mass of the scattering particles was found to be highest. Curiously the value of the second virial coefficient was determined to be largest (i.e. repulsive) close to the isoelectric point[7].

Another early study that reported protein cluster formation was the one by Baglioni et al. They observed the formation of clusters in solutions of cytochrome C. Without salt the scattering curves showed a peak which was related to local ordering of the protein molecules. When salt (sodium salts of thiocyanate, chloride and sulfate) was added, a cluster peak appeared. The cluster formation was sensitive to the specific anion and to the volume fraction. The size as well as the fractal dimension of the resulting clusters followed the trends of the Hofmeister series. The cluster formation went along with a structural arrest as revealed by viscosity measurements[8].

The eye lens proteins are an interesting class of proteins. Their aggregation behavior is directly related to eye cataract. α-crystallin and γ-crystallin are two proteins

in the eye lens with different properties. Their diffusion behavior has been compared by Bucciarelli et al. For α-crystallin a self-diffusion behavior was found which is very well described by hard-sphere models from colloid theory. The self-diffusion behavior of γ-crystallin and its volume fraction dependence, however, was not reproduced by colloid theory. There was a significant slow-down of the self-diffusion. Computer simulations were carried out where the proteins were represented by spherical particles. The effect of two different kinds of potentials on the self-diffusion behavior of γ-crystallin was tested. The finding was that with the addition of a short-range attraction the self-diffusion coefficients moved towards the experimental ones. By further adding two attractive patches on each particle, the experimental data were approached even closer. Simulation snap shots showed the formation of transient clusters. In the case of the isotropic attraction the clusters were compact and rather small. The potential with the attractive patches led to more open and network-like cluster structures[9].

Protein cluster formation is relevant for the actively debated topic of protein crystal nucleation. For many crystallization phenomena, also in non-protein systems, it is known that classical nucleation theory can only describe crystal formation qualitatively, but not quantitatively. Instead, two-step mechanisms have been observed where crystals formed via a first step of disordered clusters[10]. In solutions of lysozyme and NaCl, the existence of fractal clusters could be used as a criterion for the degree of supersaturation and thus the crystal nucleation rate. Formation of fractal clusters was observed by dynamic light scattering (DLS) and static light scattering (SLS). The size of the clusters increased with the supersaturation of the solution. The same group further performed energy minimization calculations for 4-60 spheres which interacted via a suitable potential. In line with the experiments, the calculation results showed fractal cluster structures[11]. For glucose isomerase, experiments also showed that protein clusters increased the crystal nucleation rate. Moreover, protein clusters contributed to the growth of smooth and impurity-free crystal surfaces[12]. In the case of lumazine synthase, dense liquid droplets play a role during crystal growth. New crystal layers were formed when a dense liquid droplet was attached to the crystal surface. DLS measurements showed that the cluster droplets continuously formed and dissolved. They were metastable both with respect to the solution and the crystal[13]. Monte Carlo simulations with a short-range attraction and an additional intermediate-range repulsion successfully reproduced the clusters[14]. Recently, the crystallization of lysozyme has been studied by in situ transmission electron microscopy. In unfiltered lysozyme solutions there were small structures which did not coalesce and also did not grow into crystals. These small structures were named amorphous solid particles (ASPs) – "solid" because they did not coalesce and "amorphous" because there was no diffraction pattern. In filtered lysozyme solutions these ASPs were not present. This went along with a reduced crystal nucleation rate. The ASPs thus enhanced crystallization and served as heterogeneous nucleation sites. Importantly, the ASPs themselves were never seen to

turn into crystals. Non-crystalline particles different from the ASPs were observed to over time develop crystal facets[15].

In solutions of different variants of hemoglobin and in solutions of lysozyme the group of Peter G. Vekilov, which also performed the above mentioned study on lumazine synthase, found a different type of clusters. The clusters that were reported by this group were large mesoscopic clusters with radii on the order of 100 nm which contained about $10^5 - 10^6$ single protein molecules[16;17]. The ratio of clusters and monomers in solution was very small, $10^{-6} - 10^{-4}$. The lifetime of the clusters was on the order of several seconds and the nature of the clusters was not gel-like but fluid[17]. It was proposed that the clusters consist of a non-equilibrium mixture of protein monomers and protein complexes in which the rate of formation of the complexes is different from the rate of their decay. The clusters would stop growing due to a chemical reaction which makes the protein complexes in the cluster break up into monomers[17;18]. The introduction of space and time-dependent rate constants, however, showed that this model cannot explain the existence of mesoscopic clusters[18]. In lysozyme solutions clusters with sizes of the same order of magnitude as reported by the Vekilov group have already been studied in the early 90's[19]. Contrary to the clusters by the Vekilov group which do not change size over time[16], Georgalis et al. reported clusters that grew with time. The growth was described using models for fractal cluster growth. More specifically, crystal growth proceeded via diffusion limited cluster aggregation. Vekilov's group dissolved lysozyme in HEPES buffer. Georgalis et al. studied lysozyme in solution with NaCl (in which lysozyme crystallizes) and $(NH_4)_2SO_4$ (in which lysozyme does not crystallize but precipitates).

Protein clustering was also observed in artificial cell membranes. The membrane protein nephrin clustered when the concentration of two other proteins that interact with the nephrin tail in the solution exceeded a critical value. The clusters consisted of all three proteins. They were fluid and highly dynamic. The individual proteins changed their positions on a timescale of seconds or minutes whereas the clusters themselves persisted for hours. Nephrin remained in the membrane. Thus, in this sense, these clusters were two-dimensional ones. Cluster formation or phase separation was accompanied by a polymerization of the proteins. The clusters helped to promote the formation of actin networks. There are other membrane proteins which are also known to form clusters when they bind to ligands or when two cells stick together[20]. Furthermore, phase separation of the three investigated proteins has also been observed in bulk solutions[21]. Simulations show that cluster formation of proteins in the membrane is a general phenomenon. Different potential types led to cluster formation as long as they consisted of a short-range attractive and a long-range repulsive part. If different protein families were taken into account, the attraction between similar molecules differed from the attraction between different molecules. This energy difference is an important parameter. It was shown that there is a threshold value of this energy difference below which there were mixed

clusters and above which clusters mainly consisted of one protein species. Three-body interactions were also considered as far as computationally possible. They did not destabilize the clusters[22].

Summarizing, cluster formation has been reported for different proteins. In aqueous solution the proteins may either be covalently cross-linked by enzymes or the clusters form due to a weaker attraction between single protein molecules. Sometimes cluster formation is promoted by the addition of salts. Protein clusters were shown to play an important role during protein crystal growth. Finally, cluster formation has not only been reported in bulk solution but also in artificial cell membranes. After showing that protein clusters occur in different systems, the following paragraphs specifically describe the formation of equilibrium clusters and present studies that explore short-range attractive, long-range repulsive (SALR) potentials.

1.1.2 Competing interactions and equilibrium cluster formation

Groenewold and Kegel presented a fundamental theoretical work regarding equilibrium cluster formation. They described the energy contributions in a colloid system with both a short-range attraction and a long-range repulsion. In their model the short-range attraction is due to dispersion interactions and the long-range repulsion is due to Coulomb interactions. With this theory they predicted the existence of large equilibrium clusters[23]. The type of potential that was employed by Groenewold and Kegel, a SALR potential, plays an important role in all research on equilibrium cluster formation. The attraction brings the particles together and the repulsion stabilizes a finite cluster size. A useful potential in this respect is the Two-Yukawa potential that consists of an attractive exponential term and a repulsive exponential term. This potential and its implementation was discussed by Liu et al.[24].

Equilibrium cluster formation is studied in both colloid and protein systems. Currently, theoretical and simulation groups are also interested in competing interactions which are necessary for equilibrium cluster formation. A few examples will be shown here. First, some theoretical work and experimental findings in colloid systems as well as in a system of protein and polyelectrolyte are presented. Then, experimental work on equilibrium clusters in pure protein systems is discussed. Finally, a few selected theoretical and simulation studies are shown that cover the relation of the so-called intermediate range order (IRO) peak in the structure factor and the formation of clusters.

Some examples of pattern and cluster formation in systems with SALR interactions

In a two-dimensional system pattern formation was observed when a potential with an attractive and a competing repulsive part was investigated. Depending on the density the transition from a droplet or a stripe phase to a homogeneous phase was observed when the temperature was increased [25].

By another group the ground state energy of a cluster of particles that ineract via a SALR potential was calculated numerically and analytically, neglecting cluster-cluster interactions. The employed short-range attraction was of a Lennard-Jones type (using a large exponent). The parameters characterizing the attraction were kept fixed. When the strength A and the range ξ of the repulsive interaction were varied, a region in the (A, ξ) space was found, where the ground state energy was minimal at a finite cluster size [26].

Experimetally, using confocal microscopy, clustering was observed in colloidal solutions with SALR interactions at low volume fractions. When the volume fraction was increased the clusters percolated to form a gel. The building blocks of the clusters as well as of the gel were tetrahedra [27]. Solutions of charged poly(methylmethacrylate) (PMMA) particles with polystyrene may either end up in an equilibrium cluster state or in a gel state, depending on the exact concentration of PMMA colloids and polystyrene polymers. The fraction of unbonded particles as well as the mean cluster size changed abruptly when the gelation line was crossed or closely approached. Diffusion limited cluster aggregation (DLCA) and reaction limited cluster aggregation (RLCA) theories do not describe equilibrium clusters. However, the radius of gyration vs. the number of particles per cluster of the PMMA equilibrium clusters still followed a fractal power law behavior. The power law behavior could be assigned to the diffusion limited cluster aggregation (DLCA) behavior at low colloid volume fraction and to the RLCA behavior close to the gel boundary [28]. At low volume fraction of charged PMMA particles and low concentration of polystyrene, a "fluid-cluster" phase was observed by another group using confocal microscopy. Polystyrene was used to induce a depletion attraction between PMMA particles. A long-range electrostatic repulsion arose from the charged fluorescent dye attached to the particles. When the strength of the depletion attraction was increased by adding more polystyrene, the system arrested in a gel state. At high volume fraction and strong attractive interaction, the solutions did not reach the equilibrium cluster case [29].

Proteins in solution with oppositely charged polyelectrolytes also form clusters. In a simulation study the protein was modeled as a hard sphere with a charge distribution based on the crystal structure of lysozyme. The polyelectrolyte was modeled as a chain of hard spheres with one negative charge on each sphere. Initially, the only interaction allowed between all macroions was purely electrostatic. It was found that cluster formation was most pronounced at low ionic strength and when the total

charge on all polyelectrolyte molecules was approximately equal to the total charge of all protein molecules. When the charges were screened by a high ionic strength, cluster formation was hampered. The introduction of an additional attractive interaction between the protein molecules restarted cluster formation. Furthermore, in this study a redissolution behavior was observed when the polyelectrolyte concentration was increased above the point where the charges on protein molecules were equal to those on the polyelectrolyte molecules[30].

Experimental works on (equilibrium) protein clusters

One of the first systematic studies on equilibrium cluster formation in pure protein (lysozyme) solutions was performed by Stradner et al. The cluster-cluster peak in the effective structure factor did not change its position when the protein concentration was increased. It was assumed that this cluster-cluster correlation peak reflects the distance between the centers of mass of the scattering particles. In pure lysozyme solutions the distance between the scattering particles thus stayed constant even when more and more protein molecules were added. Therefore, the scattering particles had to be clusters of single proteins where the number of proteins per cluster increased with increasing protein concentration. In the investigated volume fraction range up to nearly 0.25 the cluster size grew proportionally to the volume fraction. The estimated numbers of monomers per cluster ranged from a bit less than 2 to approximately 11. Variation of temperature showed larger clusters at lower temperatures[31;32]. Shukla et al. challenged these results. They repeated the expriments performed by Stradner et al. A clear shift of the cluster-cluster correlation peak with volume fraction was found. The scattering intensity was fitted using a model of lysozyme monomers interacting via a Two-Yukawa potential. The potential parameters changed with temperature. For comparison, the scattering intensity of a colloid solution which is known to form clusters, was discussed[33].

A neutron spin-echo (NSE) study accessing the dynamics of lysozyme solutions showed clustering at high protein concentrations. The self-diffusion coefficients were extracted from the high q limit of the NSE data. The diffusion coefficient of lysozyme decreased faster with increasing volume fraction than that of hard or charged spheres. This was explained by the existence of clusters. The clusters were suggested to be dynamic, i.e. existing only on the short-time limit. 25 ns was found to be a lower limit for the cluster lifetime. In the investigated volume fraction range up to 0.2, the hydrodynamic radius R_h of the clusters was estimated to lie between 1.2 and 2.5 monomer hydrodynamic radii[34].

Careful analysis of SANS data at different volume fractions and pH values showed that the IRO peak was more pronounced at low concentrations where the NSE results pointed towards predominantly monomeric proteins (R_h equal to 1.2 hydrodynamic radii of a lysozyme monomer). Long-time self-diffusion coefficients, accessed by NMR experiments, were found to essentially reproduce the short-time

self-diffusion coefficients. Generally, long-time diffusion is slower than short-time diffusion. Therefore, in the long-time limit the solutions had to be regarded as consisting of lysozyme monomers. A lower limit for the cluster lifetime was given by the time up to which the intermediate scattering function from NSE was described by a single exponential function. This time was 50 ns. The clusters were identified as being dynamic instead of transient or permanent. Based on the finding that the first peak in the structure factor could not directly be related to cluster formation, the term *IRO* peak was introduced [35].

Selected simulation and theory studies dealing with the relation of the IRO peak to cluster formation

The experimental detectability of protein clusters is a debated topic. As already mentioned in the previous section, it turned out that not only clusters but also so-called IRO structures may lead to a correlation peak in the structure factor. Simulations are a helpful tool for detailed studies of the relation between the appearance of an IRO peak in the structure factor and the microstructure of the solution. Note here that for a comparison of simulation and experimental works, the accessed timescales are important. In the simulation by Godfrin et al. [36], for example, each particle performs on average $2 \cdot 10^7/1728 = 11574$ movements. If the particle with diameter σ moves 0.1σ each time, it will have moved across its own diameter after 10 moves and across ~ 1000 diameters at the end of the simulation. This simualtion would thus address the long-time limit. A detailed analysis of the timescales that are addressed in the following simulation studies is beyond the scope of this thesis.

MD simulations of colloidal particles with a small polydispersity that interact via a DLVO potential revealed a stable cluster phase at low temperature and low volume fraction. At high volume fraction the systems gelled [37].

Lysozyme molecules were modeled by spheres which interact via a hard sphere interaction. The amino acids were represented by charges inside of the spheres. These charges interacted via electrostatic interactions. Furthermore, each sphere contained a hydrophobic interaction site which interacted attractively with hydrophobic sites in other molecules. The results of the simulations showed that oligomers (2 to maximum 8 proteins) form when the protein concentration or the ionic strength of the solvent increase and when the charge on the protein decreases [38].

The experimental structure factor obtained by Stradner et al. with the concentration-independent IRO peak was well reproduced by a molecular dynamics (MD) simulation structure factor. MD simulations were carried out with the same SALR potential parameters. Snapshots of the simulation box and analysis of the MD data revealed a broad size distribution of the clusters. The cluster size distribution exhibited no peak but slowly decayed from a maximum at one particle to zero at cluster sizes of 30 to 600 particles. For volume fractions above 0.15 the MD simulations

resulted in a percolated network[39]. Furthermore, the experiments on equilibrium clusters in lysozyme solutions by Stradner et al. were extended to NSE measurements. The inverse of the measured short-time diffusion coefficient is proportional to the structure factor. The results also show the cluster peak q_c. There is no pronounced further oscillation in the structure factor at higher q. This indicates transient clusters with a lifetime longer than the observation timescale of the NSE spectrometer. At low volume fractions the NSE results are well reproduced by Brownian dynamics (BD) simulations. At higher volume fractions the BD simulations which neglect many-body interactions were not able to reproduce the measured diffusion coefficients[40].

The Two-Yukawa potential parameters obtained by Shukla et al.[33] for rather low lysozyme concentrations were also used to perform Monte Carlo simulations. At low lysozyme volume fraction, the simulated solutions were dominated by monomers. At higher volume fraction the fraction of monomers strongly decreased and clusters of different sizes formed. The clusters tended to have an elongated shape[41].

Pure simulation studies were performed by Godfrin et al. and by Bollinger et al. Godfrin et al. performed Monte Carlo (MC) simulations for colloidal particles that interact via SALR potentials. They studied two different types of SALR potentials and for each potential they tested various possible parameter combinations. The resulting states were classified as *dispersed fluid*, *random percolated*, *clustered fluid* and *cluster percolated*. The resulting states were plotted in a generalized phase diagram where temperature and volume fraction were normalized to the respective critical values. The binodal of a reference attractive potential was added to this generalized phase diagram. Interestingly, clustered fluid and cluster percolated states were found below the binodal whilst dispersed fluid and random percolated states were found above the binodal. IRO peak formation in the structure factor was observed for all four states. Therefore, this study shows that it is not always possible to relate the existence of an IRO peak directly to the formation of clusters. As a criterion for the IRO peak being indeed related to cluster formation, the simulation results suggest a peak height of at least 2.7[36;42].

Bollinger et al. combined MD simulations and integral equation theory to examine the dependence of the IRO peak on attraction and repulsion strength. The simulations revealed a large area of the parameter space where an IRO peak was found. Only in a small fraction of this IRO peak area was there also cluster formation. The necessary criterion of a peak height greater than 2.7 was well confirmed. Another possible criterion is that at the onset of clustering the range of repulsion has to be comparable to the thermal correlation length. Except for very low repulsion ranges, this criterion also held quite well[43].

In another publication by Bollinger et al. SALR MD simulations of clustering fluids for about 100 different combinations of volume fraction, surface charge Z and electrostatic screening length were presented. The resulting cluster sizes N were compared to the predictions of the free energy model by Groenewold and Kegel. The

model by Groenewold and Kegel states that $N \propto [\beta\epsilon]/[Z^2(\lambda_B/d)]$. The numerator in this expression, $\beta\epsilon = \epsilon/k_BT$, characterizes the strength of the short-range attraction. The denominator characterizes the strength of the long-range repulsion (unscreened Coulomb repulsion). λ_B is the Bjerrum length. In the simulations 60% of the particles had a diameter d, 20% of the particles a diameter $d + 0.158\,d$ and 20% of the particles a diameter $d - 0.158\,d$. The polydispersity was introduced to prevent crystallization. The simulated cluster sizes indeed lay on a master curve when plotted against the ratio of attraction strength and repulsion strength. However, the scaling exponent was not equal to one as predicted by Groenewold and Kegel, but rather 3/4. This lower exponent was explained by a size-dependent coordination number which results in a size-dependent number of missing bonds at the surface. The surface energy penalty then scales with an exponent of 1/3 instead of 2/3[44].

To summarize, theory predicts the formation of equilibrium clusters for systems where the interaction is of a SALR type. In colloidal systems fluid cluster phases have been observed using confocal microscopy. As proteins are smaller than colloids, it has not been possible to study them by confocal microscopy. Small-angle X-ray scattering (SAXS) and NSE data, however, point to the formation of equilibrium clusters also in protein systems. The interpretation of the small angle X-ray scattering (SAXS) is debated. Simulation studies contribute to understanding the relation between the IRO peak in the structure factor and the microstructure of the solutions. They also show clustering. Pure simulation studies, however, also show that an IRO peak cannot always be related to cluster formation.

1.2 BSA in solution with trivalent salts

This section introduces the model system of BSA in solution with a trivalent salt. Parts A, C and D of this thesis study this model system. First of all, for BSA in solution with trivalent salts a RC behavior was found[1;2]. A schematic phase diagram is shown in Fig. 1.1. At a fixed protein concentration c_p sample solutions turn from clear to turbid to clear when the salt concentration c_s is increased. The c_s-c_p phase diagram is accordingly divided into regimes I, II and III. In regime II the sample solutions are turbid. The lower and upper c_s boundaries of regime II are called c^* and c^{**}, respectively. If the attraction strength is suitable, there is also liquid-liquid phase separation (LLPS) in a certain region of regime II. This LLPS has a lower critical solution temperature (LCST), implying an entropic driving force of the phase separation. As shown in the left part of Fig. 1.1, the reason for the RC phase behavior is charge inversion on the protein surface. At low salt concentrations the BSA molecules are negatively charged. The trivalent cations bind to carboxy groups on the protein surface and thereby lead to a charge inversion at high c_s. Condensation starts when the protein is approximately neutral. The microscopic origin of the attraction and thus the RC phase behavior is the formation of ion

bridges between the protein molecules. The effective pair interactions in this system can be described by either a purely repulsive term or a purely attractive term, depending on the concentration of the trivalent salt. At low c_s in regime I a screened Coulombic, long-range repulsive, potential describes the interactions. At higher c_s a sticky hard sphere, short-range attractive potential describes the interactions[45–48]. The strength of the attraction and thus the macroscopic appearance of the sample solutions in regime II depend on various parameters such as the specific cation and anion which are employed, the temperature and the solvent isotope. Cluster formation in this system is also assumed to be driven by the formation of ion bridges and has so far been studied in the first regime of the RC phase diagram, prior to macroscopic condensation[3;5].

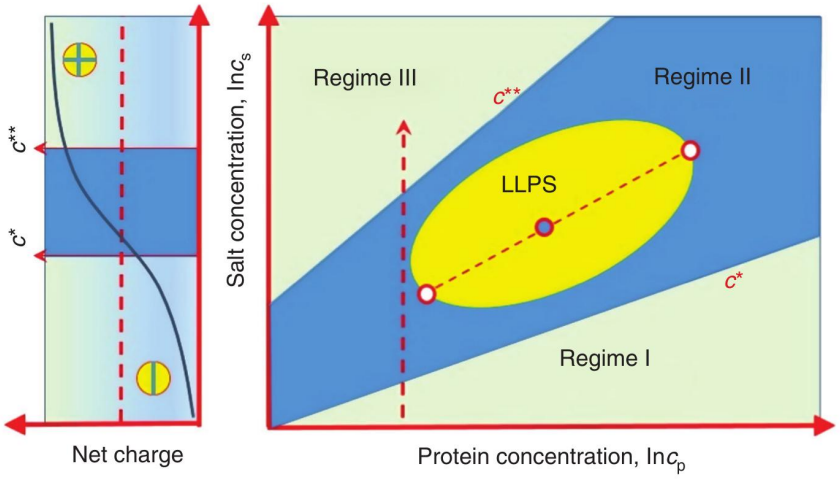

Figure 1.1: *Sketch of the phase diagram in systems of BSA with a trivalent salt. At a fixed protein concentration c_p the solutions turn from clear to turbid to clear when the salt concentration c_s is increased. The reason for the reentrant condensation phase behavior is charge inversion as shown in the left part of the figure. The figure is taken from Zhang et al.*[2].

1.3 Outline

Publication A explores the effect of the solvent isotope on the effective interaction in solutions of BSA with trivalent salts. In contrast to the general assumption, a strong difference in the effective attraction strength is observed when H_2O is replaced by D_2O. In addition to the solvent isotope effect, publication A explores the effect of the cation on the effective interaction. Y^{3+} leads to stronger attraction than La^{3+}.

Publication B contributes a study of cluster formation in pure BLG solutions. Three different methods, characterizing both the static and dynamic properties of the samples, are employed. Dynamic investigations show a slow-down of the self-diffusion coefficient when the protein concentration increases. This slow-down cannot be explained by models from colloid theory with a fixed particle size. Instead the data suggests the formation clusters with increasing volume fraction. Together with the position of the IRO peak in the static structure factor, the size of the clusters is estimated.

Part C extends a previous light scattering study [3] in BSA with YCl_3 to BSA with $LaCl_3$. With $LaCl_3$ the trends are the same as with YCl_3. The measurements are also extended to regimes II and III of the phase diagram. In regime II the transmission of the protein solutions is low (below 50%). Therefore, due to possible multiple scattering effects, the data in regime II has to be treated with care. In regime III with $LaCl_3$ the contribution of clusters starts to decrease at salt concentrations where with YCl_3 there is still a strong contribution of clusters. This finding goes along with the narrower regime II in BSA with $LaCl_3$.

The effect of the anion is studied in results part D. Both, visual inspection of the protein solutions and characterization of the effective interaction using SAXS, show that with NO_3^- the attractive interaction is stronger than with Cl^-. This finding is interesting in light of the Hofmeister series where Cl^- and NO_3^- are close to each other.

1.4 List of manuscripts

- [A] M. K. Braun, M. Wolf, O. Matsarskaia, S. Da Vela, F. Roosen-Runge, M. Sztucki, R. Roth, F. Zhang, and F. Schreiber.
  Strong Isotope Effects on Effective Interactions and Phase Behavior in Protein Solutions in the Presence of Multivalent Ions.
  J. Phys. Chem. B **121** (2017), 1731–1739.

- [B] M. K. Braun, M. Grimaldo, F. Roosen-Runge, I. Hoffmann, O. Czakkel, M. Sztucki, F. Zhang, F. Schreiber, and T. Seydel.
  Crowding-Controlled Cluster Size in Concentrated Aqueous Protein Solutions: Structure, Self- and Collective Diffusion.
  J. Phys. Chem. Lett. **8** (2017), 2590–2596.

- [C] M. K. Braun, R. Schweins, T. Seydel, M. Sztucki, F. Zhang, and F. Schreiber.
  Effective Interactions, Collective Diffusion and Cluster Formation in Protein Solutions in the Presence of Trivalent Salts.
  In Preparation.

- [D] M. K. Braun, A. Sauter, M. Sztucki, F. Zhang, and F. Schreiber.
  Reentrant Phase Behavior in Protein Solutions Induced by Multivalent Salts: Effect of Anions Cl^- versus NO_3^-.
  In Preparation.

Chapter 2

Basic principles of small angle scattering and spectroscopy

Small-angle scattering is useful for studying macromolecules such as proteins which are large compared to single atoms. Each atom in the solution represents a scattering center which interacts with the incoming radiation. There are different methods which either probe the static or the dynamic properties of the system or both. Elastically scattered X-rays deliver information about the static properties. If a certain distance between the scattering particles occurs very often there will be a high intensity at the corresponding scattering vector. Dynamic information is characterized by diffusion coefficients. Neutrons may be used to obtain dynamic information on short timescales greater than approx. 4 ns in a backscattering spectrometer. Longer timescales are accessible with NSE spectrometers. With DLS, processes on even longer timescales (ms) are monitored.

This chapter first explains how static information is obtained in a purely elastic X-rya scattering event. The scattering intensity and the structure factor are described. The structure factor may be modelled using an interaction potential. The potentials which are relevant for this thesis are discussed. The second part of this chapter describes the methods that investigate the dynamics of a system. Dynamic light scattering is explained and the form of the intermediate scattering function for the case of Brownian diffusion is derived. The total scattering function for neutrons and its relations to the pair and self correlation functions are discussed. Finally, the two techniques neutron backscattering and neutron spin-echo are explained.

2.1 Static information

The scattering vector for elastic scattering (Fig. 2.1) is given by $\vec{q} = \vec{k}_{in} - \vec{k}_{out}$. $\vec{k}_{in}$ and $\vec{k}_{out}$ are the incoming and outgoing wave vectors. The magnitude of the scattering vector is

$$q = \frac{4\pi}{\lambda} \sin\left(\frac{\Theta}{2}\right), \tag{2.1}$$

where λ is the wavelength of the radiation[49]. The static scattering intensity at a scattering angle q, which is recorded by small angle x-ray scattering (SAXS), is

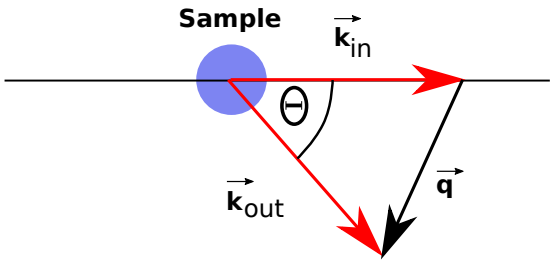

Figure 2.1: *Scattering geometry.*

given by

$$I(q) = N(\Delta\rho)^2 P(q) S(q). \tag{2.2}$$

N is the number of particles in the scattering volume, $\Delta\rho$ is the scattering contrast (difference in scattering length density between solvent and solute). $P(q)$ is the form factor which describes the shape of the individual particles. It is given by

$$P(\vec{q}) = \left| \int_{V_p} \exp^{i\vec{q}\vec{r}}\, d\vec{r} \right|^2 . \tag{2.3}$$

In this thesis, the protein molecules are approximated by ellipsoids with $V_p = \frac{4\pi}{3} R_a R_b^2$. The $q = |\vec{q}|$ dependent form factor is then

$$P(q) = \int_0^1 f^2[qR_b\sqrt{1 + x^2(\nu^2 - 1)}]dx \tag{2.4}$$

where $\nu = R_a/R_b$ and

$$f(qr)^2 = 9V_p^2 \left[\frac{\sin(qr) - qr\cos(qr)}{(qr)^3} \right]^2 \tag{2.5}$$

is the form factor of a sphere with radius r[49–51]. By equating the volume of this ellipsoid to the volume of a sphere one may calculate an effective sphere radius which can then be used to calculate the structure factor[51]. The structure factor $S(q)$ describes the spatial arrangement of the particles which is governed by the interaction potential. In chapter three of the lecture notes by G. Nägele[52], its definition is given as

$$S(q) = \left\langle \frac{1}{N} \sum_{j,k=1}^{N} \exp^{i\vec{q}\cdot(\vec{r}_j - \vec{r}_k)} \right\rangle \tag{2.6}$$

with $< \cdots >$ denoting an equilibrium average. It is related to the pair correlation function g(r) via Fourier transform,

$$S(q) = 1 + 4\pi \frac{N}{V} \int_0^\infty [g(r) - 1]\, r^2 \frac{\sin(qr)}{qr} dr. \tag{2.7}$$

2.1.1 Structure factor

The structure factor is closely related to the potential. It describes the spatial arrangement of the particles in solution. As shown in eq. 2.7 it is related to the pair correlation function $g(r)$ by Fourier transformation. The total correlation function $h(r) = g(r) - 1$ is obtained by solving the Ornstein-Zernicke (OZ) equation. The OZ equation splits the correlations into a direct and an indirect part,

$$h(|\vec{r_i} - \vec{r_k}|) = c(|\vec{r_i} - \vec{r_k}|) + \rho \int d^3 r_j c(|\vec{r_i} - \vec{r_j}|) h(|\vec{r_j} - \vec{r_k}|). \tag{2.8}$$

It is only possible to solve the OZ equation if a statement is made on how to relate c(r) to the interaction potential u(r). This statement is called closure relation [49;53].

The following three paragraphs shortly describe the three potentials that were used in this thesis.

2.1.2 Screened Coulomb potential

The Screened Coulomb (SC) potential for macroions in solution is purely repulsive and is given by

$$u(r) = \pi \epsilon_0 \epsilon \sigma^2 \Psi_0^2 \exp[-\kappa(r - \sigma)]/r. \tag{2.9}$$

σ is the particle diameter, Ψ_0 the surface potential and κ the inverse of the Debye screening length [54]. The structure factor for the SC potential has been calculated analytically using the (rescaled) mean spherical approximation ((R)MSA) [54;55].

In this thesis, the SC potential is used for samples with BSA and trivalent salts at low concentrations of trivalent salts.

2.1.3 Sticky hard sphere potential

The Sticky Hard Sphere (SHS) potential consists of a hard core and a thin attractive square well with depth u_0 and width Δ.

$$\beta u(r) = \begin{cases} \infty & r < \sigma \\ -\beta u_0 = \ln\left(\frac{12\tau\Delta}{\sigma+\Delta}\right) & \sigma < r < \sigma + \Delta \\ 0 & r > \sigma + \Delta \end{cases} \tag{2.10}$$

The stickiness parameter is $\tau = \exp(-\beta u_0)/(12\epsilon)$ where $\epsilon = \Delta/(\sigma + \Delta)$ [51]. The structure factor has been calculated using the Percus-Yevick equation. For $\Delta \to 0$ B_2/B_2^{HS} can be related to τ by

$$B_2/B_2^{HS} = 1 - 1/(4\tau) \tag{2.11}$$

with the second virial coefficient of a hard sphere $B_2^{HS} = 16\pi R^3/3$ and $R = \sigma/2$ [56;57].

In this thesis, the SHS potential is employed for solutions of BSA with trivalent salts at higher salt concentrations where the negative charges of the proteins are screened and the proteins attract each other due to the formation of ion bridges. The SHS potential fits are used for an experimental determination of the reduced second virial coefficient B_2/B_2^{HS}.

2.1.4 Two Yukawa potential

The Two Yukawa potential is an extension of the SC potential. In addition to the repulsive exponential term (negative K_1) it has an attractive exponential term (positive K_2) [24],

$$\beta u(r) = \begin{cases} \infty & 0 < r < \sigma \\ -K_1 \frac{\exp[-Z_1(r-\sigma)]}{(r/\sigma)} - K_2 \frac{\exp[-Z_2(r-\sigma)]}{(r/\sigma)} & r > \sigma \end{cases} \tag{2.12}$$

The structure factor has been calculated using the MSA closure relation [24].

This type of potential is very well suited to describe cluster formation. In this thesis, it is used to fit the SAXS data for the pure BLG system where cluster formation is observed.

2.2 Dynamics

2.2.1 Different types of diffusion

The following paragraph is based on chapter 8 of the lecture notes on *The Physics of Colloidal Soft Matter* by G. Nägele [52]. In publication B the backscattering data is analyzed by assuming that the proteins are subject to Brownian diffusion. The motion of a Brownian particle with mass m in a solvent is described by the Langevin equation which consists of a retarding term due to friction and a random force,

$$m\frac{d\vec{v}}{dt} = -\gamma\vec{v}(t) + \vec{f}(t). \tag{2.13}$$

The friction term is proportional to the friction coefficient γ which for a sphere of radius R in a solvent with shear viscosity η_0 is $\gamma = 6\pi\eta_0 R$. On average the random

force on the particle is zero. Its strength is given by the time-correlation function which also states that the force is not correlated in time,

$$\left\langle \vec{f}(t) \right\rangle = 0 \qquad \left\langle \vec{f}(t)\vec{f}(t') \right\rangle = 6k_B T\gamma\delta(t-t'). \tag{2.14}$$

The solution of the Langevin equation is

$$\langle \vec{v}(t) \rangle = \vec{v}_0 \exp\left(-\frac{\gamma}{m}t\right). \tag{2.15}$$

The characteristic time for the relaxation of the initial velocity of the particle is thus given by a time which is also denoted as the *Brownian time*, $\tau_B = m/\gamma$. The movement of the particle is quantified by the mean square displacement

$$MSD = \frac{1}{6}\left\langle |\vec{r}(t) - \vec{r}(0)|^2 \right\rangle. \tag{2.16}$$

For times smaller than τ_B, the particle movement is ballistic and the MSD is proportional to t^2. For times larger than τ_B the particle movement is diffusive and the MSD is proportional to t. The proportionality constant in the case $t \gg \tau_B$ is the diffusion coefficient D. This diffusion regime can further be divided into a short-time and a long-time regime. In the short-time regime different particles in the solvent interact solely via hydrodynamic, i.e. solvent-mediated interactions or long-ranged electrostatics. In the long-time regime, direct interactions contribute additionally. The long-time regime starts at an interaction time $\tau_I \approx R^2/D$. This is the time that a particle needs to diffuse a length that is equal to its own radius. On this timescale, the particle starts to feel also the cage built by the surrounding particles.

The type of diffusion differs not only in different time regimes. Another distinction between self-diffusion and collective diffusion has to be made. Self-diffusion considers only one tracer particle and follows its motion, while disregarding that of the other particles in the sample. Collective diffusion considers many particles at once and describes how a density wave in space decays over time[52].

The short-time collective diffusion function is proportional to the ratio of the hydrodynamic function and the static structure factor,

$$D(q) = D_0 \cdot \frac{H(q)}{S(q)}. \tag{2.17}$$

D_0 is the diffusion coefficient at infinite dilution. Thus when $H(q) \sim 1$, the diffusion coefficient is the inverse of the static structure factor[34].

In publication B the short-time self-diffusion coefficient is accessed by neutron backscattering (NBS). As already stated above, these diffusion coefficients are analyzed by assuming Brownian diffusion of the proteins. The short-time collective

diffusion function is applicable to the NSE data. At low q NSE measures the short-time collective diffusion. As the results in publication B show, the high q limit of NSE coincides with the short-time self-diffusion coefficients measured by NBS. In part C of the thesis, the long-time collective diffusion coefficient is determined from DLS. The results are also analyzed under the assumption of Brownian diffusion. This will be shown below.

2.2.2 Methods

Dynamic light scattering

The following section summarizes the basics of light scattering theory as outlined in the first five chapters of the book by B. J. Berne and R. Pecora[58]. First, the self-correlation function as well as the self-intermediate scattering function are introduced. The solution of the diffusion equation is given in the case of Brownian diffusion. Then it is explained how the self-intermediate scattering function is obtained by dynamic light scattering.

The self-correlation function and the self-intermediate scattering function are related via a Fourier transform. The self-correlation function is

$$G_s(\vec{R},\tau) = \left\langle \delta(\vec{R} - [\vec{r}_j(t) - \vec{r}_j(0)]) \right\rangle . \tag{2.18}$$

In the case of Brownian diffusion, the self-correlation function is the solution of the diffusion equation,

$$\frac{\partial}{\partial t} G_s(\vec{R},t) = D\nabla^2 G_s(\vec{R},t), \tag{2.19}$$

where D is the self-diffusion coefficient. A Fourier transform delivers the diffusion equation in terms of the self-intermediate scattering function,

$$\frac{\partial}{\partial t} I_s(\vec{q},t) = -q^2 D I_s(\vec{q},t). \tag{2.20}$$

The solution is a single exponential function,

$$I_s(\vec{q},t) = \exp(-q^2 D t). \tag{2.21}$$

If particles with several sizes are present in the solution, the self-intermediate scattering function is an integral over the different decay rates $\Gamma = q^2 \cdot D$ where each Γ and D characterizes one particular particle spezies. $G(\Gamma)$ gives the distribution of decay rates.

$$I_s(\vec{q},\tau) = \int d\Gamma G(\Gamma) \exp(-\Gamma\tau). \tag{2.22}$$

In order to explain the relationship between the measured intensity correlation function $g_2(R,\tau)$ and the self-intermediate scattering function $I_s(\vec{q},\tau)$, it is assumed

that incident and outgoing light is polarized in the same direction. This means that only what is also called the *polarized* component is considered. Furthermore, the sample is characterized by its polarizability $\alpha(\vec{r},t)$ which is a function of the position $\vec{r}$ in the sample and the time t. Note that in the book by B. J. Berne and R. Pecora[58] fluctuations $\delta\epsilon$ of the dielectric function are considered instead of the polarizability. In order to derive the form of the intermediate scattering function for a solution of N particles, here the polarizability $\alpha(\vec{r},t)$ is used instead of the fluctuation $\delta\epsilon(\vec{r},t)$ of the dielectric function $\epsilon(\vec{r},t) = \epsilon_0 + \delta\epsilon(\vec{r},t)$. Volume 2 of the series on experimental physics by W. Demtröder[59] states that if the electric field strength E is not too large, the dielectric polarization is $P = N\alpha E$. N is the number of induced dipoles per volume. The dielectric polarization is also $P = \epsilon_0(\epsilon - 1)E$. Therefore, if the electric field is not too large, the polarizability can be used instead of the dielectric function. If the incident electric field with amplitude $\vec{E}_0$, wavevector $\vec{k}$ and angular frequency ω is

$$\vec{E}_i(\vec{r},t) = \vec{E}_0 \exp(i(\vec{k}\cdot\vec{r} - \omega t)), \tag{2.23}$$

then the magnitude of the scattered electric field at the detector (distance R from the sample ($R \gg r$)) is[58]

$$E_s(R,t) = \frac{E_0}{4\pi R\epsilon_0} \exp(i(kR - \omega t)) \int_V d^3r \exp(i\vec{q}\cdot\vec{r})\alpha(\vec{r},t) \tag{2.24}$$

and the autocorrelation of the electric field at a certain position of the detector is proportional to the autocorrelation of the Fourier components of the polarizability with wavevector $\vec{q}$, $\alpha(\vec{q},t) = \int_V d^3r \exp(i\vec{q}\cdot\vec{r})\alpha(\vec{r},t)$,

$$g_1(R,\tau) = \langle E^*(R,0)E(R,\tau)\rangle = \frac{k^4|E_0|^2}{16\pi^2R^2\epsilon_0^2} \langle\alpha^*(\vec{q},0)\alpha(\vec{q},\tau)\rangle \exp(-i\omega\tau). \tag{2.25}$$

The autocorrelation function of the electric field is

$$g_1(R,\tau) = \langle E^*(R,0)E(R,\tau)\rangle = \lim_{T\to\infty} \frac{1}{T} \int_0^T dt E^*(R,t)E(R,t+\tau). \tag{2.26}$$

The experimentally measured quantity is the intensity autocorrelation function $g_2(R,\tau)$,

$$g_2(R,\tau) = \langle I(R,0)I(R,\tau)\rangle = \lim_{T\to\infty} \frac{1}{T} \int_0^T dt I(R,t)I(R,t+\tau). \tag{2.27}$$

The intensity at position R and time t is $I(R,t)$. Under the assumption that the scattering volume is divided into a large number of independent smaller volumes, the electric field autocorrelation function and the intensity autocorrelation function

are connected via the Siegert relation:

$$g_1(\tau) = \beta\sqrt{1 + g_2(\tau)}. \tag{2.28}$$

For a dilute solution of N macromolecules the polarizability is given by

$$\alpha(\vec{r}, t) = \sum_{j=1}^{N} \alpha_j \delta(\vec{r} - \vec{r_j}), \tag{2.29}$$

with the polarizability α_j of molecule j. The Fourier transform of this expression is $\alpha(\vec{q}, \tau) = \sum_{j=1}^{N} \alpha_j \exp(i\vec{q} \cdot \vec{r}_j(\tau))$. If the polarizability is the same for each molecule and the solution is dilute,

$$g_1(R, \tau) \propto < N > \langle \exp[i\vec{q} \cdot (\vec{r}_j(\tau) - \vec{r}_j(0))] \rangle = < N > I_s(\vec{q}, \tau). \tag{2.30}$$

As was explained above, the self-intermediate scattering function $I_s(\vec{q}, \tau)$ is related to the self-correlation function $G_s(\vec{R}, \tau)$ via a Fourier transform. I If there are M particle spezies in solution, $I_s(\vec{q}, \tau)$ is the sum of M exponential terms. The decay rate is related to the respective size of each particle spezies[58].

Neutron scattering

This section on neutron scattering is based on chapters 2 and 5 in the book by M. Bée[60]. The double differential scattering cross section is introduced. Moreover the incoherent and coherent intermediate scattering functions are discussed. Finally, the incoherent scattering function is given for the case of Brownian diffusion.

Neutrons coming from a reactor are moderated at a certain temperature T. After the moderator the neutron velocities are distributed according to the Maxwell distribution with a mean velocity given by

$$\frac{1}{2}mv^2 = \frac{3}{2}k_B T. \tag{2.31}$$

m is the neutron mass and k_B is Boltzmann's constant. Different from the scattering cross section for X-rays, neutron scattering cross sections do not depend on the atomic number. For each isotope the neutron scattering cross section has to be determined experimentally. Table 2.1 shows the coherent and incoherent scattering cross sections σ_{coh} and σ_{inc} of hydrogen, deuterium and vanadium. For a sample consisting of N atoms the double differential scattering cross section is

$$S(\vec{q}, \omega) = \frac{1}{4\pi N} \frac{k}{k_0} \left[\sigma_{coh} S_{coh}(\vec{q}, \omega) + \sigma_{inc} S_{inc}(\vec{q}, \omega)\right]. \tag{2.32}$$

Here, $\vec{k_0}$ is the wavevector of the incoming neutron beam and $\vec{k}$ is the wavevector

Table 2.1: *Neutron scattering cross sections for selected isotopes: hydrogen, deuterium and vanadium.*

	hydrogen	deuterium	vanadium
σ_{coh} (barns)	1.8	5.6	0.03
σ_{inc} (barns)	79.9	2.0	5.1

of the outgoing neutron beam. The coherent and incoherent scattering functions are the Fourier transforms of the coherent and incoherent intermediate scattering functions,

$$S(\vec{q},\omega)_{coh,inc} = \frac{1}{2\pi}\int_{-\infty}^{\infty} I(\vec{q},t)_{coh,inc}\exp(-i\omega t)dt. \tag{2.33}$$

The coherent intermediate scattering function is

$$I(\vec{q},t)_{coh} = \frac{1}{N}\sum_{i,j}\left\langle \exp(i\vec{q}\cdot\vec{r}_i(t))\exp(i\vec{q}\cdot\vec{r}_j(0))\right\rangle . \tag{2.34}$$

It probes the collective motion of the atoms and via a spatial Fourier transform it is related to the pair correlation function which, given that a particle is at the origin at time 0, gives the probability that another or the same particle is at position $\vec{r}$ at time t. The incoherent intermediate scattering function is

$$I(\vec{q},t)_{inc} = \frac{1}{N}\sum_{i}\left\langle \exp(i\vec{q}\cdot\vec{r}_i(t))\exp(-i\vec{q}\cdot\vec{r}_i(0))\right\rangle . \tag{2.35}$$

The incoherent intermediate scattering function is related to the self correlation function which via a spatial Fourier transform is related to the self correlation function. The self correlation function, given that a particle is at the origin at time 0, gives the probability that the same particle is at position $\vec{r}$ at time t.

The case of Brownian diffusion was already treated in the previous section on dynamic light scattering. The intermediate scattering function is the solution of the Fourier transformed diffusion equation (eq. 2.20). An inverse Fourier transform in the time-frequency domain transforms the incoherent or self- intermediate scattering function into the incoherent scattering function. Thus, in the case of Brownian diffusion the incoherent scattering function is a Lorentzian function, given by [60]

$$S_{inc}(\vec{q},\omega) = \frac{1}{\pi}\cdot\frac{Dq^2}{\omega^2+(Dq^2)^2}. \tag{2.36}$$

After this general section on neutron scattering, the following two sections will briefly explain both neutron backscattering and neutron spin-echo.

Neutron backscattering

Neutron backscattering probes the total scattering function $S(q, \omega)$. There are two different neutron sources, reactors and spallation sources. Reactors provide a continuous beam whereas at spallation sources the beam is pulsed. When neutrons come from a reactor, the beam has to be monochromatized for backscattering. At a spallation source, neutrons with different energies from one pulse can be divided by letting them fly a long path before reaching the sample. A monochromator is not needed in this case.

Based on chapter 3.3 in the book by M. Bée[60], this paragraph describes how a backscattering spectrometer at a reactor source works. Both the monochromator and the analyzer crystals operate in backscattering mode. This allows for high energy resolution $\Delta E/E$ which is obtained by differentiating Bragg's law, $\lambda = 2d\sin(\Theta)$,

$$\frac{\Delta E}{E} = \frac{2\Delta\lambda}{\lambda} = 2\cot(\Theta)\Delta\Theta + \frac{2\Delta d}{d}. \tag{2.37}$$

λ is the wavelength of the neutrons, d is the lattice spacing of the crystal and Θ is the angle of incidence[50]. The cotangent is zero at 90° which is why a high energy resolution is obtained in backscattering.

The monochromator crystal moves back and forth. The neutrons are reflected from the moving monochromator towards the sample. The incoming energy at the sample is varied due to the Doppler effect. When interacting with the sample, neutrons may loose or gain energy. The sample is surrounded by large analyzer crystals (e.g. Silicon 111) by which neutrons arriving from the sample are scattered back once again. The focus of the analyzers is at the position of the detectors which are tubes filled with He^3 gas[60].

Neutron spin-echo

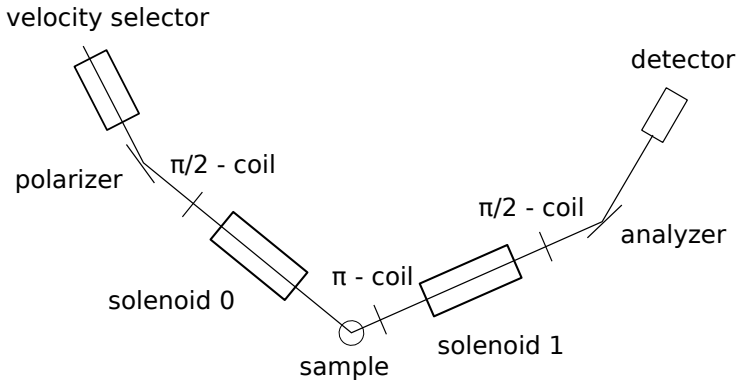

Figure 2.2: *Sketch of a NSE instrument. Reproduced from Mezei et al.[61] p. 9.*

The neutron spin-echo technique exploits the fact that the neutron has a spin. The basic setup of a NSE instrument is shown in Fig. 2.2. A NSE instrument has two

identical solenoids. The second solenoid can be tilted with respect to the first one. This tilt angle defines the scattering angle. The sample is located between the two solenoids. To explain the working principle of NSE, the path of one single neutron is followed here. After a polarizer, the neutron spin is aligned in the direction of propagation. A first $\pi/2$ coil rotates the spin vector by 90° such that the spin is oriented perpendicular to the direction of propagation. This allows the spin to undergo Larmor precession in the two solenoids. The neutron passes through the first solenoid. The number of rotations that the spin performs and the rotation angle Φ_0 of the spin vector after the first solenoid is determined by the velocity of the neutron. Then the neutron hits the sample. After the sample the spin is flipped by 180° to make the spin vector precess in the other direction in the second solenoid. The second solenoid produces exactly the same magnetic field as the first one. If the neutron did not gain or loose energy at the sample, it will make exactly the same number of rotations in the second solenoid but in the opposite direction. Thus, if the neutron does not change its energy at the sample, the final polarization (after the second solenoid) is similar to the initial polarization (before the first solenoid). If the neutron changes its energy, the the final polarization is different from the initial polarization. The total precession angle is (index 0 refers to the first solenoid, index 1 to the second solenoid)

$$-\Phi_0 + \Phi_1 = -\frac{\gamma H_0 l_0}{v_0} + \frac{\gamma H_1 l_1}{v_1} \approx \frac{\gamma H l}{m v_0^3} \hbar\omega \tag{2.38}$$

$H_{0/1}$ is the strength of the magnetic field, $l_{0/1}$ the length of the respective solenoid. γ is the gyromagnetic ratio of the neutron, m its mass and $v_{0/1}$ its respective velocity. The last approximate equality holds for $H_0 l_0 = H_1 l_1 = Hl$ and small velocity changes. The derivation of the approximate relationship is shown in more detail in the book by F. Mezei et al.[61]. The detector analyzes the difference between initial and final polarizations. A $\pi/2$ coil before the detector flips the part of the spin vector that was not changed due to the interaction with the sample, back into the direction of propagation. If the neutron changed its velocity at the sample, there is a P_x component of the polarization that remains perpendicular to the direction of propagation:

$$P_x = \langle \cos(-\Phi_0 + \Phi_1) \rangle = \langle \cos(\omega t) \rangle \,. \tag{2.39}$$

Here, the Fourier time is defined as $t = \gamma \hbar H l / (m v^3)$. The energy distribution is given by the total scattering function $S(\vec{q}, \omega)$. The polarization in x-direction is thus identical to the normalized intermediate scattering function,

$$P_x = \frac{\int S(\vec{q}, \omega) \cos(\omega t) d\omega}{\int S(\vec{q}, \omega) d\omega} = \frac{I(\vec{q}, t)}{I(\vec{q}, 0)}. \tag{2.40}$$

Similar to dynamic light scattering, NSE measures the intermediate scattering function[60;61].

Chapter 3

Experimental

This chapter first gives some details on the proteins and salts that were used. Then there is a section on UV-visible spectrometry which was used to determine protein concentrations. The SAXS beamline at the ESRF, the laboratory X-ray source, the light scattering device and the NBS and NSE spectrometers at Institut Laue-Langevin (ILL) are introduced. Moreover, SAXS, NBS and NSE data treatment is explained.

3.1 Materials and Sample Preparation

3.1.1 Proteins and salts

Bovine serum albumin (BSA) was used as a model protein that is globular and relatively cheaply available. Structures of BSA are deposited in the protein data bank (*www.rcsb.org*). One of them has the code 4F5S[62]. The tertiary structure of the protein is often described as heart-like. With $35 - 55\,\mathrm{mg/ml}$ serum albumins are abundant in the blood of mammals. They help to regulate the osmotic pressure and serve as vehicles for the transport of metabolites, hormones and drugs[62]. The molecular weight of a BSA monomer can be calculated using the tool at *web.expasy.org/protparam/* and the FASTA sequence of 4F5S from the protein data bank. The result is 66.5 kDa.

BLG served as another model protein. This protein is isolated from bovine milk. One of the structures that have been deposited in the protein data bank has the code 1BEB[63]. With the FASTA sequence of this structure the tool at *web.expasy.org/protparam/* delivers a molecular weight of 18.3 kDa of the BLG monomer. BLG belongs to the protein family of lipocalins and is the major whey protein. Its function is not fully clear. As all lipocalins it can bind hydrophobic molecules in its core. Its main function might however be to serve as a source of amino acids for the offspring[63;64].

Lyophilized powder of BSA (A7906, Sigma Aldrich) and BLG (L3908, Sigma Aldrich) was used as received and dissolved in ultrapure water (Millipore, 18.2 MΩcm) or in pure D_2O (Sigma Aldrich).

BSA was studied in aqueous solution with trivalent salts. YCl_3 (451363, Sigma Aldrich) and $LaCl_3$ (449830, Sigma Aldrich) salt was dissolved in ultrapure water

(Millipore, 18.2 MΩcm) or in pure D_2O.

For the solutions with salt, stocksolutions of protein and of salt were mixed by pipetting. BLG was used in purely aqueous solution of H_2O (part of the SAXS measurements) and D_2O (neutron experiments and other part of the SAXS measurements).

The samples for light scattering were prepared in a flow cabinet. All stock solutions and the ultrapure water were filtered through a 200 nm Nylon filter prior to mixing.

3.1.2 UV-visible spectrometry

UV-visible spectrometry was used to determine the protein concentration. The spectrometer that was used was a *Varian Cary 50 Scan*. The aromatic amino acids, namely tryptophan, tyrosine and phenylalanin absorb light at 280 nm [65]. Lambert-Beer's law states that

$$I(d) = I_0 \cdot \exp(-(\epsilon c d)/\log_{10}(e)) \tag{3.1}$$

where d is the distance that the light has travelled through the material (here the protein solution), c is the protein concentration and ϵ is the protein specific extinction coefficient. In the case of BSA it is $\epsilon_{BSA} = 0.667\,\mathrm{ml/(mg \cdot cm)}$. In the case of BLG it is $\epsilon_{BLG} = 0.96\,\mathrm{ml/(mg \cdot cm)}$ [66]. The transmission is

$$T = \frac{I}{I_0} = \exp(-(\epsilon c d)/\log_{10}(e)). \tag{3.2}$$

The absorbance A, which is used to calculate the protein concentration, is defined as

$$A = -\log_{10}\left(\frac{I}{I_0}\right) = \epsilon c d. \tag{3.3}$$

The protein concentration may thus be calculated as $c = A/(\epsilon d)$ [67].

3.2 Instruments

3.2.1 Beamline ID02 at the ESRF

The layout of the ID02 beamline at the ESRF is shown in Fig. 3.1. The ID02 beamline has an undulator source. A double monochromator (Si-111) selects the wavelength and a toroidal mirror focuses the beam on the detector. The detector is a CCD device. The wavelengths that can be selected are in the range from $\lambda = 1.55$ to 0.73 Å which corresponds to energies from 8 to 17 keV ($E = hc/\lambda = [12.4/(\lambda[\text{Å}])]\,\mathrm{keV}$). Recently, the detector tube has been enlarged such that now

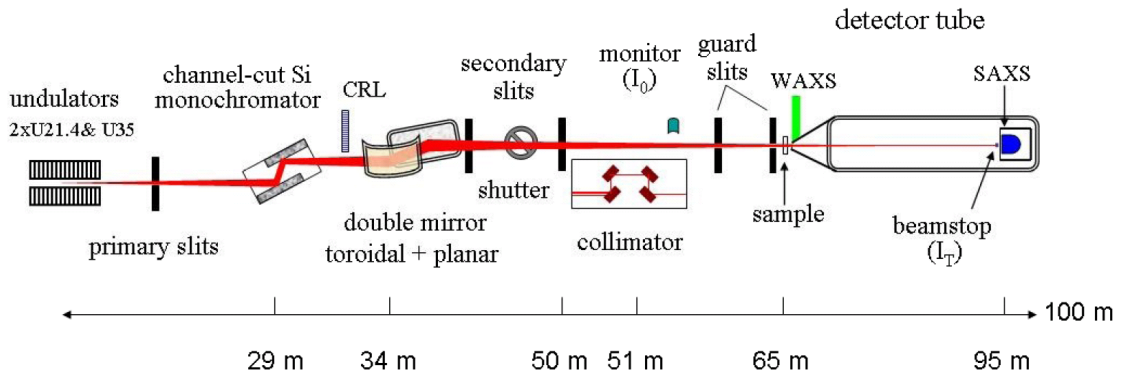

Figure 3.1: *Layout of the ID02 beamline at the ESRF*[68].

the sample-to-detector (SD) distance may maximally reach 30 m which is then a suitable configuration for ultra small angle X-ray scattering (USAXS) experiments which resolve structures in the μm range[68;69]. The experiments reported in this thesis were, however, performed at standard SD distances of 0.8, 2 and 5 m. This corresponds to q values between $2.6 \cdot 10^{-3}$ and $7.9 \cdot 10^{-1}$ Å^{-1}.

3.2.2 Home SAXS instrument

Figure 3.2: *Home SAXS instrument Xeuss 2.0 from XENOCS*[70].

As a laboratory X-ray source the *Xeuss 2.0* instrument from XENOCS SA (Sassenage, France) was used (Fig. 3.2). The source is a *GENIX3D* Cu Ultra Low Divergence device with a beam size of $1.1 \times 1.5\,\text{mm}^2$. It contains a mirror with a special multilayer coating that monochromatizes the beam by Bragg reflection. The

beam tube is evacuated. For the sample loading there are several options. Two of them are a flow through capillary and a standing capillary. The sample holder is mounted on motors which control the horizontal and vertical alignment of the sample. The length of the diffracted beam tube and thus the SD distance can be varied. The minimum q value that can be reached with the system is $0.0042\,\text{Å}^{-1}$. The maximum accessible q value is $1.42\,\text{Å}^{-1}$. The detector is a *Pilatus 3R 300K* from DECTRIS[71;72]. For the BLG measurements in D_2O a SD distance of 1846.54 mm was used, accessing a q range from $6.06 \cdot 10^{-3}$ to $3.28 \cdot 10^{-1}\,\text{Å}^{-1}$.

3.2.3 ALV CGS-3 SLS and DLS

Figure 3.3: *ALV CGS-3 SLS and DLS device (ALV GmbH, Langen, Germany).*

The *ALV CGS-3* SLS and DLS device (ALV GmbH, Langen, Germany) is shown in Fig. 3.3. It consists of a HeNe-Laser with a power of 22 mW operating at a wavelength of 632.8 nm. The detector is mounted on a goniometer arm which may rotate from 12° to 152° (scattering angle Θ, see also Fig. 2.1 and equation 2.1). The sample is filled into a glass cuvette which is then inserted into an index matching quartz glass vat which is filled with toluene. The index matching vat is further attached to a tubing system to allow for temperature control of the sample. For static light scattering the average intensity on the detector is recorded. For dynamic light scattering the autocorrelation function of the measured intensity has to be calculated. This is performed by the *ALV/LSE-5004* Multiple Tau Digital Correlator[73]. The measurements for this work were performed from 30° to 150°. With eq. 2.1 and the refractive index of water, $n_0 = 1.3320$, the q values range from $6.85 \cdot 10^{-4}$ to $2.56 \cdot 10^{-3}\,\text{Å}^{-1}$.

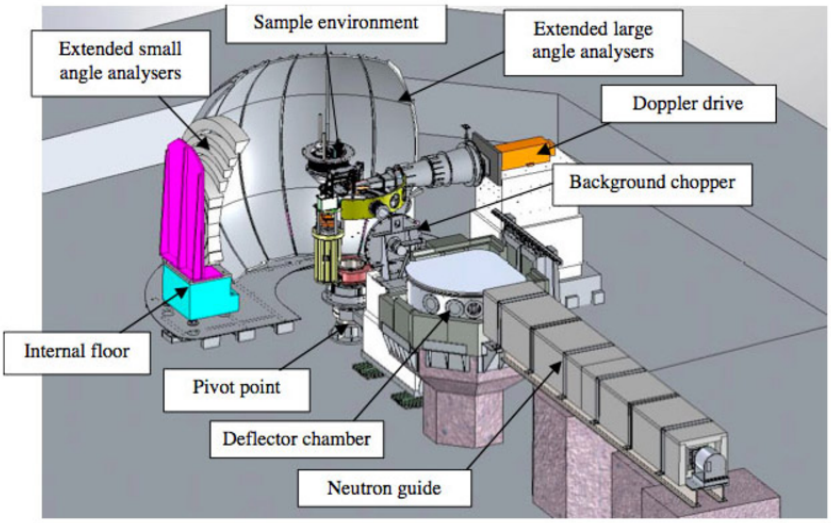

Figure 3.4: *IN16B instrument at the ILL in Grenoble, France. The image is taken from the ILL homepage*[74].

3.2.4 NBS spectrometer IN16B at ILL

Fig. 3.4 shows the neutron backscattering spectrometer IN16B at the ILL in Grenoble, France[74]. The energy resolution of the IN16B instrument is about 1 μeV. With unpolished Si(111) monochromator and analyzer crystals, the elastically measured wavelength is 6.27 Å. The maximum velocity of the Doppler machine is 4.5 m/s. This maximum velocity results in an accessible energy range from −30 to 30 μeV. These values are from personal communication with Dr. Tilo Seydel, instrument responsible for IN16B at the ILL.

3.2.5 NSE spectrometer IN15 at ILL

Fig. 3.5 shows the layout of the IN15 spectrometer. There are three different modes in which it can operate. The standard mode, a time of flight (TOF) mode and a focusing mode. The sketch in Fig. 3.5 shows the standard mode. The IN15 NSE spectrometer has a high energy resolution and can therefore investigate slow dynamical processes. It uses neutrons with wavelengths from 8 to theoretically 25 Å. Principally, in the standard mode Fourier times from 0.03 to 360 ns are accessible. The q range spans from 0.01 to 0.6 $Å^{-1}$. If the focussing mirror is used, the q value may even be reduced down to 0.002 $Å^{-1}$ which closes the gap to the q values accessed by light scattering[76;77].

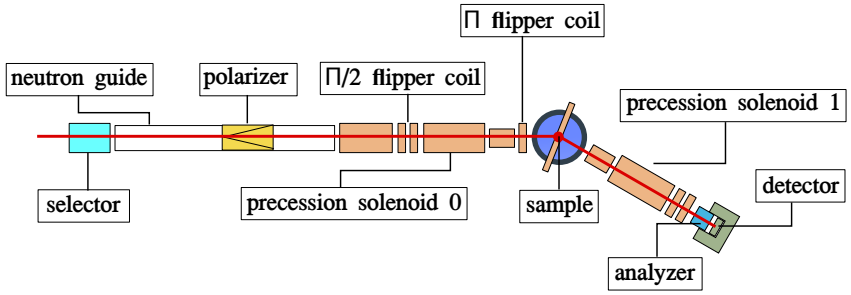

Figure 3.5: *IN15 spin-echo instrument at the ILL in Grenoble, France. The image is redrawn after a sketch on the ILL homepage*[75].

3.3 Data Treatment and Analysis

3.3.1 SAXS data

The SAXS data from beamline ID02 at the ESRF was treated as follows. A background of either pure water or salt solution was subtracted from the data. The intensity was then calibrated to absolute values by employing the absolute scattering cross section of pure water which is $1.65 \cdot 10^{-2}\,\mathrm{cm}^{-1}$ [78]. For this absolute calibration the water scattering of a flat region at large q values was taken into account. From the home SAXS data pure D_2O was subtracted as a background. The data was not calibrated to absolute intensities. The measured data was then fitted using the methods implemented in the NIST Center for Neutron Research (NCNR) package for *Igor Pro 6.3*.

For the analysis of the BLG data, an experimental structure factor was calculated by dividing the data through an ellipsoid form factor obtained by A. Sauter with half axis of rotation $R_a = 38\,\text{Å}$ and half axis $R_b = 19\,\text{Å}$ [79].

To calculate the form factors for the fits, the National Institute of Standards and Technology (NIST) script *UniformEllipsoid.ipf* was used. This code calculates the form factor $P(q)$ based on the form factor of a sphere, see also equation 2.4 and the publication by S. Kline et al. as well as the *SANS Model Function Documentation* from the NIST [51;80].

This form factor model was combined with structure factor models. In this work, three different structure factor models were employed. The corresponding potentials were shown in chapter 2. The screened Coulomb structure factor is implemented in the code *HPMSA.ipf* from NIST [51;54;55]. The sticky hard sphere structure factor is implemented in the code *StickyHardSphereStruct.ipf* [51;57]. The Two-Yukawa structure factor is implemented in *Two_Yukawa.ipf* [24;51].

3.3.2 NBS and NSE data

Here the data treatment for NBS and NSE data will be briefly explained. The NBS data was fitted by the following model:

$$S(q,\omega) = \mathcal{R} \otimes \{\beta \left[A_0 \cdot \mathcal{L}\left(\gamma,\omega\right) + (1 - A_0) \cdot \mathcal{L}\left(\gamma + \Gamma,\omega\right)\right] + \beta_{D_2O} \mathcal{L}\left(\gamma_{D_2O},\omega\right)\}\,. \quad (3.4)$$

The model contains two Lorentzian functions $\mathcal{L}\left(\gamma,\omega\right)$ and $\mathcal{L}\left(\gamma+\Gamma,\omega\right)$. The smaller width γ accounts for the global motion of the whole protein molecule. The larger width Γ accounts for the internal motions in the protein molecule. A_0 is the elastic incoherent structure factor (EISF). β is a scalar. β, A_0, γ and Γ are fit parameters. The q and temperature dependence of γ_{D_2O} was previously determined by Grimaldo et al.[81] using time-of-flight neutron spectroscopy. The scattering intensity of a pure D_2O sample at IN16B is adjusted by accounting for the D_2O content in the sample. This adjusted intensity is β_{D_2O}. To obtain the resolution function $\mathcal{R}$ of the instrument, vanadium, a purely isotropic scatterer was measured. The vanadium spectra were fitted using a sum of four Gaussian functions. The measured total scattering functions $S(q,\omega)$ were then fitted with the convolution of the resolution function and the sum of the three Lorentzian functions as shown in equation 3.4. Further details on NBS data treatment are given in the publication by Grimaldo et al.[81].

The intermediate scattering functions obtained from NSE were fitted with an exponential function $\exp(-Dq^2\tau)$ to obtain the diffusion coefficient D. For further information on NSE data treatment see the method part of publication B and the references cited there.

Part II

Results & Discussion

Chapter 4

Publication A. *Isotope Effects on Effective Interactions and Phase Behavior in Protein Solutions in the Presence of Multivalent Ions*

J. Phys. Chem. B ***121*** *(2017), 1731–1739.*

Michal K. Braun, Marcell Wolf, Olga Matsarskaia, Stefano Da Vela, Felix Roosen-Runge, Michael Sztucki, Roland Roth, Fajun Zhang and Frank Schreiber

Contributions	
Research design	*FS, FZ, RR*
Experiments	*MB, MW, OM, SDV, FZ*
Technical Assistance	*MS*
Data analysis and interpretation	*MB, FZ, FRR, FS, RR*
Paper writing	*MB, FZ, FS*

We have studied the influence of the isotopic composition of the solvent (H_2O or D_2O) on the effective interactions and the phase behavior of the globular protein bovine serum albumin (BSA) in solution with two trivalent salts ($LaCl_3$, YCl_3). Protein solutions with both salts exhibit a reentrant condensation phase behavior. The condensed regime (regime II) in between two salt concentration boundaries ($c^* < c_s < c^{**}$) is significantly broadened by replacing H_2O with D_2O. Within regime II liquid-liquid phase separation (LLPS) occurs. The samples that undergo LLPS have a lower critical solution temperature (LCST). The value of LCST decreases significantly with increasing solvent fraction of D_2O. The effective protein-protein interactions characterized by small-angle x-ray scattering (SAXS) demonstrate that while changing the solvent has negligible effects below c^*, where the interactions are dominated by electrostatic repulsion, an enhanced effective attrac-

tion is observed in D_2O above c^* in consistency with the observed phase behavior. As the LCST-LLPS is an entropy-driven phase transition, the results of this study emphasize the role of entropy in solvent isotope effects.

4.1 Introduction

The quantitative description of the effective protein-protein interactions in aqueous solutions is one of the major challenges in research of soft and biological matter[82–87]. As the effective interactions control the exact phase behavior of protein solutions including crystallization, a complete picture of protein interactions at different length scales with various control parameters could ease the search of optimal conditions for crystal growth. Protein phase behavior is also crucial for a better understanding of protein aggregation-related physiological diseases. In particular, the existence of a metastable liquid-liquid phase separation (LLPS) in protein solutions is a fundamental biophysical phenomenon and provides a mechanism for biological structure formation[82;84;87–92]. It serves as a prerequisite for the formation of crystals in cataracts[88;91;92] and for fibers responsible for sickle cell anemia and Alzheimer's disease[82;89], and influences the pathways of protein crystallization[84;93;94].

Effective interactions of biological macromolecules in aqueous solution are generally complex. They depend on a number of environmental parameters[31;85–87;95–104], such as concentration and valence of salt ions, the type of salt (e.g. Hofmeister series), concentration of additives (e.g. non-adsorbing polymers, co-solvents), pH and temperature. Possible mechanisms to change protein interactions are, among others, the control of protein surface charge and the tuning of hydrophobic and hydrophilic interactions. Furthermore, there is a whole arsenal of different types of interactions including Coulombic interaction, hydrogen bond formation, hydrophobic interaction and formation of salt bridges, which may be either highly specific or non-specific. The diversity of interactions leads to a rich phase behavior in protein solutions. Despite the complexity, progress has been made in modeling the liquid-liquid phase transition in protein and colloid systems, emphasizing the role of the short-ranged attraction[93;94;99;105–108].

Among the various environmental parameters, the solvent isotope effect on the effective interactions between proteins is still far from clear. The impact of the isotopic composition of the solvent depends very much on the circumstances and on the observable of interest. The physicochemical properties of D_2O are very similar to those of H_2O. It is thus commonly believed that the substitution of H_2O with D_2O causes only a very small perturbation of the structural preferences of a solute. In fact, in many biophysical studies using neutron scattering, infrared and NMR spectroscopy, D_2O is widely used as the solvent to obtain a useful signal[109;110]. In all these studies, it is generally assumed that D_2O has a negligible effect on the structure and interactions of these biological systems. However, while the effect of

D_2O is generally considered weak in biological systems, studies have shown significant changes in the interactions between proteins and their dynamics when H_2O is exchanged against D_2O. For instance, it has been found that D_2O can stabilize proteins against thermal denaturation [111–116], and influence the macromolecular dynamics in *E.coli* [117].

Some studies have found that the effective protein-protein attraction can be enhanced when H_2O is replaced by D_2O [109;110;118;119]. Gripon et al. investigated the effective interactions in lysozyme solutions in H_2O and D_2O in order to understand the lower solubility of lysozyme in D_2O. The solubility line is shifted to higher temperatures by about 7.2 °C in D_2O. SANS measurements and data analysis based on the second virial coefficient indicate that the repulsive potential due to the net surface charge does not change. The attraction between lysozyme molecules, however, is stronger in D_2O than in H_2O. It is assumed that this is due to hydrophobic, hydration and salt-specific interactions.

A recent study by Bucciarelli et al. [110] on γB-crystallin solutions has shown an even stronger solvent isotope effect. Replacing H_2O by D_2O results in an increase of the critical LLPS temperature of up to 16 °C. While this systematic study demonstrates that the variation of the critical temperature can be described using the extended law of corresponding states [107;120], the underlying physical mechanism of the solvent isotope effect is still not clear [110].

We have shown previously that trivalent salts such as YCl_3 can induce a reentrant condensation (RC) phase behavior in several acidic proteins [1;2;46;121;122]. For a given protein concentration, when the salt concentration is below a certain value c^*, or above a value c^{**} (with $c^* < c^{**}$), protein solutions are clear. At salt concentrations between c^* and c^{**}, protein condensation occurs including aggregation or clustering, LLPS and crystallization [3;47;48;123]. In particular, the metastable LLPS has been demonstrated to be an entropy-driven process as the system exhibits a lower-critical solution temperature (LCST) phase behavior [45]. The charge inversion and the effective attraction mediated via multivalent metal ions have been further investigated by experiments, simulations and theoretical studies [46;122;124–128]. However, in spite of the details known about the macroscopic phase behavior and the interactions, the microscopic origin of the short-ranged attraction is not yet completely clear [45;48].

In this work, we perform a systematic study of the effective interactions and the phase behavior of the protein bovine serum albumin (BSA) in solution with two different trivalent salts (YCl_3 and $LaCl_3$) in both H_2O and D_2O. Our goal is to explore the solvent isotope effect on the effective interactions and on the phase behavior which may shed light on the underlying mechanism of the solvent isotope effect and the entropy-driven LLPS.

4.2 Experimental

4.2.1 Material and Sample Preparation

BSA (product No. A7906), $LaCl_3$ (product No. 298182), YCl_3 (product No. 451363) and D_2O were purchased from Sigma Aldrich and used as received. For the stock solutions, protein and salt were dissolved in D_2O or in degassed Milli-Q H_2O (18.2 MΩcm conductivity).

The state diagrams of protein solutions with $LaCl_3$ at room temperature in D_2O and H_2O were determined by visual inspection or UV-vis transmission measurements. In H_2O, samples in regime II became difficult to judge by eye as samples turned only slightly turbid in regime II and no macroscopic phase separation occurred. Therefore, UV-vis transmission measurements (Cary UV-visible spectrophotometer 50 Scan, Varian Australia Pty Ltd) were used to determine the boundaries of regime II. This method worked very well for BSA concentrations up to 100 mg/ml. Example plots of the UV-vis transmission measurements and the determination of boundaries were presented in Fig S1. For higher protein concentrations (e.g.150 mg/ml), the boundaries were determined by visual inspection again. The state diagram of protein solutions with YCl_3 and different solvent fractions of D_2O was determined by visual inspection. To discriminate between LLPS and aggregation, the turbid samples were examined using a transmission microscope (AxioScope A1, Zeiss) equipped with an AxioCam ICc5 CCD camera.

4.2.2 Determination of the LCST

The dependence of the transition temperature on the solvent fraction of D_2O was determined using a UV-visible spectrometer equipped with a water bath for temperature control (Haake A10B and SC 150, Thermo Fisher Scientific Inc.). The sample was slowly heated from a bath temperature of 12 °C with a heating rate of 0.1 °C/min. The temperature of the sample solution was calibrated using a thermocouple attached to the sample holder. At a heating rate of 0.1 °C/min the sample temperature T_s was given by $T_s = (0.092 \cdot t + 12)$ °C, with the time t in minutes after the start of the experiment. The absorbance spectra in the range of 500-800 nm were collected in every 2 minutes and the intensity were integrated and plotted vs. temperature. The LCST was determined from the main peak of the first derivative of the integrated absorbance as a function of temperature. Prior to the UV-vis measurement the samples were centrifuged for 2 min with a RCF of 6860×g in order to remove large aggregates.

4.2.3 Small-Angle X-ray Scattering (SAXS)

The effective protein - protein interactions in the solutions were characterized by SAXS. SAXS experiments were performed at beamline ID02 at the ESRF, Grenoble,

France. The X-ray energy was 16 keV, which corresponds to a wavelength of 0.77 Å. For all measurements the sample-to-detector distance was set to 2 m, covering a q-range of 0.005 to 0.5 $Å^{-1}$. The data were collected by a high-sensitive fiber-optics coupled CCD detector placed in an evacuated flight tube. Samples were prepared right before the measurement. The protein solution was loaded into a flow-through quartz capillary with a diameter of 2 mm and a wall thickness of 0.01 mm. The data sets were reduced by subtracting the scattering of a pure salt solution as a background and by normalizing to absolute intensity. Further details on q-resolution, calibration and data reduction can be found in Ref.[129;130]. Data fitting was performed using IGOR Pro with macros provided by NIST[80].

4.3 Results

4.3.1 Phase behavior and effective interactions of BSA-$LaCl_3$ in H_2O and D_2O

We first present the phase behavior of BSA with $LaCl_3$ in both pure H_2O and D_2O, respectively, at room temperature. As shown in Fig. 4.1, a reentrant condensation is found in both cases[121]. The solutions are clear below the salt concentration c^* (regime I). In between c^* and c^{**} (with $c^{**} >> c^*$) condensation takes place, this is the so-called regime II. Above the salt concentration c^{**} the protein solutions reclarify (regime III). However, the macroscopic appearance of the solutions in regime II is different in H_2O and D_2O. Solutions in H_2O are only slightly turbid between c^* and c^{**}. There is no macroscopic phase separation and no LLPS. After a few hours, small precipitates become visible at the bottom or on the wall of the cuvette. In D_2O the solutions are highly turbid and phase-separate macroscopically. Amorphous protein aggregates or droplets with a high protein density form right after mixing and sediment quickly. Fig. 4.1 also shows that, when replacing H_2O by D_2O, the area of regime II is significantly enlarged. A closer look at the two boundaries reveals that the c^* values in both cases are very similar. The value of c^{**} however, is higher in D_2O than in H_2O.

Table 4.1: *Determination of the LCST for a series of samples with 80 mg/ml BSA, 13 mM $LaCl_3$ and different D_2O solvent fractions.*

D_2O solv. frac.	0	0.05	0.10	0.15	0.20	0.25	0.30
c_p (mg/ml)	80.1	80.7	80.8	80.1	80.4	72.1	77.1
LCST (°C)	31.5	28.8	26.4	23.6	22.2	19.7	18.7

Fig. 4.2 presents the plots of the integrated UV-vis absorbance of samples with 80 mg/ml BSA, 13 mM $LaCl_3$ and solvent fractions of D_2O from 0 to 0.3 as a function of temperature. At the starting temperature, 12.0 °C, and after centrifugation,

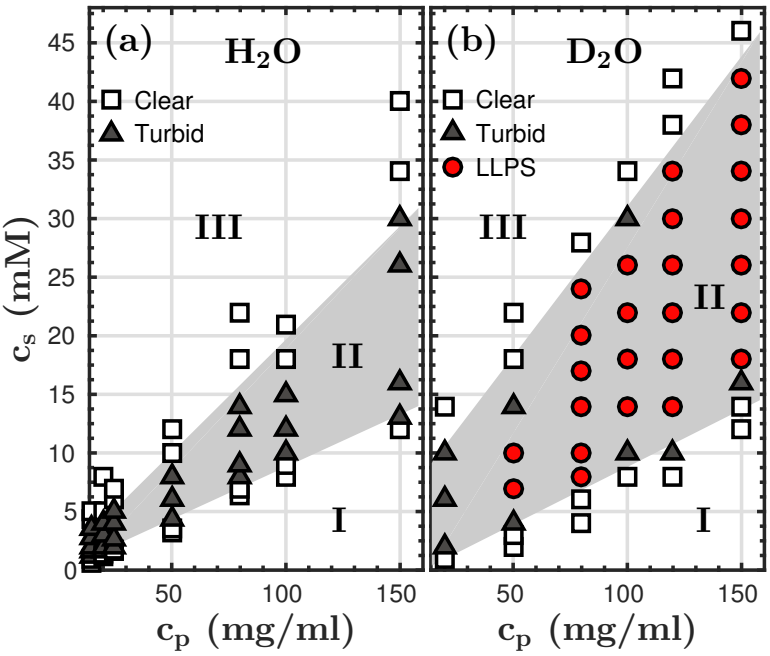

Figure 4.1: *Experimental state diagram of the BSA-$LaCl_3$ system at room temperature in both H_2O* ***(a)*** *and D_2O* ***(b)****. Shaded areas correspond to the condensed regime.*

all sample solutions are clear with an integrated absorbance close to zero. When increasing the temperature, a strong increase of the apparent absorbance occurs. The transition from low to high absorbance becomes sharper with increasing D_2O solvent fraction. The first derivative of the absorbance curve as a function of temperature was used to determine the exact LCST value, as shown in Fig. 4.2b. The peak position, i.e. the LCST of each sample, is plotted as a function of D_2O solvent fraction in Fig. 4.2c. When the D_2O solvent fraction increases, this transition temperature (the LCST) decreases dramatically. At a D_2O solvent fraction of 0.10, this value has decreased from 31.5 °C to 26.8 °C. Up to a D_2O solvent fraction of 0.20, the transition temperature decreases linearly. The slight deviation from the linear behavior at higher D_2O solvent fraction may be due to the formation of small amounts of protein aggregates as the protein concentration after centrifugation decreases with increasing D_2O solvent fraction (Table 4.1). At the highest investigated D_2O solvent fraction of 0.3, the LCST has decreased to 18.7 °C, which is already 12.8 °C lower than in pure H_2O. A further decrease of the LCST with increasing D_2O solvent fraction is expected. Due to the aggregation of protein it is difficult to investigate higher D_2O solvent fractions with our method. From a linear fit of the first five data points shown in Fig. 4.2c an LCST of -16.1 °C is obtained. This would be 47.6 °C below the LCST in pure H_2O.

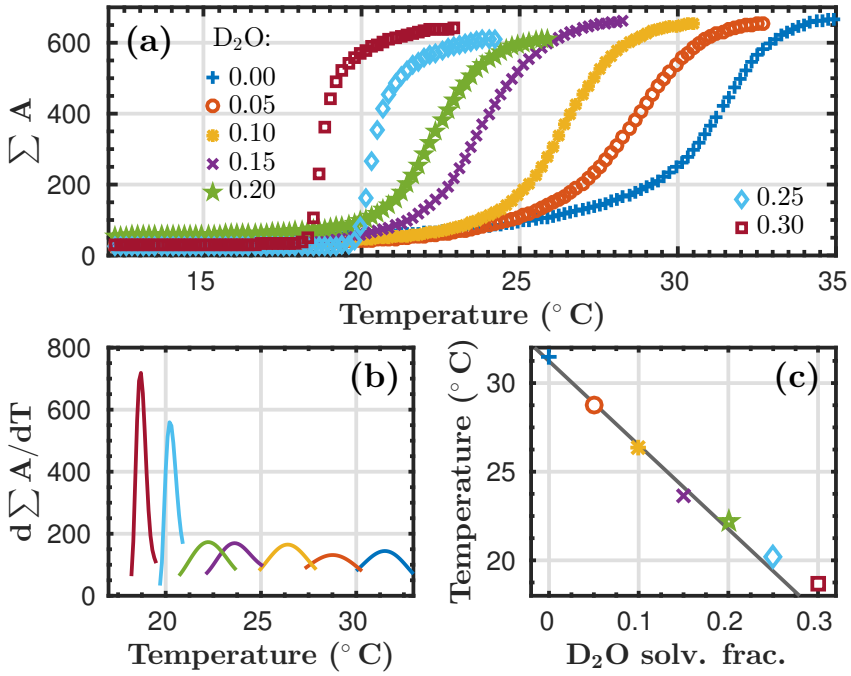

Figure 4.2: *LCST phase behavior of 80 mg/ml BSA with 13 mM $LaCl_3$.* ***(a)****: integrated absorbance ($\sum A$) (500-800 nm) vs. temperature for different D_2O solvent fractions.* ***(b)****: first derivative of the integrated absorbance with respect to temperature. The maximum determines the transition temperature.* ***(c)****: transition temperature as a function of D_2O solvent fraction. The line is a linear fit to the first five data points.*

4.3.2 Effective protein-protein interactions characterized by SAXS

For a quantitative understanding of the solvent isotope effects, we characterize the effective protein-protein interactions using SAXS. Representative SAXS profiles are shown in Fig. 4.3 for BSA-$LaCl_3$ solutions in both H_2O and D_2O as a function of salt concentration. In both cases, SAXS data show similar trends. At low salt concentration, the effective protein-protein interactions are dominated by the net negative charge. A strong correlation peak is visible. With increasing salt concentration, the low q intensity increases indicating the reduction of repulsion. In this region of the phase diagram (regime I), the solutions are clear.

With further increasing salt concentration the systems become more and more dominated by attractive interactions with the attraction reaching its maximum at 12 mM (H_2O) and 20 mM $LaCl_3$ (D_2O). In H_2O, starting from 15 mM the strength of the attraction starts to decrease. In D_2O the strength of the attraction starts to decrease at 25 mM. In D_2O the decrease starts at higher salt concentration which

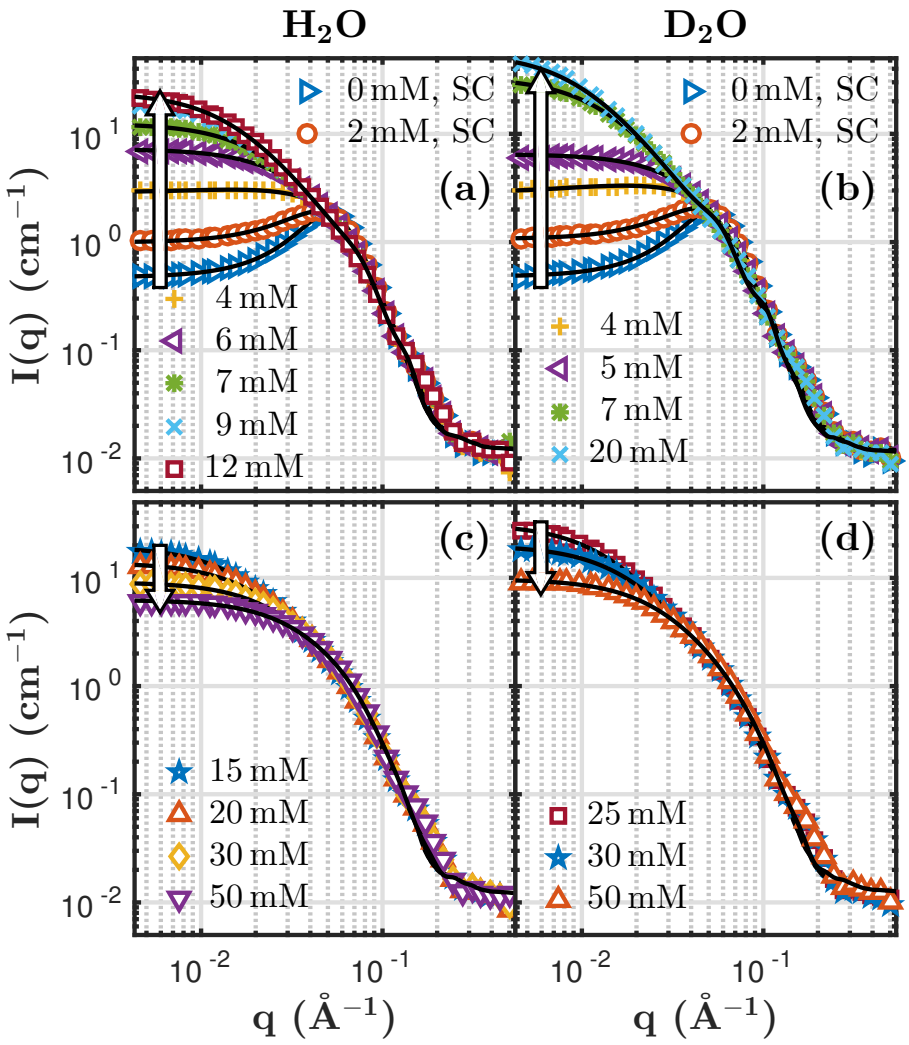

Figure 4.3: ***(a, c)****: SAXS data with model fits for samples in* H_2O *containing 85 mg/ml BSA.* ***(b, d)****: SAXS data with model fits for samples in* D_2O *containing 87 mg/ml BSA . The scattering intensity at low q increases with increasing salt concentration in* ***(a)*** *and* ***(b)****, and decreases in* ***(c)*** *and* ***(d)****. In the legend, SC indicates that the screened Columbic potential was used for data fitting. The other data were fitted using the SHS potential. For further information on the SAXS data analysis see the Supporting Information.*

corresponds very well to the finding that regime II also extends to higher salt concentrations (see also Fig. 4.1). The decrease is found to start very close to the upper boundaries (c^{**}) of the second regime. In H_2O c^{**}(80 mg/ml) is located at 16±2 mM. In D_2O c^{**}(87 mg/ml) is located at 26±2 mM in D_2O. The data with decreasing low q intensity are shown in the lower parts of the figure. SAXS profiles for a further set of data with 150 mg/ml BSA are shown in Fig. S2 in the Supporting Information.

In order to quantify the effective interactions, the SAXS data were fitted using models with an ellipsoid form factor and different interaction potentials. Fig. 4.3 presents the SAXS data with model fitting for BSA-$LaCl_3$ in H_2O and D_2O, respectively. The fits are superimposed on the data as solid black lines. The corresponding structure factors are shown in Fig. S3 in the Supporting Information. In both cases, below c*, the interactions are dominated by electrostatics due to the surface charges. The two scattering curves for samples with very low salt concentrations (0 and 2 mM $LaCl_3$) were fitted using a screened Coulombic potential in both H_2O and D_2O. In H_2O the fitted charges are (for 0 and 2 mM) 18.1 and 10.3 e, respectively. The ionic strength in H_2O is 7.4 and 10 mM. In D_2O the charges are 16.3 and 8.71 e. The ionic strength in D_2O is 6.2 and 8.6 mM. The values in H_2O are thus very similar to the ones in D_2O. Therefore, the *repulsive* part of the potential shows only a weak dependence on the solvent (H_2O or D_2O).

In regimes II and III, where the effective interactions are *attractive*, a strong isotope effect is observed. This interesting finding will be further discussed and explained in Section 4.

To quantitatively describe the attractive potential, the sticky hard sphere (SHS) potential was used[56]. A pertubative solution of the Percus-Yevick closure relation was used to calculate the structure factor[57]. The sticky hard-sphere model was introduced by Baxter[56] for a system with hard-core repulsion and additional short-range attraction, which can undergo fluid-vapor phase separation. The interaction potential for particles with radius R is

$$\beta U(r) = \begin{cases} 1 & r < \sigma = 2R \\ -\beta u_0 = \ln\left(\frac{12\tau\Delta}{\sigma+\Delta}\right) & \sigma < r < \sigma + \Delta \\ 0 & r > \sigma + \Delta. \end{cases} \tag{4.1}$$

The interaction potential is in units of k_BT ($\beta = 1/k_BT$), τ is the stickiness parameter and Δ is the width of the square well.

Frequently, for simplicity the limit $\Delta \to 0$ is considered. In this limit the reduced second virial coefficient is given by

$$\lim_{\Delta\to 0} \frac{B_2}{B_2^{HS}} = 1 - \frac{1}{4\tau}. \tag{4.2}$$

$B_2^{HS} = 16\pi R^3/3$ is the second virial coefficient of a hard sphere of radius R. For

the SAXS data fitting, Δ was fixed to $0.01\,\sigma$ to avoid artificial coupling with τ. Theoretical considerations and computer simulations[107;131;132] suggest that there is a universal value of $B_2/B_2^{HS} \approx -1.5$ at the critical point of the gas-liquid transition for various systems.

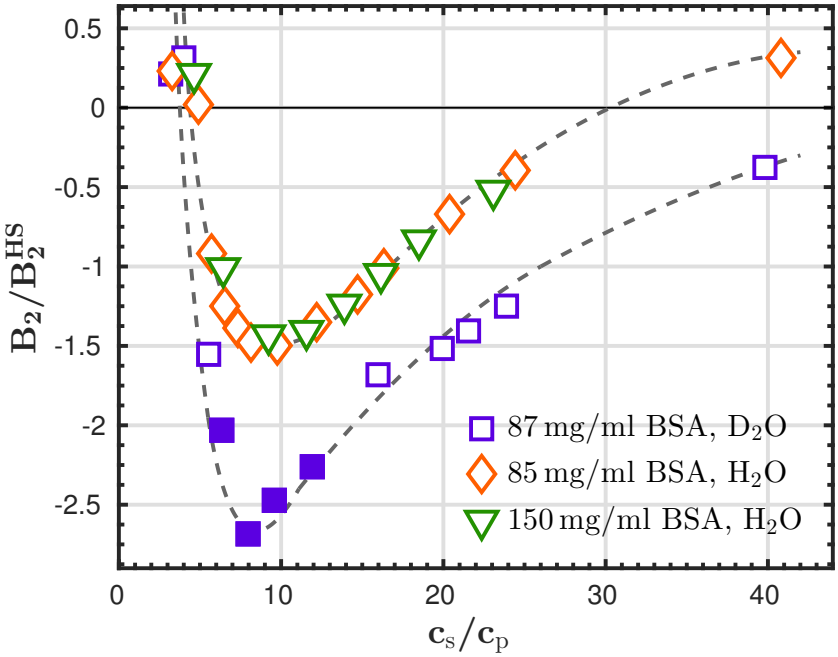

Figure 4.4: *Reduced 2nd virial coefficients calculated from the SAXS data analysis of BSA-$LaCl_3$ samples (Fig. 4.3) B_2/B_2^{HS} could be calculated for samples above c^*. Triangles and diamonds mark samples in H_2O. Samples in D_2O are marked by squares. The solid squares indicate samples showing LLPS. The dashed lines are guides to the eye.*

Fig. 4.4 summarizes the B_2/B_2^{HS} values calculated from the stickiness parameter obtained for samples in regimes II and III. The data are plotted against the normalized salt concentration, c_s/c_p. Results for two sets of samples with 150 and 85 mg/ml BSA in H_2O and for one set of samples with 87 mg/ml BSA in D_2O are shown. Dashed lines are added as guides to the eye. Remarkably, the two series measured for the BSA-$LaCl_3$ system in H_2O fall onto one common master curve. In H_2O, B_2/B_2^{HS} only touches -1.5 in its minimum. Clearly, the curve in D_2O is well below the one in H_2O. Thus, the strength of attraction is significantly enhanced in D_2O. The samples that showed macroscopic LLPS are marked by filled squares. B_2/B_2^{HS} for these samples is below -1.5, in agreement with findings reported by Wolf et al.[132]. Furthermore, B_2/B_2^{HS} first decreases quickly above c^*. After reaching the minimum, it starts to increase again but much more slowly. The reason for the non-symmetric change is most likely due to the screening effect of the

co-ion, Cl^-. The increasing amount of co-ions screens the effective surface charge of the proteins. Fujihara and Akiyama studied the attractive interaction between macroanions mediated by divalent cations and observed a similar trend of effective interaction potential as a function of cation concentration [125;127].

This quantitative interpretation and analysis of the SAXS data nicely fits to the qualitative macroscopic phase behavior in the different systems described above (Fig 4.1). The qualitative observations as well as the quantitative results show that the attraction is enhanced when H_2O is replaced by D_2O.

4.3.3 Effect of D_2O solvent fraction on the phase behavior and the effective interactions

The general phase behavior including LCST for BSA with YCl_3 in H_2O has been described in our previous work [45;48;121]. Here we focus on the effect of the solvent fraction of D_2O on the phase behavior. We first determined a state diagram for protein solutions with a fixed protein concentration (91.7 mg/ml BSA) as a function of YCl_3 concentration and the solvent fraction of D_2O. The results are summarized in Fig. 4.5. The shaded area indicates regime II. This state diagram shows that above a D_2O solvent fraction of 0.8 there is no LLPS anymore but only amorphous aggregation. For example, samples with 12 mM YCl_3 are all in the condensed regime (labeled with dashed green line). With increasing solvent fraction of D_2O, the condensed phase undergoes a transition from dense liquid droplets to amorphous protein aggregates. Direct observation on the morphology of the condensed phase using optical microscopy is presented in the Supporting Information (Fig. S4). In addition to the structural change of the condensed phase, we also observe a shift of the c^{**} boundary to higher salt concentrations with increasing solvent fraction of D_2O. The location of the c^* boundary stays more or less constant.

To further investigate the solvent isotope effect on the effective interactions, four series of samples with salt concentrations well below c^*, close to c^*, in regime II (between c^* and c^{**}) and slightly above c^{**} were measured by SAXS as a function of D_2O solvent fraction. The salt concentrations that were chosen for the SAXS experiments are marked by green lines in Fig. 4.5. The measured SAXS profiles are shown in Fig. 4.6.

Well below c^*, at $c_s = 0.5$ mM YCl_3, the scattering curves exhibit a correlation peak. This is the result of the long-range Columbic repulsion due to the net negative charge of the proteins. Varying the D_2O solvent fraction does not affect the scattering profiles and thus the effective interactions. This is in good agreement with the results for BSA with $LaCl_3$ at low salt concentrations which are presented in Fig. 4.3.

Slightly below c^* with $c_s = 5$ mM YCl_3, the correlation peak in SAXS profiles is vanished. An increase of the D_2O solvent fraction slightly shifts the scattering intensity at low q to higher values, indicating a slight increase of the attractive

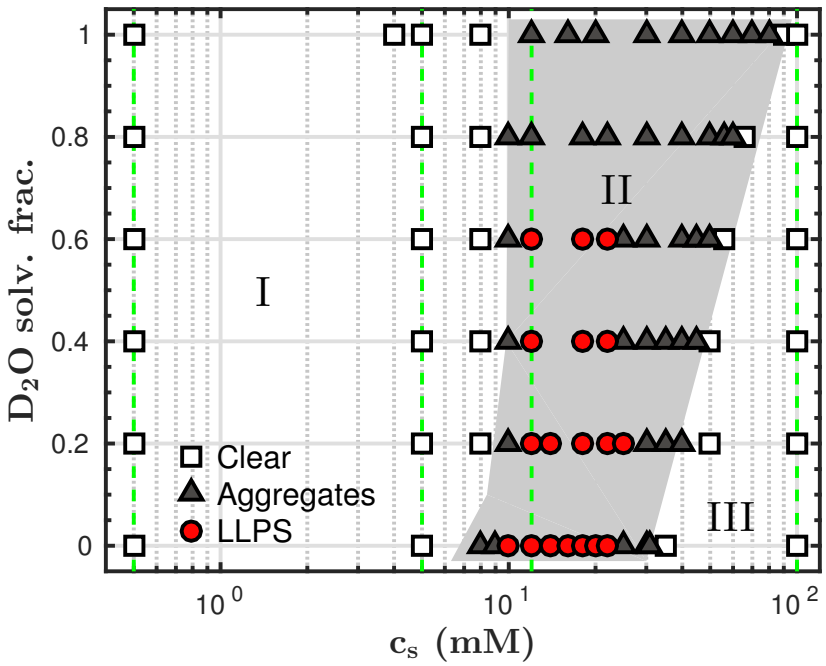

Figure 4.5: *Experimental state diagram for BSA with YCl_3 at different solvent fractions of D_2O. The BSA concentration was fixed at 91.7mg/ml. The shaded area corresponds to regime II. Sample series with selected salt concentrations for SAXS measurements were marked by green lines.*

interactions.

In regime II with 12 mM YCl_3 where macroscopic phase separation occurs as shown in Fig. 4.5. The samples were centrifuged and only the supernatant were used for SAXS measurements. The vertical shift of the SAXS profiles corresponds to the variation of the protein concentration in the supernatant. The downward shift of the SAXS profiles with increasing D_2O solvent fraction is consistent with an increase of attraction.

In regime III with 100 mM YCl_3 where the samples are clear again. The scattering intensity at low q and hence the attraction increases significantly with increasing D_2O solvent fraction. This is also consistent with the macroscopic phase behavior that the samples are closer to c^{**} with increasing D_2O solvent fraction (Fig. 4.5).

4.4 Discussion

We have studied the influence of the solvent isotope (H_2O vs D_2O) on the phase behavior of BSA solutions in the presence of two trivalent salts, $LaCl_3$ and YCl_3. While the reentrant condensation phase behavior is found under all experimental conditions (salt or solvent), LCST-LLPS occurs only under certain conditions. The

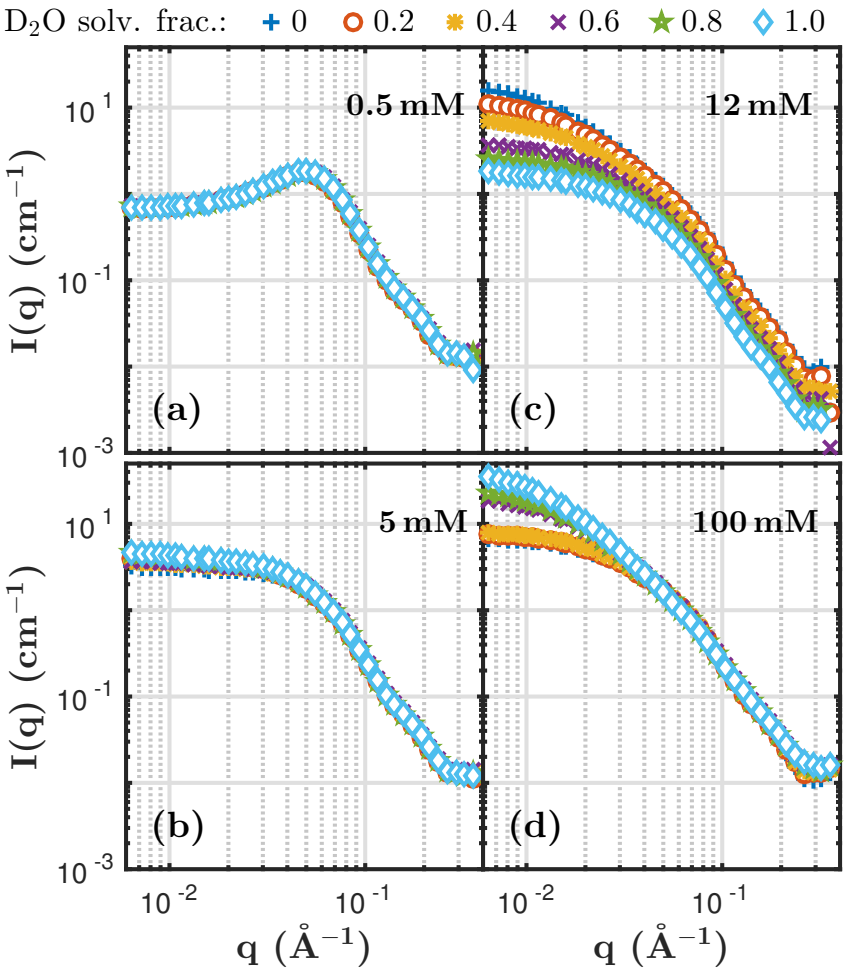

Figure 4.6: *SAXS profiles for samples in different regimes with BSA 91.7 mg/ml and varying solvent fractions of D_2O. The YCl_3 concentrations are given in each subplot (see also green dashed lines in Fig. 4.5).*

phase behavior found in different systems is summarized in Table 4.2. In the BSA-YCl_3 system, LLPS occurs in pure H_2O. At room temperature the region of LLPS shrinks with increasing D_2O solvent fraction until it vanishes in pure D_2O. In the BSA-$LaCl_3$ system however, LLPS occurs in pure D_2O at room temperature whereas in pure H_2O, LLPS occurs only at temperatures above 30 °C (Fig. 4.2). At room temperature, only mesoscopic protein clusters exist and there is no macroscopic phase separation.

The effective protein-protein interactions characterized by SAXS demonstrate that the attraction increases by replacing H_2O with D_2O (Fig. 4.4). This explains the phase behavior that is summarized in Table 4.2. In BSA-$LaCl_3$ in H_2O there is no LLPS at room temperature because the attraction is too weak. In BSA-YCl_3

Table 4.2: *Summary of LCST-LLPS phase behavior at room temperature.*

No.	Solvent	Salt	Macroscopic phase behavior in regime II	Attraction
1	H_2O	$LaCl_3$	mesoscopic clusters	too weak for LLPS
2	D_2O	$LaCl_3$	LCST - LLPS	suitable for LLPS
3	H_2O	YCl_3	LCST - LLPS	suitable for LLPS
4	D_2O	YCl_3	amorphous aggregates	too strong for LLPS

in D_2O there is no LLPS because the attraction is too strong and only amorphous aggregates are formed.

The strong decrease of the LCST with increasing D_2O solvent fraction should be compared to solvent isotope effects on the solubility of lysozyme. A difference of about 7.2 °C in D_2O versus H_2O was reported[109;118]. In another system, namely in solutions of γB-crystallin, the (upper) critical temperature of LLPS increases by 16 °C in D_2O versus H_2O[110]. While the 7.2 °C difference in protein solubility of lysozyme is consistent with the temperature difference of the maximum density of light and heavy water, the larger difference observed in γB-crystallin solutions and in the work presented here indicate that other contributions may play a crucial role.

The existence of a lower-critical solution temperature (LCST) phase behavior in our systems demonstrates that the LLPS is driven by entropy. Thus, the observed significant response of the effective interactions (mainly the attractive part) to the solvent composition in protein solutions must be due to the solvent isotope dependent entropy contribution. Before discussing further the possible entropy contribution, we emphasize that the protein condensation observed is not caused by a change of the protein structure induced by YCl_3 or $LaCl_3$. We have studied the stability of protein secondary structure in the presence of multivalent salts in H_2O and D_2O using circular dichroism (CD) and FTIR[1;130;133]. The consistency of the different techniques suggests that replacing H_2O by D_2O has no significant effects on the secondary structure of proteins. Moreover, the successful growth of high-quality crystals and structural analysis confirm that the proteins are still in their native state[47;79;133].

We have recently discussed the mechanism of the LCST phase behavior in our system based on the patchy colloid model. We propose that the key entropy contribution is due to the release of hydration water molecules upon ion bridging[45]. Upon heating both the carboxy-groups and the trivalent ions are partially dehydrated, resulting in a high entropy gain. Substitution of H_2O with D_2O certainly influences the hydration and dehydration of both proteins and cations. Unfortunately, studies on the hydrogen bonds in H_2O or D_2O for systems involving different types of functional groups turn out to be a great challenge[111;134–137]. Nevertheless, we find that these isotope effects lead to a higher entropy contribution for our system in D_2O which results in an enhanced effective attraction between proteins and a lower

LCST. The entropy contribution to the solvent isotope effects may also shed light on the unusual strong effects observed in other protein systems[109;110;118].

It is worth noting that although similar entropy-driven LCST phase behavior is common in some polymer solutions, the isotope effects of solvents are different. In some polymer (e.g. PNIPAM) solutions, replacing H_2O by D_2O *increases* the LCST by 1 or 2 °C[138;139], which is in contrast to our system where we observe a *significant decrease* of the LCST. This opposite trend of the solvent isotope effect may be due to the different types of entropy contributions involved. In aqueous solutions of polymers, the entropy contribution comes from the dehydration of the hydrophobic part of the molecules[139;140]. Therefore, the stability of this hydration shell is enhanced when H_2O is replaced by D_2O, leading to a higher LCST. In our system the entropy contribution comes from the reduced translational and rotational entropy of the hydration waters of the hydrophilic carboxyl groups on the protein surface and the metal cations. The different significance of the solvent isotope effect in polymer vs. protein systems might be due to the different levels of cooperation of the hydrogen bond or to the different amount of hydration water involved.

4.5 Conclusions

In this work, we have studied the effective protein-protein interactions and phase behavior in solutions with two trivalent salts ($LaCl_3$ and YCl_3). In particular, we focused on the solvent isotope effect when replacing H_2O by D_2O. For both systems in both solvents, a reentrant condensation phase behavior is observed. Within regime II, LCST-LLPS occurs under certain specific conditions. This rich phase behavior is highly sensitive to the D_2O solvent fraction. While c^* is weakly affected by replacing H_2O with D_2O, c^{**} shifts to higher salt concentrations resulting in a broadening of regime II. The LCST-LLPS phase behavior for both salts shows strong solvent isotope effects, as summarized in Table 4.2. The LCST decreases significantly with increasing D_2O solvent fraction. The effective protein-protein interactions characterized by SAXS are consistent with the observed phase behavior. At low salt concentrations below c^*, interactions are dominated by electrostatic repulsion which is not sensitive to the D_2O solvent fraction. Above c^* the effective interactions become attractive and strongly depend on the D_2O solvent fraction. The interaction potential can be well described using a sticky hard sphere model, indicating the short-ranged nature of the attraction. The reduced second virial coefficients, B_2/B_2^{HS}, decrease steeply first and increase again slowly after reaching a minimum with increasing salt concentration. Similar trends are observed in both H_2O and D_2O, but the values become more negative in D_2O, indicating an enhanced attraction. The entropy driven LCST phase behavior suggests that the origin of the short-ranged attraction is closely related to entropy, which is most likely due to the release of hydrated waters from both metal ions and protein surfaces upon ion

bonding[45]. The entropy contribution to the solvent isotope effects may also shed light on the unusual strong effects observed in other protein systems[109;110;118].

We thank R. Akiyama (Kyushu University, Japan) and G. Lotze (ESRF) for valuable discussions and help for data analysis. This work was supported by the Deutsche Forschungsgemeinschaft (DFG). Furthermore we thank the ESRF for allocation of beamtime on ID02. Olga Matsarskaia acknowledges a studentship by the Studienstiftung des Deutschen Volkes.

Chapter 5

Publication B. *Crowding-controlled cluster size in concentrated aqueous protein solutions: Structure, self- and collective diffusion*

J. Phys. Chem. Lett. ***8*** *(2017), 2590–2596.*

Michal K. Braun, Marco Grimaldo, Felix Roosen-Runge, Ingo Hoffmann, Orsolya Czakkel, Michael Sztucki, Fajun Zhang, Frank Schreiber and Tilo Seydel

Contributions	
Research design	*TS, FZ, FRR, FS*
Experiments	*MB, MG, TS, FZ*
Technical Assistance	*TS, OC, IH, MS*
Data analysis and interpretation	*MB, MG, FRR, TS, FZ*
Paper writing	*MB, FRR, TS, FZ, FS*

We report on the concentration-controlled formation of cluster in β-lactoglobulin (BLG) protein solutions, as evidenced by a combination of structural and dynamical scattering techniques. The static structure factor from small-angle X-ray scattering as well as de-Gennes narrowing in the nanosecond diffusion function $D(q)$ from neutron spin-echo spectroscopy evidence the formation of clusters. Using neutron backscattering spectroscopy, a monotonous increase of the average hydrodynamic cluster radius is monitored over a broad protein concentration range, corresponding to oligomeric structures of BLG ranging from the native dimers up to roughly four dimers. The results suggest that BLG forms compact clusters that are static on the observation time scale of several nanoseconds. The presented analysis provides a general framework to access the structure and dynamics of macromolecular assemblies in solution.

5.1 Introduction

The formation of protein clusters in aqueous solutions is of great fundamental and practical interest[34;35;141;142], for instance in the context of the rational parameter choice for controlled self-assembly, and for the delivery of highly concentrated protein-based drugs. Moreover, a systematic understanding of protein cluster formation is important in a context of exploring possible dynamic precursor processes of dynamical arrest, protein aggregation and crystallization[9;133;143;144]. Various parameters influence the formation and size of protein clusters, including the protein concentration, pH and salt-induced charges in the solutions[5;142]. Thus far, only very few protein solutions undergoing cluster formation have been investigated systematically with respect to both their nanometer structure and nanosecond dynamics.

Lysozyme represents the most comprehensively studied system in this context[31–35;39;104]. The existence of lysozyme protein clusters in aqueous solutions has been shown by Stradner et al.[31] using small-angle X-ray and neutron scattering (SAXS/SANS). The small-angle scattering studies on lysozyme solutions suggest that isotropic charge-mediated interactions consisting of a short-range attraction and a long-range repulsion cause the formation of clusters. Depending on the protein concentration three to ten proteins merge into a cluster[31;32;39]. From the static studies alone, the question of finite lifetime of the clusters remained controversial and inspired dynamics studies using neutron spin-echo spectroscopy (NSE)[34], setting the lower limit of the cluster lifetime to about 25 nanoseconds. Further studies observing diffusion on the much longer millisecond time scale found evidence for a finite lysozyme cluster lifetime on this scale[145;146].

So far, as summarized above, systematic studies of protein cluster formation addressing both static and dynamic aspects have focused on the lysozyme model system, employing SAXS/SANS, NSE, and NMR methods, complemented by theory and simulations[16;27;39;147–149]. A recent study, by Grimaldo et al.[5], systematically addressed the cation-induced formation of protein clusters of bovine serum albumin via neutron backscattering spectroscopy (NBS). This technique is promising for the study of clustering for two reasons: First, at short nanosecond time scales, the self-diffusion only depends on the individual cluster mobility in a hydrodynamic medium, and is not affected by encounters with other clusters. Second, by measuring at large scattering vectors, NBS unambiguously accesses the cluster self-dynamics independent of the cluster size, which has been challenged for NSE results due to the unclear convergence of collective to self-diffusion in attractive systems.

Here, we report on solutions of bovine β-lactoglobulin (BLG). Here, clustering is induced solely by a high protein volume fraction, i.e. by crowding, without the necessity for the presence of salt or a non-neutral pH. We combine structural investigations using SAXS with dynamic investigations using both NSE and NBS to arrive at a consistent picture on cluster formation and structure.

5.2 Results

5.2.1 Statics - Evidence for cluster formation in pure BLG solutions

Scattering profiles from SAXS are shown in Fig. 5.1A, displaying a clear concentration-dependent correlation peak at intermediate q. At high q, the scattering profiles are concentration-independent, and are clearly consistent with the form factor of a BLG dimer. This observation indicates the dominance of dimeric building blocks at all concentrations. We observe a similar behavior for BLG in both H_2O and D_2O (Supporting Information, Figure 1). The SAXS measurements have been repeated for different protein concentrations and BLG proteins from different batches.

The pronounced correlation peak in the SAXS profiles (Fig. 5.1A) indicates an overall repulsive interaction, and the peak position q_c is related to the averaged center-to-center distance $d_{cc} = 2\pi/q_c$ between proteins. Assuming a solution consisting solely of BLG dimers, the volume per dimer $V \propto d_{cc}^3$ shrinks linearly in dimer volume fraction ϕ. Thus, the peak position q_c should scale with $\varphi^{1/3}$ for a monodisperse system [8;150;151].

In contrast with this expectation, the peak position scales with a significantly smaller exponent. We employed four different methods to extract q_c from the data (Fig. 5.1C, see Methods for details), and fitted the function $q_c = a \cdot \varphi^b$ (lines in Fig. 5.1C, Table 1 in Supporting Information). First, we used the model-free peak positions of the SAXS intensity curves (blue squares, for method see Fig. 5.1A), resulting in an exponent of $b = 0.11 \pm 0.03$. Second, the peak positions of the experimental structure factors (yellow triangles, for method see Fig. 5.1B) yield $b = 0.13 \pm 0.03$. Third, peak positions of fitted structure factors based on a Two-Yukawa potential with short-range attraction and long-range repulsion result in $b = 0.10 \pm 0.03$ (purple diamonds). Forth, peak positions of fitted structure factors based on a screened-Coulomb potential yield an exponent of $b = 0.28 \pm 0.03$ (orange circles), deviating from the other methods.

To further quantify the deviation from a monodisperse system, we estimate the number density of clusters

$$n_{cluster} = \phi_{cp} \Big/ \left(\frac{1}{6}\pi d_{cc}^3\right) = \frac{q_c^3}{\pi^3\, 4\sqrt{2}} \ . \tag{5.1}$$

Here, we assume that imaginary, blown-up spheres around the clusters effectively have a packing fraction close to $\phi_{cp} = \frac{\pi}{3\sqrt{2}} \approx 0.74$ [152]. The number density for dimers as the basic building blocks of the clusters is given from the sample preparation as

$$n_{\mathrm{d}imer} = \frac{m}{M_w} \cdot \frac{1}{(V_s + \theta_p \cdot m)} \ , \tag{5.2}$$

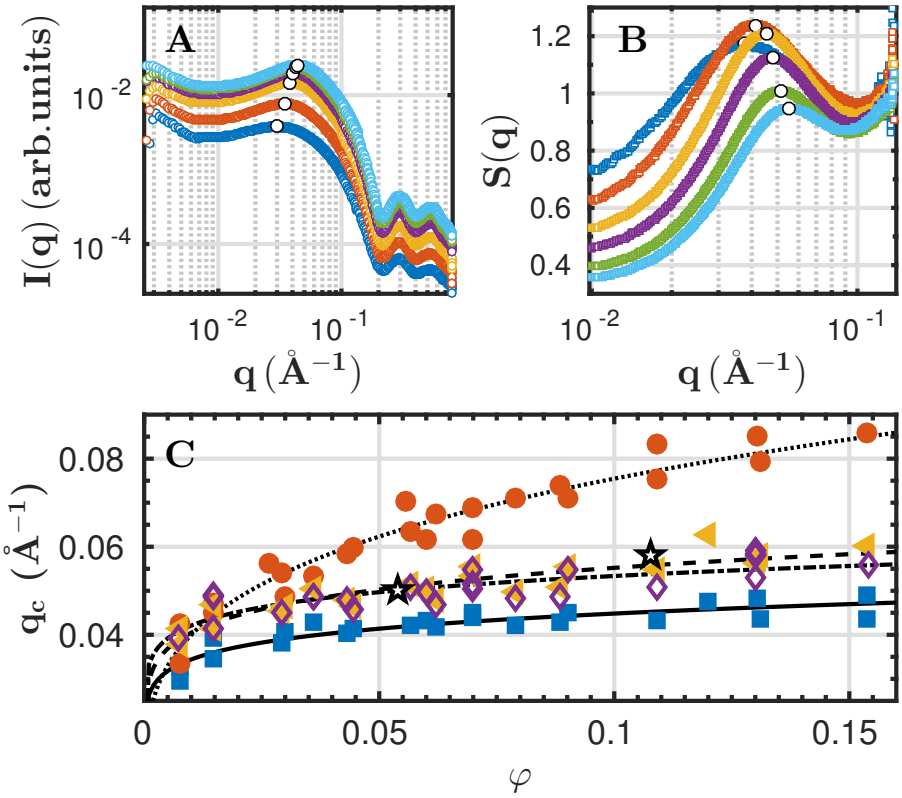

Figure 5.1: *A: Representative SAXS profiles of BLG solutions with protein concentrations of 10, 20, 40, 60, 80 and 100 mg/ml (from bottom to top). B: Experimental structure factors obtained from the SAXS profiles by dividing by the form factor of BLG dimers. The open circles mark the positions of the peak maxima. C: Position q_c of correlation peaks as a function of the protein volume fraction φ from different approaches: maxima of the SAXS intensity according to part A (blue squares); maxima of the experimental structure factor according to part B (yellow triangles); based on a fit using a SC structure factor (orange circles); based on a fit using a 2Y structure factor (purple diamonds). The open star symbols denote q_c obtained from NSE (Fig. 2).*

where m is the protein mass, $M_w = 36.8\,\mathrm{kDa}$ is the molecular weight of the BLG dimer, V_s is the volume of added water and $\theta_p = 0.75\,\mathrm{ml/g}$[153] denotes the specific volume of the protein. From these two number densities, the number of dimers per cluster $N_{dimers} = n_{dimer}/n_{cluster}$ is calculated, yielding an increase from $N_{dimers} \approx 1.6$ at $\phi = 0.054$ to 3.7 at $\phi = 0.18$.

5.2.2 Dynamics - Estimation of cluster size from self-diffusion coefficient

Complementing this structural information on the dimers per cluster, we use neutron spectrocopy, in particular neutron spin-echo (NSE) and neutron backscattering (NBS), to obtain detailed information on cluster formation and structure. While NSE accesses collective motions on length scales of several tenths of nanometers, NBS allows to address the ensemble-averaged self-diffusion coefficients of the proteins on nanometer length scales. The intermediate scattering functions from NSE are well described by a single exponential with relaxation rate $\gamma(q)$ (Fig. 5.2A). The NBS spectra are fitted following the previously published protocol[81;154] for each recorded q-value individually and independently, thus not imposing any q-dependence for the Lorentzian linewidth $\gamma(q)$ during the fitting (Fig. 5.2B).

The scale-dependent diffusion coefficients $D(q) = \gamma/q^2$ for two samples obtained from NSE and NBS are shown in Fig. 5.2C, and support the picture of overall repulsive protein clusters. The collective diffusion function $D(q)$ observed in NSE is given by

$$D(q) = D_0 \frac{H(q)}{S(q)} \tag{5.3}$$

where D_0 denotes the self-diffusion coefficient in the limit of infinite dilution, and $S(q)$ is the static structure factor. The hydrodynamic function $H(q)$ scales in a comparable way to $S(q)$, with generally weaker features. The minimum in $D(q)$ thus corresponds to the peak position q_c of the structure factor, and the obtained values for q_c using a dynamic technique agree well with the values from SAXS (Fig. 5.1C, green stars). As theoretically expected, the collective diffusion coefficient $D(q)$ from NSE converges to the self-diffusion coefficient $D(q)$ from NBS at high q, since collective effects become weak on small length and time scales.

An even more detailed picture of cluster formation is obtained from the self-diffusion coefficients measured by NBS for several protein volume fractions. Consistent with the information from SAXS, the resulting apparent diffusion coefficients D for all samples (symbols in Fig. 5.2D, Table 2 in Supporting Information) are not in agreement with the theoretical diffusion of BLG dimers (dashed line in Fig. 5.2D) at high φ. The theoretical D was calculated following Ref.[155] assuming $R_h = 2.80\,\mathrm{nm}$ for the dimer (HYDROPRO[156], dashed line) and $R_h = 4.44\,\mathrm{nm}$ for a compact cluster of 4 dimers. Given the small length scales, the apparent diffusion coefficients D depend on the translational D_t, and rotational D_r diffusion coefficients via

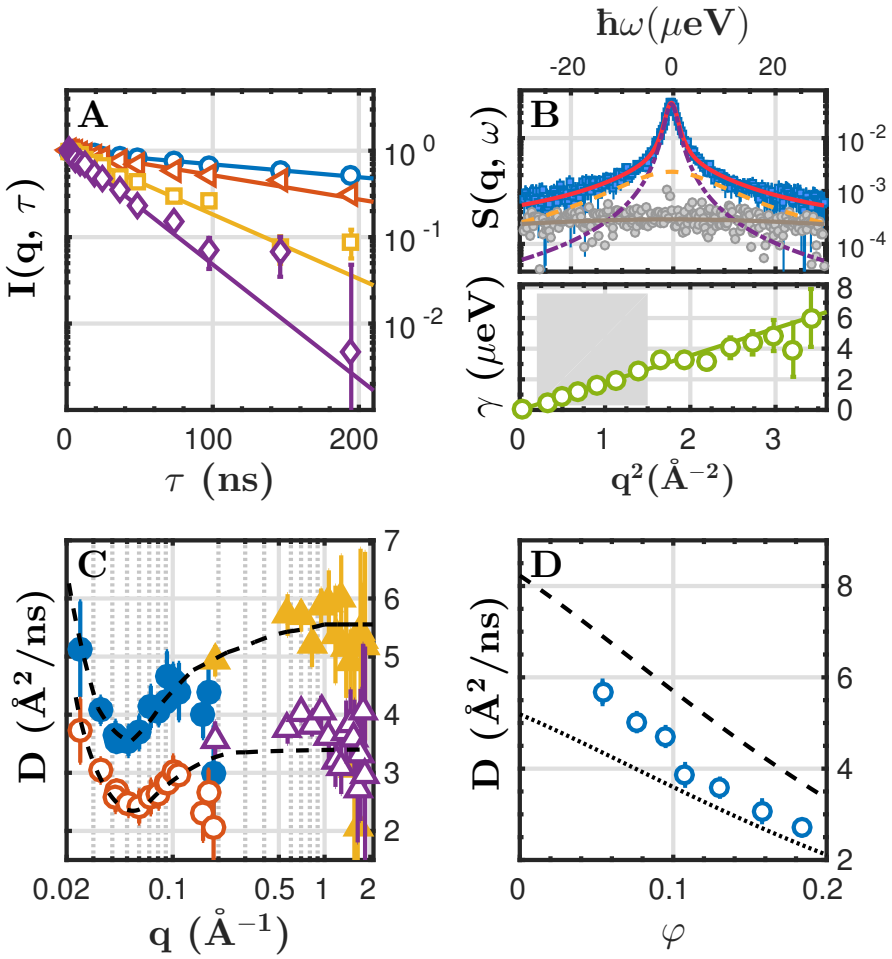

Figure 5.2: *A: Example intermediate scattering functions $I(q,\tau)$ from neutron spin-echo spectroscopy (BLG concentration 161 mg/ml) versus relaxation time τ for q=0.034, 0.051, 0.081, 0.10 Å^{-1} (from top to bottom). B: Example neutron backscattering results for BLG concentration 300 mg/ml. Top: Spectrum at q=0.70 Å^{-1} (blue) along with model fits (lines, see Methods), and corresponding D_2O background (grey). Bottom: Linewidths $\gamma = Dq^2$ from the narrow contribution (dash-dotted) represent simple diffusion of the entire protein molecule (fit region in grey). C: $D(q)$ from neutron spin-echo (circles) and backscattering (triangles) for 76 (open symbols) and 161 mg/ml (filled symbols) BLG solutions. The dashed lines are guides to the eye. D: Apparent diffusion coefficients D from neutron backscattering versus the dry protein volume fraction φ, Eq. 5.4. The dashed and dotted lines are the theoretical D for a BLG dimer and a cluster consisting of 4 dimers, respectively (cf. text).*

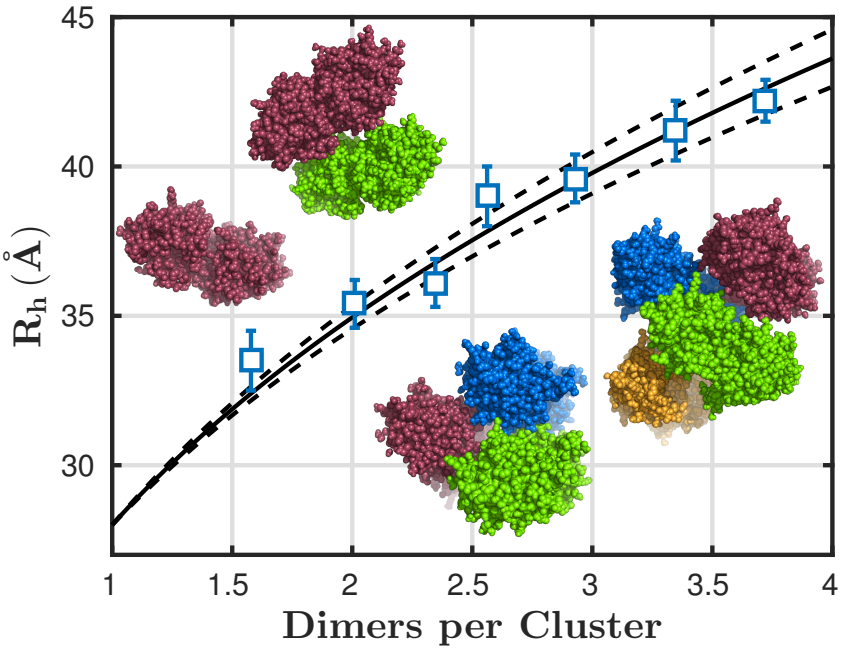

Figure 5.3: *Effective hydrodynamic radii R_h of the clusters obtained from backscattering data versus number of dimers per cluster $N_{dimers} = n_{dimer}/n_{cluster}$ obtained from the SAXS data using equations (5.1,5.2). The solid line is a fit of the data yielding $R_h = 28.0 \cdot N_{dimers}^{0.32\pm0.02}$. The dashed lines indicate the 95 % confidence limits for the fitted exponent. Note that the result for R_h is sensitive to the position of the correlation peak extracted from the SAXS and NSE data. The clusters are illustrated by assembling one to four dimers (1beb.pdb) using PyMOL.*

an implicit function[81;155]. By modelling the clusters as effective hard spheres with volume $\frac{4}{3}\pi R_h^3$, D_t and D_r are only determined by the effective hydrodynamic radius R_h and the known dependencies on the volume fraction (see Methods for details). Fitting the apparent diffusion coefficients D for each protein concentration with the effective hydrodynamic radii $R_h(\phi)$ as only free parameter, we obtain detailed information on the average hydrodynamic size of the clusters (Fig. 5.3, Table 2 in Supporting Information).

Combining the information on the φ-dependent hydrodynamic and static size of the clusters (Fig. 5.3), we obtain the scaling $R_h = R_{h,dimer} \cdot (N_{dimers})^f$ with $f = 0.32 \pm 0.02$. $R_{h,dimer} = 28.0\,\text{Å}^{-1}$ is given by the hydrodynamic radius of the BLG dimer calculated using HYDROPRO[156] and the dimer pdb file *1beb.pdb*. The fitted exponent $f = 0.32 \pm 0.02$ supports a picture of compact assemblies of BLG dimers.

5.3 Coherent picture on cluster formation by combining static and dynamic methods

The combination of results from the SAXS, NBS, and NSE experiments permits to infer on several properties of the protein solutions:

First, the comparison of SAXS and NSE data allows to robustly extract information on the structure factor maximum q_c (Fig. 5.1C). While the dynamic NSE data directly access the structure factor (see Eq. 5.3), different models for the SAXS profiles return different q_c values due to the influence of changing form factor contributions. In particular, both the peak position from the experimental structure factor and the fit using the Two-Yukawa potential agree with the NSE result, whereas the model of a screened Coulomb potential and the intensity maximum of the SAXS curves fail. From this observation we tentatively conclude that our BLG solutions are governed by a superposition of a short-range attraction and long-range repulsion, favoring the formation of clusters. The corresponding scaling $q_c \propto \varphi^b$ with $b \approx 0.12 \ll 1/3$ indicates the presence of protein clusters in our samples.

Second, the high-q limit of the diffusion function $D(q)$ observed in the NSE results is in good agreement with the diffusion coefficients observed using NBS on the same samples. This observation corroborates the general consistency of the NSE and NBS experiments. This agreement also supports the picture that the assumed protein clusters in our samples have a life time that is larger than both the NSE and NBS observation time scales. In the opposing picture of a cluster life time that would cross the NSE or NBS time scales, we would expect inconsistent results from the two techniques.

Third, NBS allows to systematically explore the dependence of the self-diffusion coefficient on the protein concentration in the samples. We observe that the NBS data are not consistent with the presence of dimers over the explored concentration range (Fig. 5.2D). This observation gives rise to the assumption that clusters are present in our samples. Using the presented analysis, we access the concentration-dependence of the cluster hydrodynamic radius R_h in our samples. The increase of R_h with rising protein concentration (Fig. 5.3) can be associated with the presence of clusters with increasing size. We can conclude that these clusters are static on the observation time scale of our NBS experiment: if the clusters were transient, they would diffuse with a smaller effective hydrodynamic radius.

Fourth, by combining the information from NBS with the SAXS results, we can associate R_h with the number of dimers per cluster (Figure 5.3). The obtained scaling $R_h \propto N_{\mathrm{dimers}}^{1/3}$ suggests the formation of compact clusters with a size increasing with protein concentration.

Finally, our results are consistent with the picture that BLG dimers constitute the elementary building blocks of the observed clusters. Notably, these dimers consistently model the SAXS form factor in the Two-Yukawa fits. On a higher level, the

assembly of the dimers within the clusters may be structurally disordered, because no further form factor feature appears to be required in the Two-Yukawa fits.

We note that studies of the dynamic properties of protein clusters and the details of the static structure factor for a system with competing interaction potentials have shown that a reduced power-law behavior $q_c \propto d_{cc}^{-1} \propto \varphi^b$ with $b < 1/3$ alone is not a sufficient condition for the existence of equilibrium, i.e. static, protein clusters. Rather, an intermediate-range order may exist in a system with long range repulsion and short-range attraction, which could obscure an unambiguous discrimination of static or dynamic clusters [35]. However, our additional dynamic experiment confirms the existence of static clusters for our system at least on the NSE time scale on the order of 50 ns.

For BLG, previous studies by Piazza and Iacopini [157] on BLGA suggest that the proteins form oligomer-type clusters. Their results using static and dynamic light scattering indicate that these clusters have a limited life time on the microsecond observation time scale of DLS and should be considered as "transient". These findings are consistent with PFG-NMR results on millisecond time scales by Le Bon et al. [158], which concluded that BLG self-diffusion in concentrated solutions is in agreement with dimers. We remark that these results on these long observation time scale do not contradict our results for BLGA/BLGB mixtures on a much shorter obervation scale.

5.4 Conclusions

In conclusion, we have studied the formation of BLG clusters both using static (SAXS) and neutron spectroscopic (NSE and NBS) methods. By combining the results from these static and dynamic methods, we obtain a conclusive picture of the presence of clusters in BLG solutions that are static on the accessible observation time scale. The SAXS data are consistent with a disordered assembly of BLG dimers that form compact clusters. The experimental SAXS structure factor agrees with a model of short-ranged attractions and long-ranged repulsions consistent with the presence of clusters. The spectroscopic data from both the NBS and NSE experiments, respectively, yield equal diffusion coefficients at the overlapping q within the errors. These diffusion coefficients are in agreement with static BLG clusters on the experimental observation time scale (coherence time) of up to 50 ns in the case of NSE. Moreover, the NSE data are consistent with the SAXS data. The combination of the SAXS and NSE results points to the general possibility to refine the analysis of static SAXS data by employing complementary NSE experiments. Our analysis shows that the combination of the SAXS, NSE and NBS results provides a robust quantitative picture of the cluster size and compactness depending on the protein concentration in the solution, a criterion for the choice of the SAXS model, and information on the cluster lifetime.

5.5 Methods

5.5.1 Sample preparation

β-lactoglobulin (BLG) from bovine milk was purchased from SIGMA-ALDRICH (L3908, guaranteed purity of 90%) and used without further purification. This product is a mixture of the genetic variants A and B that differ at two positions in the primary sequence of 162 amino acids in total[159]. Under physiological conditions, BLG is found predominantly as a dimer[159]. With an isoelectric point (pI) of 5.2, BLG is acidic and carries a net charge of $-10\,\mathrm{e}$ at neutral pH[160].

All samples were prepared by mixing the required amount of protein stock solution with D_2O (for NSE and NBS) or deionized degassed Millipore H_2O (for SAXS). The pH of the protein solutions was monitored using a Seven Easy pH meter from Mettler Toledo. Freshly degassed millipore water has a pH of 7.1, and the resulting BLG solutions display a pH of about 7.2 independent from protein concentration.

The protein volume fraction for a given protein concentration $c_p = m_p/V_s$ is given by[155]

$$\varphi = \frac{c_p}{1 + c_p \cdot \theta_p} \cdot \theta_p. \tag{5.4}$$

5.5.2 Small-Angle X-ray Scattering

SAXS measurements were performed at the European Synchrotron Radiation Facility (ESRF), Grenoble, France at beamline ID02. Protein solutions as well as H_2O were measured using a flow-through capillary cell with a wall thickness of about $10\,\mu$m at a sample-to-detector distance of 2 m. The beam energy was set to 16 keV, and the accessed q values ranged from 0.006 to $0.34\,\text{Å}^{-1}$. For each sample, 10 exposures of 0.1 s or 20 exposures of 0.05 s each were measured on fresh sample solution, respectively. The 2D intensity pattern was corrected and azimuthally averaged to obtain the intensity profiles. Finally, the solvent background was subtracted. More detailed information on data reduction and q-resolution calibration can be found in the literature[129;130].

Additional SAXS data were collected on a laboratory source SAXS instrument – Xeuss 2.0 (Xenocs, Grenoble, France) – employing a GeniX 3D microfocus X-ray tube consisting of a copper anode, using an X-ray wavelength of 1.54 Å. With a sample-to-detector distance of 1.85 m, the employed Pilatus 300K detector covered a q range of 0.0055 to $0.3\,\text{Å}^{-1}$. Protein solutions as well as the buffer (D_2O) were measured in a flow-through quartz capillary with a wall thickness of about $10\,\mu$m. Note that only for the SAXS dataset measured at the laboratory source the protein was dissolved in D_2O.

Experimental structure factors (examples shown in Fig. 5.1B) were calculated from the SAXS intensity by dividing with an ellipsoid form factor with rotation axis $R_a = 38$ Å and axis $R_b = 19$ Å[79]. For structure factor fits, we used the Two-Yukawa

potential and the Hayter-Penfold mean spherical approximation (HPMSA) for the screened Coulomb potential as implemented in IGOR[80]. For the Two-Yukawa potential, an ellipsoid form factor with $R_a = 38\,\text{Å}$ and $R_b = 19\,\text{Å}$ was used. For the screened Coulomb potential, we employed an ellipsoid form factor with $R_b = 19\,\text{Å}$, and R_a was allowed to take values between 39 and 55 Å.

5.5.3 Neutron spectroscopy

The neutron spin-echo measurements were performed at IN15 at Institut Laue-Langevin (ILL), Grenoble, using the wavelengths of 8 and 12 Å and detector angles between 3.5 and 12.5 ° covering a q-range from 0.025 to 0.19 Å^{-1} and Fourier times of up to 190 ns at 12 Å and 58 ns at 8 Å. Details of the experiment setup are explained elsewhere[76;161]. The samples on IN15 were kept in quartz cuvettes at $T = 295\,\text{K}$. For calibration and background treatment, a graphite sample and the pure buffer (D_2O) signal were used.

The neutron backscattering experiment was carried out using the spectrometer IN16B[162] (ILL) employing a Phase Space Transformer[163] and using Si(111) single crystals for the monochromator and analysers in exact backscattering geometry, corresponding to a wavelength of 6.27 Å. The energy was scanned by mechanically Doppler shifting the monochromator crystal on a sinus velocity profile, achieving a maximum energy transfer of approximately $\pm 30\mu$eV. The nearly perfect Gaussian resolution line shape had a width of approximately 0.9 μeV FWHM. The experiment was carried out using the measurement, calibration, and data reduction procedures described earlier[154]. The fit function for the NBS spectra consists of two Lorentzian profiles convoluted with the instrumental resolution (dash-dotted and dashed line in Fig. 5.2B), plus a fixed D_2O background[81;154].

5.5.4 Apparent diffusion coefficient D

Using the NBS results, we obtain the apparent self-diffusion coefficient D from $\gamma(q) = Dq^2$ (cf. Fig. 5.2B). The apparent D, translational D_t, and rotational D_r diffusion coefficients are related via an implicit function[81;155]

$$\sum_{l=0}^{\infty} B_l(q) \frac{D_r l(l+1) + (D_t - D)q^2}{\left[D_r l(l+1) + (D_t + D)q^2\right]^2} = 0\ . \tag{5.5}$$

Using an effective sphere with hydrodynamic radius R_h, the translational and rotational self-diffusion are given by $D_t = f(\tilde{\varphi})k_BT/(6\pi\eta R_h)$ and $D_r = g(\tilde{\varphi})k_BT/(8\pi\eta R_h^3)$, respectively. The dependencies on the concentration, $f(\tilde{\varphi})$ and $g(\tilde{\varphi})$, are the known functions for the translational[164] and rotational[165] self-diffusion of colloidal hard spheres. The effective cluster volume fraction reads $\tilde{\varphi} = n_{cluster}\frac{4}{3}\pi R_h^3$, where we used q_c from the Two-Yukawa fits to calculate $n_{cluster}$

from Eq. (5.1). To calculate $B_l(q)$ analytically, we model the radial distribution function by $\rho_H(r) = \rho_0 \cdot 4\pi \cdot r^2 \cdot \Theta(R_h - r)$, where $\rho_0 = 0.0415\,\text{Å}^{-3}$ is obtained from the actual hydrogen density distribution in the BLG monomer (Supporting Information Figure 2). We obtain (with $x = qR_h$)

$$B_l(q) = (2l+1)\rho_0 2\pi x^3 \left[j_l^2(x) - j_{l+1}(x)j_{l-1}(x)\right] \ . \tag{5.6}$$

We solve Eq. (5.5) with an upper summation limit of $l_{max} = 230$ numerically using the above assumptions, yielding R_h as the sole fit parameter for each protein concentration.

We acknowledge financial support from the Deutsche Forschungsgemeinschaft (DFG) and the Knut and Alice Wallenberg Foundation. We are grateful to B. Farago, P. Falus (ILL), and C. Beck (ILL and Tübingen) for stimulating discussions, and to R. Ammer (ILL) for technical support. Furthermore we thank the ILL and ESRF for allocation of beamtime.

Chapter 6

Results Part C. *Effective Interactions, Collective Diffusion and Cluster Formation in Protein Solutions in the Presence of Trivalent Salts*

In preparation.

Michal K. Braun, Ralf Schweins, Tilo Seydel, Michael Sztucki, Fajun Zhang and Frank Schreiber

Contributions	
Research design	*FZ, TS, FS*
Experiments	*MB, FZ*
Technical Assistance	*RS, MS*
Data analysis and interpretation	*MB, FZ, TS*
Paper writing	*MB, FZ, FS*

6.1 Introduction

The collective diffusion in solutions of BSA with YCl_3 was investigated previously by D. Soraruf et al. In this study, solutions were only prepared in regime I below the first salt concentration boundary c^*. The intermediate scattering function was modeled by a sum of two exponential terms. The fast mode was tentatively assigned to monomers and the second mode to clusters. The diffusion coefficients both of the monomers and the clusters decreased with increasing salt concentration. The weight of the cluster mode increased strongly shortly before c^* was reached. The collective diffusion coefficients were normalized and plotted together with the normalized inverse SLS intensity. At low salt concentrations the monomer collective

diffusion followed the inverse SLS intensity. At higher salt concentration the cluster collective diffusion followed the inverse SLS intensity. The SLS data further pointed to c^* being a spinodal line[3]. In a complementary study Grimaldo et al. measured the self diffusion coefficients in solutions of BSA with YCl_3 below c^*. Using Flory-Stockmeyer theory for the number density of clusters with n monomers, the binding probability was calculated. Both the binding probabilty and the self diffusion coefficients followed a master curve when plotted against the ratio of salt and protein, c_s/c_p[5].

Here, the dynamic light scattering study in BSA with YCl_3 is extended to BSA with $LaCl_3$. Furthermore, solutions are also prepared in regimes II and III. The results are compared to the data obtained previously. The data in the system with BSA and $LaCl_3$ follow the same trends as in the system with BSA and YCl_3. In the second regime the solutions are turbid. Although this turbidity is not strong in the case of $LaCl_3$, it may cause multiple scattering and make the DLS data hard to analyze. In order to quantify the strength of the turbidity, transmission measurements were preformed.

6.2 Experimental

6.2.1 Materials and sample preparation

BSA (A7906) and LaCl3 (298182) were purchased from Sigma Aldrich and used as received. The protein as well as the salt were dissolved in deionized and degassed Millipore water (conductivity 18.2 MΩcm). Protein and salt stock solutions as well as the water were filtered using 200 nm Nylon filters. Samples were prepared from the filtered stock solutions directly before the light scattering measurements.

6.2.2 Transmission measurements

The transmission of the (BSA-$LaCl_3$) samples was measured using a *Cary 50* UV-vis spectrophotometer (Varian, Inc). The samples were measured right after preparation. The measurements were repeated several times in order to investigate the time dependence of the transmission.

6.2.3 Static and Dynamic Light Scattering

Static and dynamic light scattering was performed using the *ALV/CGS-3* goniometer and a *ALV/LSE-5004* digital correlator (ALV-GmbH, Langen, Germany). The system was controlled using the ALV-Correlator Software V. 3.0. The HeNe-Laser of the instrument operates at a wavelength of $\lambda = 632.8$ nm. After passing through an attenuator the light intensity is measured on the monitor diode. Then the light beam hits the sample. To keep reflections of the light negligible, the sample is

surrounded by an index matching vat. This quartz glass vat is filled with toluene. Toluene has an index of refraction of 1.496 [166] which is close to the index of refraction of quartz glass. The temperature of the toluene bath is controlled using a water bath (*Haake A10* bath together with a *Haake AC 200* thermostat, Thermo Fisher Scientific Inc.). The scattered intensity is measured by a detector which is mounted on a goniometer. Angles 2θ in the range of 12° to 152° can be measured with an angular resolution of 0.025°. The refractive index of water is $n_0 = 1.332$. According to

$$q = \frac{4\pi n_0}{\lambda} \sin(\theta), \tag{6.1}$$

the investigated angular range corresponds to a q-range of $2.6{\cdot}10^{-3}$ Å^{-1} to $2.8{\cdot}10^{-4}$ Å^{-1} [49;167].

For the analyzed samples with BSA concentrations from 5 to 25 mg/ml, two well-separated decay times are observed. A double exponential fit with two distinct diffusion coefficients D_1 and D_2 is therefore used to model the correlation function,

$$g_2(q,\tau) = A_1 \cdot \exp(-D_1 q^2 \tau) + A_2 \cdot \exp(-D_2 q^2 \tau). \tag{6.2}$$

As in the work by D. Soraruf et al. [3], the fast (D_1) and slow (D_2) components of collective diffusion are tentatively assigned to the diffusion of monomers and of clusters. All fits were carried out using MATLAB code that was developped by D. Soraruf and F. Zanini.

6.2.4 Small Angle X-ray Scattering

The effective protein-protein interactions in the solutions were characterized by SAXS. SAXS experiments were performed at beamline ID02 at the ESRF, Grenoble, France. The X-ray energy was 12 keV. For all measurements the sample-to-detector distance was set to 2 m, covering a q-range of 0.005 to 0.5 Å^{-1}. The data were collected by a high-sensitive fiber-optics coupled CCD detector placed in an evacuated flight tube. Samples were prepared right before the measurement. The protein solution was loaded into a flow-through quartz capillary with a diameter of 2 mm and a wall thickness of 0.01 mm. The data sets were reduced by subtracting the scattering of a pure salt solution as a background and by normalizing to absolute intensity. Further details on q-resolution, calibration and data reduction can be found in Refs. [129;130].

To quantitatively describe the attractive potential, the sticky hard sphere (SHS) potential was used [56]. A perturbative solution of the Percus-Yevick closure relation was used to calculate the structure factor [57]. The sticky hard-sphere model was introduced by Baxter [56] for a system with hard-core repulsion and additional short-range attraction, which can undergo fluid-vapor phase separation. The interaction

potential for particles with radius R is

$$\beta U(r) = \begin{cases} \infty & r < \sigma = 2R \\ -\beta u_0 = \ln\left(\frac{12\tau\Delta}{\sigma+\Delta}\right) & \sigma < r < \sigma + \Delta \\ 0 & r > \sigma + \Delta. \end{cases} \tag{6.3}$$

The interaction potential is in units of k_BT ($\beta = 1/k_BT$), τ is the stickiness parameter and Δ is the width of the square well.

Frequently, for simplicity the limit $\Delta \to 0$ is considered. In this limit the reduced second virial coefficient is given by

$$\lim_{\Delta\to 0} \frac{B_2}{B_2^{HS}} = 1 - \frac{1}{4\tau}. \tag{6.4}$$

$B_2^{HS} = 16\pi R^3/3$ is the second virial coefficient of a hard sphere of radius R. For the SAXS data fitting, Δ was fixed to $0.01\,\sigma$ to avoid artificial coupling with τ. Data fitting was performed using IGOR Pro with macros provided by NIST [80].

Further SAXS data was measured using the home SAXS instrument *Xeuss 2.0* from XENOCS.

6.3 Results and Discussion

6.3.1 Comparison of the phase behavior of protein solutions with YCl_3 and $LaCl_3$

Fig. 6.1 shows the phase diagrams of BSA with YCl_3 and BSA with $LaCl_3$ in H_2O. The green and orange shaded regions between the c* and c** lines mark the second regimes in the $LaCl_3$ and YCl_3 systems. The dashed ellipse marks the LLPS region in BSA with YCl_3. At room temperature there is no LLPS for protein solutions with $LaCl_3$. Regime II is narrower with $LaCl_3$ than with YCl_3. This is mainly due to the reduced c**. c* is very close for both salts. Light scattering measurements, indicated by the red arrow, were performed at low protein concentrations from 5 to 25 mg/ml. The salt concentration was varied through all three regimes. SAXS measurements, indicated by the blue arrow, were performed at a protein concentration of 84 mg/ml. The salt concentration was also varied to cover all three regimes.

6.3.2 Effective interactions characterized by SAXS

The differences in the phase diagrams are due to the effective protein-protein interactions in solution. SAXS helps to microscopically characterize the effective interactions. Here, we focus on the interactions in regimes II and III, where the

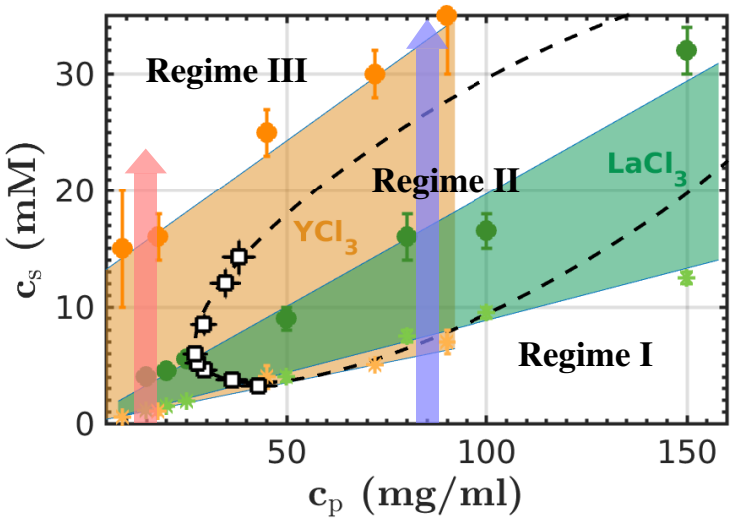

Figure 6.1: *Phase diagram of BSA with $LaCl_3$ and BSA with YCl_3 at room temperature. In both cases a reentrant condensation phase behavior is observed. The second regime with $LaCl_3$ is narrower than with YCl_3. The dashed ellipse marks the LLPS region in the BSA-YCl_3 system. No LLPS is observed in BSA-$LaCl_3$ at room temperature. The red and blue arrow illustrate the variation of salt for DLS and SAXS measurements, respectively. The data for the BSA-YCl_3 phase diagram were taken by M. Wolf.*

effective interactions are *attractive*. In regime I Coulomb repulsion dominates. The interactions in this regime have been discussed in a previous study [168].

Fig. 6.2 shows the measured intensity for 84 mg/ml BSA with $LaCl_3$ (left part), and YCl_3 (right part). The $LaCl_3$ and YCl_3 concentrations are given in the legends. With increasing salt concentration the low q intensity first increases (top row). After having reached a maximum it slowly decreases again (bottom row). At low salt concentrations, in regime I, i.e. from 0-4 mM salt there is no difference between the scattering curves obtained from the $LaCl_3$ and the YCl_3 samples. As mentioned above, this is the regime where the effective interactions are repulsive. In the second regime, starting from roughly 6 mM the intensity at low q is a bit higher in the YCl_3-system. This means that at similar salt concentrations the attraction is stronger with YCl_3 than with $LaCl_3$. In regime III the intensity at low q decreases again. This decrease happens more slowly in the case of YCl_3. The YCl_3-system thus remains attractive over a broader salt concentration range.

To quantify the effective interaction, SAXS data were fitted using an ellipsoid form factor combined with a sticky-hard sphere model as described in the experimental section. The advantage of the SHS model is that B_2/B_2^{HS} can be calculated from SHS fits. The calculated B_2/B_2^{HS} values are shown in Fig. 6.3 (top) together with the inverse of the intensity at low q (bottom). These curves also first decrease

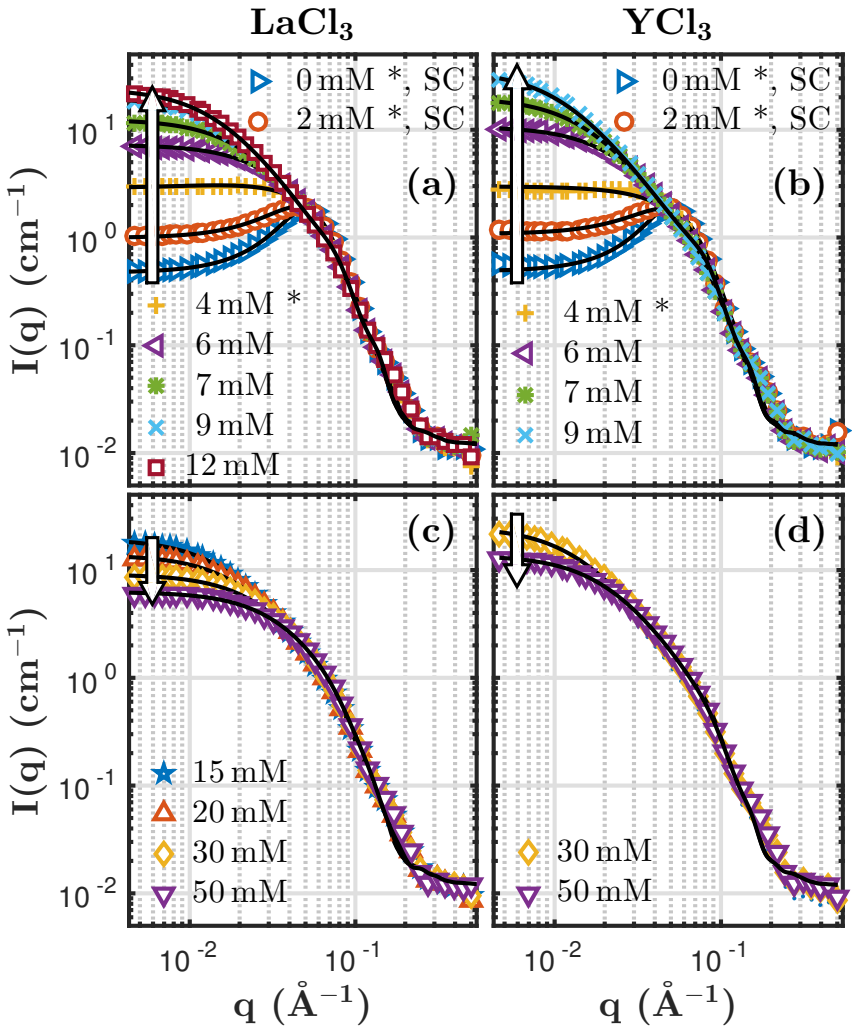

Figure 6.2: *Left: SAXS data and fits for 84 mg/ml BSA with $LaCl_3$ in H_2O. Right: SAXS data and fits for 84 mg/ml BSA with YCl_3 in H_2O. Top: Increasing intensity at low q. Bottom: Decreasing intensity at low q. Where the SC potential was used, this is indicated in the legend. The other data was fitted using the SHS potential. A * in the legend marks the data where a smaller form factor ($r_b = 42\,\text{Å}$) was used. The rotation axis of the ellipsoid was always set to $r_a = 18\,\text{Å}$. At higher salt concentrations r_b was set to 61 Å.*

sharply and then above c* increase slowly again. In the case of BSA-$LaCl_3$ two series of samples for both 84 and 150 mg/ml were prepared. The two curves fall together when plotted against c_s/c_p, showing that with B_2/B_2^{HS} the characteristic features of each protein-salt system may be identified. The overall attraction in BSA-YCl_3 is stronger and decreases more slowly upon the addition of more salt. The error in B_2/B_2^{HS} was propagated from the error in τ given by the sticky hard sphere (SHS) potential fit. The errors are smaller than the symbols, however, they are probably underestimated.

The absolute scattering at low q, $I(q \to 0)$, adds to this consistent physical picture in a model-free way. The lower part of Fig. 6.3 shows the inverse of the SAXS intensity at low q. The mean value of the first three intensity data points was taken and divided by the protein concentration. The inverse of this value is plotted against the ratio of c_s and c_p. The error $dI(q)$ in the intensity was calculated as $dI(q) = \sqrt{I(q)}/a$. The factor a was chosen such that the form factor features at high q were not covered by the error. For the error in the inverse intensity, the mean of this error for the first three data points was propagated. Theoretically, $I(0)$ is determined by the compressibility χ_T, since $S(q \to 0) = k_B T \rho\ \chi_T$ [169]. The compressibility χ_T diverges at the spinodal line. Thus, the closer the coexisting densities are, the closer binodal and spinodal lines are, the larger is χ_T and the smaller is $1/I(q \to 0)$. The experimental results on the microscopic interactions reflect the phase behavior, as can be seen by comparing the SAXS intensity for small values of q (Figure 6.3) with the RC and LLPS phase behavior shown in Figure 6.1. For samples with $LaCl_3$, without LLPS binodal, $1/I(0)$ decreases and increases and follows similar trends to B_2/B_2^{HS}. For samples with YCl_3, the existence of the LLPS binodal changes the behavior of $1/I(0)$. $1/I(0)$ decreases first. When c_s reaches c*, the system phase-separates (LLPS) in the range of c_s/c_p from 7.9 to 16. For $c_s/c_p = 7.1$ and 16 the system is close to the critical points of LLPS, which results in large values of χ_T and $S(q \to 0)$ and in small values of $1/I(q \to 0)$. Within the LLPS region $1/I(q \to 0)$ increases first and then decreases again when the second critical point is reached (filled purple circles). Above the LLPS, in regime III, $1/I(q \to 0)$ again follows a trend similar to B_2/B_2^{HS}.

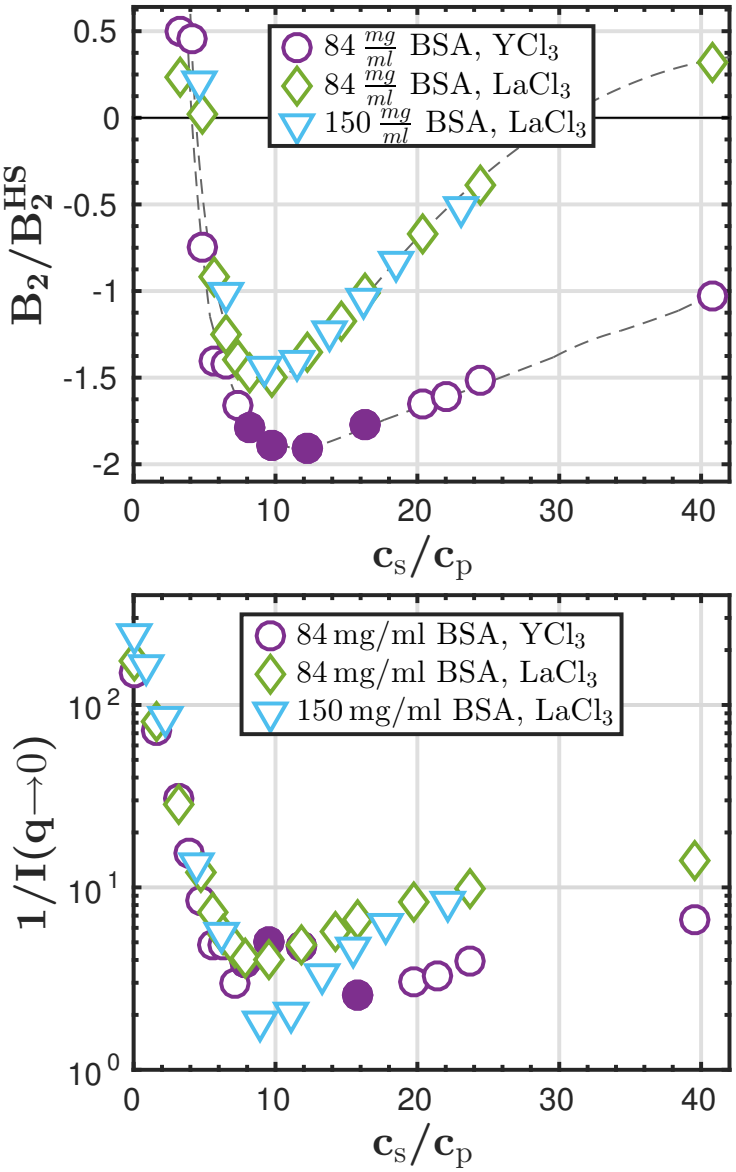

Figure 6.3: *Upper part: reduced 2^{nd} virial coefficients calculated from the SHS fits for the BSA-$LaCl_3$ and BSA-YCl_3 systems in H_2O. The dashed lines are guides to the eye. Lower part: the inverse of the intensity at low q shows the same trend as the B_2/B_2^{HS} values do in a model-free way. The filled symbols mark samples that showed LLPS.*

6.3.3 Collective diffusion and cluster formation

Before the DLS data is presented, the UV-vis-transmission measurements are discussed. These results are important for the proper analysis and interpretation of the DLS data. The protein solutions with $LaCl_3$ are only slightly turbid in regime II. Solutions with YCl_3 at this concentration are slightly more turbid with lower transmission as shown in Fig. 12.1 in the Supporting Material. In the BSA-$LaCl_3$ system visual inspection of the samples shows only a slight turbidity in regime II at all protein concentrations up to 150 mg/ml at room temperature. Although no macroscopic phase separation is observable for the samples with $LaCl_3$, the UV-vis transmission values in the condensed regime are still significantly low (below 50%). Therefore, multiple scattering may affect the DLS data in this region. The data taken in regime II has to be treated with due care.

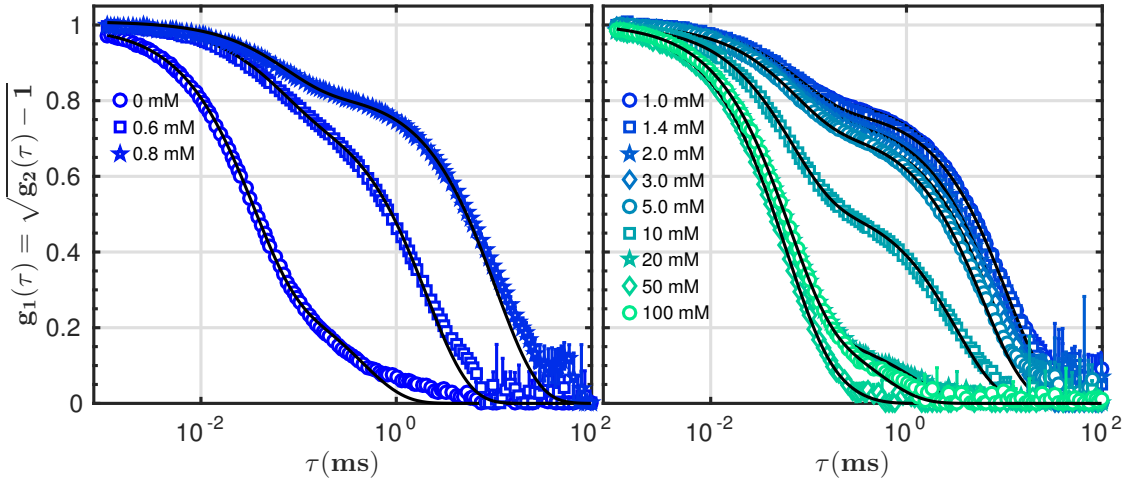

Figure 6.4: *Intermediate scattering function $g_1(\tau)$ at 90° for 10 mg/ml BSA with different concentrations of $LaCl_3$. Left part: the contribution of clusters increases and the decay rates Γ_1 and Γ_2 decrease with increasing salt concentration. Right part: starting from $\sim$ c* the contribution of clusters decreases and the decay rates Γ_1 and Γ_2 increase with increasing salt concentration.*

A set of representative DLS profiles is shown in Fig. 6.4. The dynamic data (intermediate scattering function (ISF) $g_1(\tau)$) is shown at 90° for 10 mg/ml BSA with different concentrations of $LaCl_3$ crossing all three regimes. The solid black lines are the fitted double-exponential decays. The c* and c** values for BSA-$LaCl_3$ are shown in Table 12.1 in the Appendix. At 15 mg/ml BSA c* is 1.1 ± 0.1. At 10 mg/ml c* can thus be assumed to also be around 1 mM. Without added salt, the ISF is a nearly single-exponential function. With increasing c_s, a second exponent appears and becomes more and more dominant up to $c_s \approx$ c*. Starting from $\sim$ c* the contribution of the clusters slowly decreases again. After c**, the contribution

of the second exponent (slow mode) still exists until $c_s \gg c^{**}$ where it disappears. As already mentioned above, this observation indicates the dominance of two types of species in the system. While the fast mode is assigned to the protein monomer, the slow mode is assigned to clusters.

Fig. 6.5 presents the collective diffusion coefficients for both monomers (fast mode, D_1) and clusters (slow mode, D_2) as a function of c_s/c_p for both systems at room temperature. The open symbols are for BSA-YCl_3. The filled symbols are for BSA-$LaCl_3$. The BSA-YCl_3 data in the left part of the figure up to c^* was taken by D. Soraruf[3]. The green area marks the second regime in BSA-$LaCl_3$ at protein concentrations up to 25 mg/ml (see also Table 12.1). It starts at the lowest c^*/c_p value in this protein concentration range and ends at the highest c^{**}/c_p value. The error in c^* or c^{**} is subtracted or added, respectively. The left part shows the data up to the first critical boundary c^* on a linear c_s/c_p-scale. The top row in Fig. 6.5 shows the fast collective diffusion coefficient (monomers) D_1. The middle row shows the slow component (clusters) D_2. The bottom row shows the contribution A_2 of the slow component.

In regime I the collective diffusion in the BSA-$LaCl_3$ system is similar to the collective diffusion in the BSA-YCl_3 system. The collective diffusion of monomers decreases steadily. This decrease reflects the enhanced attractive interactions between the protein molecules. The collective diffusion of the clusters first stays constant. Shortly before c^* it decreases dramatically and the contribution of the clusters to the scattering signal, A_2, at the same time increases. This means that protein clusters that are not visible by eye start to form shortly before c^* where the aggregation becomes visible by eye. As light scattering is very sensitive to large clusters which have a much larger scattering power, the point where A_2 shows a sudden increase should correspond to the lower limit of the formation of large clusters.

Interestingly, D_1 decreases faster and D_2 starts to decrease earlier in BSA with $LaCl_3$ than in BSA with YCl_3. The reason for this is not yet clear. The measurements in the second regime for BSA-$LaCl_3$ (data not completely shown) show that the decrease does not continue but the collective diffusion both of the monomers and the clusters stays constant in the second regime. Here, it has to be kept in mind, that multiple scattering probably influences the result. However, this finding could point to c^* being no spinodal line. Above c^{**}, up to $c_s/c_p = 50$ or 100 ($LaCl_3$ or YCl_3), D_2 is still dominates the DLS signal. In the third regime both D_1 and D_2 slowly increase again. Thus the attractions become weaker again and the clusters dissolve. In BSA with $LaCl_3$ the contribution A_2 of the clusters starts to decreases at a c_s/c_p where in BSA with YCl_3 there is no decrease yet. This finding corresponds to the narrower regime II in BSA with $LaCl_3$.

The overall behavior of the collective diffusion coefficients follows a trend that is similar to the trend of the effective interactions characterized by B_2/B_2^{HS} and the inverse of the SAXS intensity at low q (Fig. 6.3).

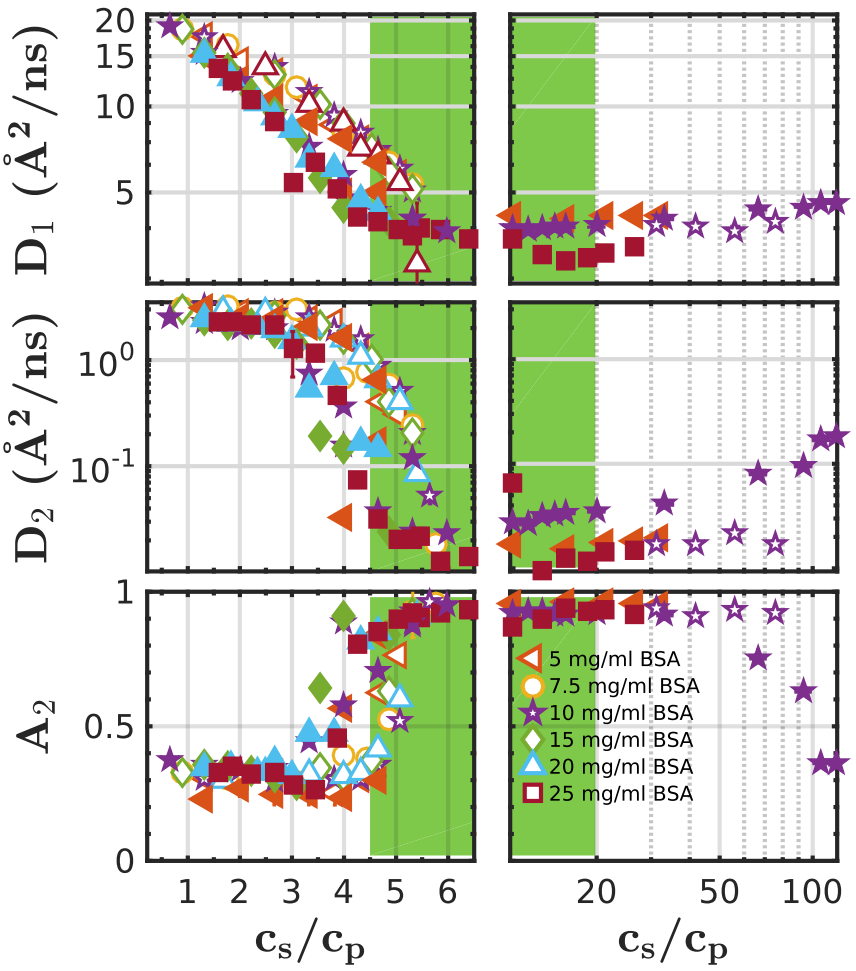

Figure 6.5: *Collective diffusion coefficients from DLS for BSA-YCl_3 (open symbols) and BSA-$LaCl_3$ (filled symbols) at room temperature. The left part shows the data up to the first critical boundary, c^* on a linear c_s/c_p-scale. The YCl_3 data up to c^* was taken by D. Soraruf[3]. The right part shows the data starting from $\sim c^{**}$ on a logarithmic c_s/c_p-scale. The green area marks regime II for BSA-$LaCl_3$ at low protein concentrations up to 25 mg/ml (see also text and Table 12.1). The intermediate scattering function was fitted with a two-exponential decay function (see Fig. 6.4).*

6.4 Conclusions

The collective diffusion data reflects the effective interactions which are quantified by B_2/B_2^{HS}. In BSA with $LaCl_3$ the same trends are obtained as in BSA with YCl_3. The narrower regime II in BSA with $LaCl_3$ makes the collective diffusion coefficients increase earlier than in BSA with YCl_3. Due to the low transmission in regime II, the DLS measurements in this regime have to be interpreted with due care. Assuming that multiple scattering effects are neglible, one can conclude that c^* is not a spinodal line because D_1 does not decrease to zero but instead levels off at a nonzero value above c^*.

We gratefully acknowledge financial support from Deutsche Forschungsgemeinschaft (DFG) and thank the European Synchrotron Radiation Facility (ESRF) for the allocation of beamtime on beamline ID02. We thank Pinelopi Christodoulou for performing the UV-vis transmission measurements.

Chapter 7

Results Part D. *Reentrant Phase Behavior in Protein Solutions Induced by Multivalent Salts: Effect of Anions Cl^- versus NO_3^-*

In preparation.

Michal K. Braun, Andrea Sauter, Michael Sztucki, Fajun Zhang and Frank Schreiber

Contributions	
Research design	*FZ, FS*
Experiments	*MB, AS, FZ*
Technical Assistance	*MS*
Data analysis and interpretation	*MB, AS, FZ*
Paper writing	*MB, FZ, FS*

7.1 Introduction

The study of effective protein-protein interactions is important for protein aggregation, protein cluster formation and protein crystallization[82]. Diseases such as eye cataract, sickle cell anemia and Alzheimer's disease are due to protein phase separation and protein aggregation. Protein crystals are needed to resolve the structure and hence the function of proteins by X-ray crystallography. The interaction between proteins and anions is discussed since the seminal work by F. Hofmeister. In the Hofmeister series the anions are ordered according to their ability to stabilize proteins in solution[170]. Macroscopically it is observed in diverse systems that the anions follow the Hofmeister series. The microscopic reasons are however not well

understood. One out of many studies investigates the binding of the different anions to a pocket in a protein. There it was found that the entropic cost for binding increases along the Hofmeister series. This increase in the entropic cost is however compensated for by the enthalpic gain of binding. The resulting free energy of binding decreases slightly but steadily along the Hofmeister series[171]. In our group we study the model system of BSA in solution with a trivalent salt. The effective interactions in this systems can be tuned by many parameters such as temperature, nature of the solvent isotope, nature of the cation etc[45;168]. In this work the effect of the anion is investigated. Two anions, NO_3^- and Cl^- are examined. These two anions are close to each other in the Hofmeister series. Nevertheless a strong difference in the strength of the effective attraction is observed.

7.2 Experimental

7.2.1 Materials

BSA (Product No. A7906), $LaCl_3$ (Product No. 298182) and $La(NO_3)_3$ (Product No. 203548) were purchased from Sigma Aldrich and used as received. The protein as well as the salt were dissolved in deionized and degassed Millipore water (conductivity 18.2 MΩcm).

7.2.2 Methods

UV-visible spectroscopy

Concentrations of protein stock solutions were determined by measuring the absorbance at 280 nm using a *Cary 50* UV-Vis spectrophotometer from Varian Inc with the software *Cary WinUV*. The extinction coefficient of BSA is ϵ_{BSA}=0.667 ml/(mg·cm)[66].

FTIR and CD spectroscopy

Fourier transform infrared spectroscopy (FTIR) and circular dichroism spectroscopy (CD) were used to monitor the stability of the secondary protein structure in the presence of trivalent salts. An *IFS 48* instrument and a *Vertex 70* instrument, both from Bruker were used for the FTIR measurements. The CD measurements were performed using a *J-720* spectrophotometer from Jasco Inc. For the FTIR measurements, the samples were dissolved in D_2O with a protein concentration of about 20 mg/ml. The samples for the CD measurements were prepared in H_2O with a protein concentration range from 0.2 to 1 mg/ml.

Small Angle X-Ray Scattering (SAXS)

The effective protein-protein interactions in the solutions were characterized by SAXS. SAXS experiments were performed at beamline ID02 at the ESRF, Grenoble, France. The X-ray energy was 12 keV. For all measurements the sample-to-detector distance was set to 2 m, covering a q-range of 0.005 to 0.5 Å^{-1}. The data were collected by a high-sensitive fiber-optics coupled CCD detector placed in an evacuated flight tube. Samples were prepared right before the measurement. The protein solution was loaded into a flow-through quartz capillary with a diameter of 2 mm and a wall thickness of 0.01 mm. The data sets were reduced by subtracting the scattering of a pure salt solution as a background and by normalizing to absolute intensity. Further details on q-resolution, calibration and data reduction can be found in Refs.[129;130]. Additional SAXS data were collected on the laboratory source SAXS instrument – *Xeuss 2.0* (Xenocs, Grenoble, France) – employing a *GeniX 3D* microfocus X-ray tube consisting of a copper anode, using an X-ray wavelength of 1.54 Å. With a sample-to-detector distance of 1.85 m, the employed *Pilatus 300K* detector covered a q range of 0.0055 to 0.3 Å^{-1}. Protein solutions as well as the salt solutions were measured in a flow-through quartz capillary with a wall thickness of about 10 μm.

To quantitatively describe the attractive potential, the SHS potential was used[56]. A perturbative solution of the Percus-Yevick closure relation was used to calculate the structure factor[57]. The sticky hard-sphere model was introduced by Baxter[56] for a system with hard-core repulsion and additional short-range attraction, which can undergo fluid-vapor phase separation. The interaction potential for particles with radius R is

$$\beta U(r) = \begin{cases} 1 & r < \sigma = 2R \\ -\beta u_0 = \ln\left(\frac{12\tau\Delta}{\sigma+\Delta}\right) & \sigma < r < \sigma + \Delta \\ 0 & r > \sigma + \Delta. \end{cases} \tag{7.1}$$

The interaction potential is in units of k_BT ($\beta = 1/k_BT$), τ is the stickiness parameter and Δ is the width of the square well.

Frequently, for simplicity the limit $\Delta \to 0$ is considered. In this limit the reduced second virial coefficient is given by

$$\lim_{\Delta\to 0} \frac{B_2}{B_2^{HS}} = 1 - \frac{1}{4\tau}. \tag{7.2}$$

$B_2^{HS} = 16\pi R^3/3$ is the second virial coefficient of a hard sphere of radius R. For the SAXS data fitting, Δ was fixed to $0.01\,\sigma$ to avoid artificial coupling with τ. Data fitting was performed using *IGOR Pro* with macros provided by NIST[80].

7.3 Results and Discussion

7.3.1 Phase behavior of BSA with YCl_3, $Y(NO_3)_3$, $LaCl_3$, $La(NO_3)_3$

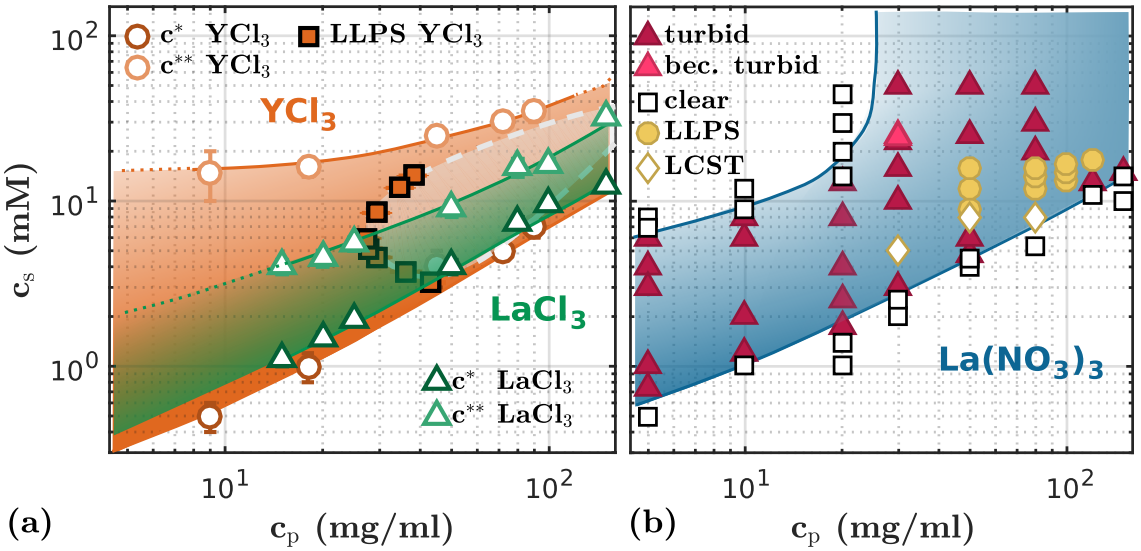

Figure 7.1: *Experimental phase and state diagrams of BSA with a) YCl_3, $LaCl_3$ and b) $La(NO_3)_3$. The data for the BSA-YCl_3 phase diagram was taken by M. Wolf.*

Fig. 7.1 presents the experimental phase diagram of BSA with three salts at room temperature. Fig. 7.1a shows the experimental phase diagram of the two chloride salts YCl_3 and $LaCl_3$. The lower boundary c* of the second regime is located at comparable salt concentrations and does not change much in $LaCl_3$ versus YCl_3. This indicates a purely electrostatic effect. The upper boundary c**, however, is located at much higher salt concentrations in YCl_3. Furthermore, YCl_3 samples are more turbid in regime II and in a certain part of regime II LLPS is found. The orange squares mark the salt concentration (c_s) and protein concentration (c_p) concentrations in the dilute phase of phase separated samples. The concentrations in the dense phase are not shown. They are outside the plotted range. $LaCl_3$ samples turn only slightly turbid and do not undergo LLPS at room temperature. At higher temperature, the $LaCl_3$ samples also show LLPS. With both salts the systems exhibit a lower critical solution temperature (LCST) phase behavior. These results for the two different cations are consistent with previous findings [168]. Further below, detailed SAXS characterization will be shown which indicates that YCl_3 induces stronger attraction than $LaCl_3$. Fig. 7.1b shows the state diagram of BSA in solution with $La(NO_3)_3$. In difference to Fig. 7.1a, the state of each sample is plotted individually. The c* and c**-boundaries lie between the last clear and the first turbid sample and between the last turbid and the first clear sample. The yellow

circles mark the samples which showed LCST LLPS. These samples became turbid when they were warmed by hand and they had a dense liquid phase on the bottom. The open diamonds show samples that showed LCST but had no discrenible dense liquid phase. Compared to $LaCl_3$ the position of the c^* boundary changes hardly. However, the second regime is significantly broadened with $La(NO_3)_3$ due to a strong shift of c^{**} to higher salt concentrations. Starting from 30 mg/ml c^{**} vanishes and the solutions do not reclarify. Above 50 mM the samples showed massive whitish precipitation. These samples are not shown, since, in this case, the precipitation is not due to charge inversion but to a different mechanism. At a BSA concentration of 30 mg/ml there were two samples which did not become turbid at once but after about 10 min. These samples are marked with a lighter purple and classified as "bec. turbid". Comparison of the BSA-$La(NO_3)_3$ state diagram and the BSA-YCl_3 phase diagram shows the following. At the concentrations where c^{**} exists in solutions with $La(NO_3)_3$, it is located below c^{**} at the same protein concentrations in YCl_3. This would mean that starting from $LaCl_3$, replacing the anion by NO_3^- enhances the attraction less than replacing the cation by Y^{3+}. However, in contradiction to this, with Y^{3+} the RC does not vanish at higher c_p. For samples with $Y(NO_3)_3$ a behavior that is similar to the one with $La(NO_3)_3$ was observed. In this case RC could not be observed at all (data not shown).

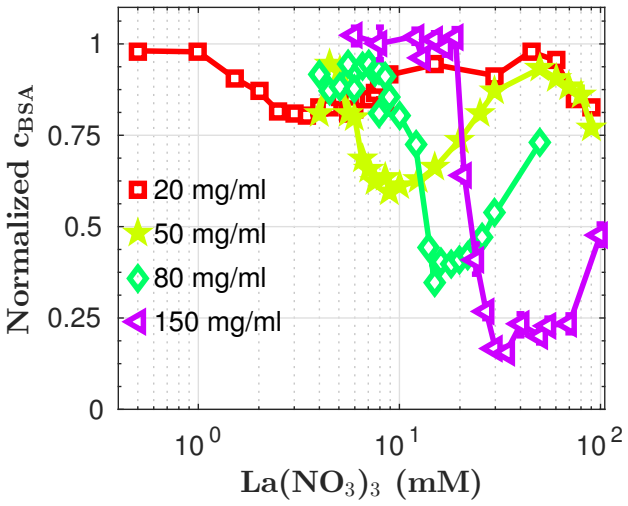

Figure 7.2: *Protein concentration in the supernatants after centrifugation determined by UV-vis spectroscopy. With increasing BSA concentration the minimum shifts to higher $La(NO_3)_3$ concentrations.*

Fig.7.2 shows the normalized protein concentration for BSA-$La(NO_3)_3$. Samples were prepared with the protein concentrations listed in the legend and different $La(NO_3)_3$ concentrations. After centrifugation of the samples, the protein concentration in the supernatant was measured by UV-vis spectroscopy. At all measured BSA concentrations, the normalized c_p shows a minimum. This minimum is located

at higher salt concentrations with increasing c_p. An increase in the supernatant concentration is observed for all measured BSA concentrations. This leads to the assumption that with $La(NO_3)_3$ the attraction is only slightly too strong to observe complete RC by visual inspection. As already mentioned, in BSA with $Y(NO_3)_3$ no RC is observed at all. The stronger cation *and* anion lead to an effective attraction that is too strong . Further, the strong attraction leads to amorphous aggregation instead of LLPS at room temperature. Overall, the trend of the salt effect on RC is $LaCl_3$ <YCl_3 <$La(NO_3)_3$ <$Y(NO_3)_3$. These phase behaviours are summarized in Table 7.1. Comparing the different phase behaviors indicates that NO_3^- enhances the effective attraction, which broadens regime II and leads to the absence of RC at high c_p. This finding is especially interesting with regard to the Hofmeister series. For literature on the Hofmeister series see e.g. the publications by Y. Zhang and P. Cremer[170;172]. The two anions Cl^- and NO_3^- are close in the Hofmeister series. Furthermore, F. Hofmeister worked with molar salt concentration whereas here in this work millimolar salt concentrations are used. Nevertheless in the systems of BSA in solution with a trivalent salt a strong effect on the effective interactions is observed. This effect can thus be regarded as an "enhanced" Hofmeister effect.

Table 7.1: *Phase behavior overview of BSA with different salts at room temperature.* $\oplus$ *indicates that the phase behavior is limited under the current experimental conditions.*

	YCl_3	$Y(NO_3)_3$	$LaCl_3$	$La(NO_3)_3$
RC	+	-	+	$\oplus$
LLPS	+	-	-	+

7.3.2 Structure conservation

Using FTIR and CD, it was controlled whether the proteins, in particular their secondary structure, remain stable upon adding the trivalent salts or not. FTIR measurements of BSA with YCl_3 and HSA with YCl_3 were reported before[1]. With chloride salts the secondary structure of the proteins is conserved.

In order to establish a connection between the phase diagram shown in Fig. 7.1 and the protein stability measurements, the extension of regime II in BSA-YCl_3 in terms of c_s/c_p is shortly summarized here. At a c_p of 18 mg/ml the second regime in BSA with YCl_3 extends from $c_s/c_p = 3.7 \pm 0.7$ to 59 ± 7. At lower c_p the second regime normally extends to higher c_s/c_p values. At 9 mg/ml for example, the upper boundary of regime II is located at $c_s/c_p = 110 \pm 37$.

Figure 7.3 shows representative FTIR and CD spectra of BSA solutions with $La(NO_3)_3$. The legends show the c_s/c_p ratio. The FTIR spectra are normalized to the peak at 1650 cm^{-1}. Up to a ratio of $c_s/c_p = 170$ the secondary structure is conserved. At $c_s/c_p = 330$ the peak at 1650 cm^{-1} broadens. This indicates a

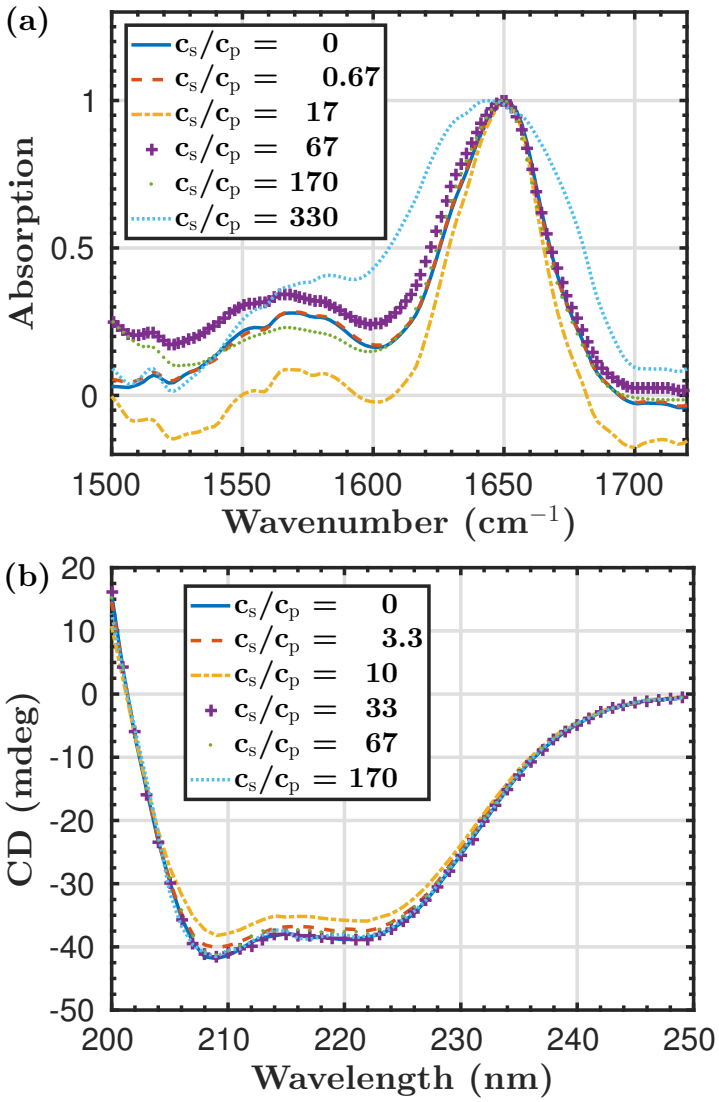

Figure 7.3: *Monitoring of the stability of the secondary protein structure. The legends give the ratio of c_s and c_p.* **(a)** *FTIR measurements for 20 mg/ml BSA with different $La(NO_3)_3$ concentrations.* **(b)** *CD measurements with different salt concentrations for BSA with $La(NO_3)_3$. The protein concentration was 0.2 mg/ml BSA and for the highest salt concentration 0.15 mg/ml BSA.*

change in the secondary structure. This c_s/c_p ratio is, however, far above the c_s/c_P ratios of the samples shown in Fig. 7.1. The CD spectrum for $c_s/c_p = 10$ deviates slightly from the others. At higher c_s/c_p the spectra are similar again to those at lower c_s/c_p. Thus the CD spectra also show a stable secondary structure up to $c_s/c_p = 170$. This is well above the highest c^{**}/c_p value in BSA-YCl_3. Results of further protein stability measurements can be found in the Supporting Material. The results there also show that with very high concentration of nitrate salts, partial unfolding is detectable.

7.3.3 Effective protein-protein interactions characterized by SAXS

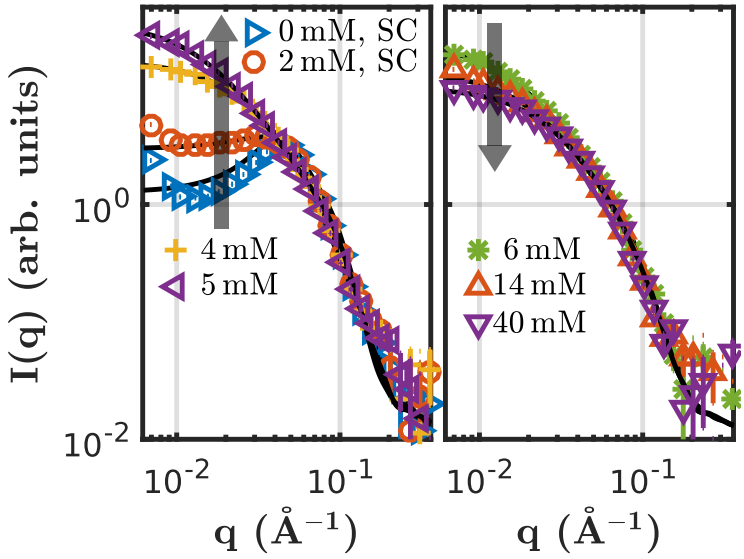

Figure 7.4: *SAXS data with model fits for samples with 50 mg/ml BSA and different concentrations of $La(NO_3)_3$.* ***(a)*** *Approaching to c^*, the scattering intensity at low q increases with increasing salt concentration. SC indicates that the data were fit using a screened Coulombic potential. The other data was fitted with a sticky-hard sphere potential.* ***(b)*** *Further increasing the salt concentration leads to a decrease of the scattering intensity at low q.*

To further quantify the effect of the two anions on the RC phase behavior, SAXS was performed. SAXS measurements for BSA with $LaCl_3$ and for BSA with YCl_3 in H_2O have been reported in a previous publication[168]. The same strategy of measurements and data analysis was applied to BSA with $La(NO_3)_3$. Representative SAXS data with model fitting are presented in Fig. 7.4. The SAXS data show similar trends as for other salts[168]. At low salt concentration, the effective protein-protein interactions are dominated by the net negative charge. A strong correlation peak is

visible. With increasing salt concentration, the low q intensity increases indicating the reduction of repulsion. In this region of the phase diagram (regime I), the solutions are clear. With further increasing salt concentration the systems become more and more dominated by attractive interactions with the attraction reaching its maximum at 5 mM $La(NO_3)_3$. This is close to the c* boundary, which at 50 mg/ml BSA is located at 4.6±0.1 mM $La(NO_3)_3$ (see Fig. 7.1).

The SAXS data fit consists of an ellipsoid form factor and either a screened Coulombic (SC) or a SHS interaction potential. In Fig. 7.4 the fits are superimposed on the data as solid lines. Below c*, the interactions are dominated by electrostatics due to the surface charges. The two scattering curves for samples with very low salt concentrations (0 and 2 mM) were fitted using a screened Coulombic potential. The fitted charges for 0 and 2 mM $La(NO_3)_3$ are 100 e. This is the upper boundary that was set during fitting. The obtained ionic strengths are 31 and 82 mM, respectively. For both SC and SHS potential fits the volume fraction was allowed to vary between 0.02 and 0.036. Furthermore, the rotation axis r_a of the ellipsoid was fixed at 18 Å. At 0 and 2 mM $La(NO_3)_3$ the axis r_b of the ellipsoid was 38 and 49 Å. Starting from 4 mM $La(NO_3)_3$ the scattering intensity was fitted by the SHS potential. For the SHS fits the axis r_b was allowed to vary between 42 and 61 Å. For further details see Tables 13.1

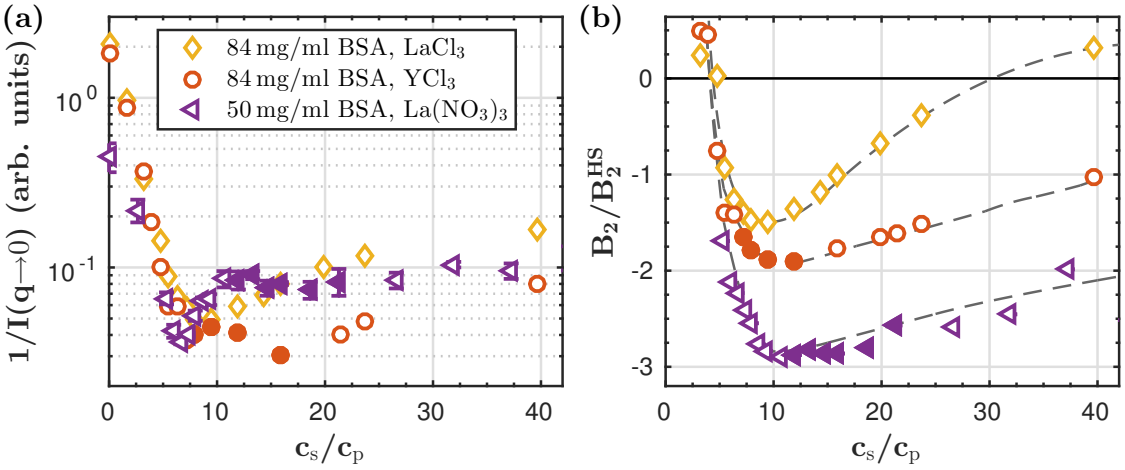

Figure 7.5: **(a)** *B_2/B_2^{HS} from the SAXS data analysis. The filled symbols indicate samples showing LLPS. The dashed lines are guides to the eye.* **(b)** *Inverse scattering intensity at low q (1/(mean of the first three data points)).*

The fitting results, B_2/B_2^{HS}, are shown in Fig. 7.5b together with the inverse of the intensity at low q, $I(q \to 0)$ in Fig. 7.5a. For comparison, the results for BSA-$LaCl_3$ and BSA-YCl_3 from previous work are also shown[168;173].

For B_2/B_2^{HS}, the curves first decrease sharply and then above c* increase slowly again. The values for BSA-$LaCl_3$ are apparently higher than the others and those for BSA-$La(NO_3)_3$ are the lowest, indicating that the nitrate anion enhances the

effective attraction between proteins. The minimum B_2/B_2^{HS} occurs around c_s/c_p = 6, 8 and 9 for $LaCl_3$, YCl_3 and $La(NO_3)_3$, respectively. After the minimum, the values for BSA-YCl_3 increase slower than in BSA-$LaCl_3$, whereas for $La(NO_3)_3$ only a slight increase above c_s/c_p=15 is visible. Note that although the fitting error is smaller than the symbol size, the systematic error for the BSA-$La(NO_3)_3$ series is larger because this data set was not measured at the ESRF but at a laboratory X-ray source. Thus, the trend of the values of B_2/B_2^{HS} should not be overinterpreted. It is however clear that The increase (recovery) is much slower with $La(NO_3)_3$ than with the other two salts.

The reason for the non-symmetric change is most likely the screening effect of the co-ion, Cl^- or NO_3^-. The increasing amount of co-ions screens the effective surface charge of the proteins. Fujihara and Akiyama studied the attractive interaction between macroanions mediated by divalent cations and observed a similar trend of effective interaction potential as a function of cation concentration [125;127].

The scattering at low q, $I(q \to 0)$, adds to this consistent physical picture in a model-free way. Fig. 7.5a shows the inverse of the SAXS intensity at low q. The mean value of the first three intensity data points was taken. The inverse of this value is plotted against the ratio of c_s and c_p. Note here, that the data from ID02, ESRF was calibrated to absolute intensities, whereas the SAXS data from the laboratory source was not calibrated to absolute intensities. Theoretically, $I(0)$ is determined by the compressibility χ_T, since $S(q \to 0) = k_B T \rho\ \chi_T$ [169]. The compressibility χ_T diverges at the spinodal line. Thus, the closer the coexisting densities are, the closer binodal and spinodal lines are, the larger is χ_T and the smaller is $1/I(q \to 0)$ in the coexisting phases. This explains the observation that for samples with YCl_3 and $La(NO_3)_3$ $1/I(q \to 0)$ follows a different behavior compared to samples with with $LaCl_3$. For samples with $LaCl_3$, without LLPS binodal, $1/I(0)$ decreases and increases and follows similar trends as B_2/B_2^{HS} does. For samples with YCl_3 and $La(NO_3)_3$, the existence of the LLPS binodal changes the behavior of $1/I(q \to 0)$: $1/I(q \to 0)$ decreases first, as c_s is increased up to c*. With YCl_3 the system phase-separates (LLPS) in the range of c_s/c_p from 8 to 16. For c_s/c_p=7.1 the system is close to the lower critical point of the LLPS, which results in large values of χ_T and $S(q \to 0)$ and in small values of $1/I(q \to 0)$. As c_s is increased further up to $c_s/c_p = 10$, the coexistence region of the LLPS broadens, causing χ_T to decrease and $1/I(q \to 0)$ to increase (filled purple circles). When further increasing c_s, but still in the LLPS regime, χ_T increases again. Above the LLPS, in regime III, $1/I(q \to 0)$ again follows a trend similar to B_2/B_2^{HS}. The $1/I(q \to 0)$ data for $La(NO_3)_3$ first decreases and after a sharp minimum increases. The LLPS samples (filled symbols) are located above this sharp minimum. The reason for this is not yet clear.

The comparison of phase behavior (Fig.7.1) and interactions (Fig. 7.5) of the four salts suggest that the weaker salt $LaCl_3$ induces RC easier than other salts. Although the attractions (B_2/B_2^{HS}) induced by $LaCl_3$ are not strong enough to induce LLPS at room temperature, it recovers to a much higher value which makes regime III more

stable. In contrast, the strong attraction induced by the stronger salts needs higher salt concentrations to enter regime III. Re-entrant occurs when the re-established repulsion can balance the short-ranged attraction via cation bridging. Thus, when a strong salt is used, such as YCl_3 vs $LaCl_3$, the strong bridging effect needs higher charge inversion to balance, which explains the broadening of regime II. When a salt is too strong, such as $Y(NO_3)_3$, even at the maximum repulsion, it is still weaker than the bridging, thus regime II disappears.

7.4 Conclusions

In this work, we have performed a systematic study of the phase behavior and interactions in BSA solutions in the presence of four different trivalent salts, focusing on the effect of anions. The results demonstrate that replacing Cl^- by NO_3^- has a strong impact on interactions and the resulting phase behavior in protein solutions. With NO_3^- the effective attraction in regime II is enhanced. This is found by visual inspection of the sample solutions where the RC behavior becomes partial. A quantitative analysis of the effective interactions, using SAXS, further corroborates the enhanced attraction with NO_3^-.

We thank Dr. F. Roosen-Runge for valuable discussions N. Scheffzyk and S. Schoenberg helped with the phase diagram and the UV-vis measurements. We gratefully acknowledge funding from DFG, as well as allocation of beamtime at the ESRF, Grenoble, France.

Part III

Conclusions & Outlook

Chapter 8

Conclusions

The effective interactions in the model system of BSA in solution with a trivalent salt were studied. The results improve the understanding of the physical mechanisms behind protein aggreagtion, protein cluster formation and protein crystallization. There are several parameters that influence the effective interactions in the studied model system. In this thesis the focus is on the effect of the solvent isotope as well as on the effect of different cations and anions. As a basis for further work, protein cluster formation is studied in a pure protein system. To address cluster formation, static and dynamic methods are combined in a unique way. Furthermore, an existing study on protein clusters in the model system of BSA and trivalent salt is extended.

The cations that were used are Y^{3+} and La^{3+}. The usage of Y^{3+} leads to stronger attraction than the usage of La^{3+}. Regarding the solvent isotpe, in D_2O the entropy-driven attractions are stronger than in H_2O. Below the lower salt concentration boundary of the RC, c^*, the interactions are neither influenced by replacing H_2O with D_2O nor by the nature of the cation. In this regime I of the RC electrostatic repulsion dominates. As soon as in regime II attractive interactions become important, the solvent isotope or the nature of the cation affect the phase behavior. Solutions with $LaCl_3$ turn from slightly turbid due to very small clusters to samples that show LLPS or larger precipitates when H_2O is replaced by D_2O. Solutions with YCl_3 show LLPS or larger precipitates already in H_2O. In D_2O LLPS is not observed anymore because the attraction is too strong. Regime II broadens when D_2O or Y^{3+} is used. The upper salt concentration boundary of the RC, c^{**}, thus moves to higher salt concentrations. This macroscopically observed phase behavior is confirmed very well by a quantitative analysis of SAXS data. Both model fits with the SHS potential and the low scattering vector (q) intensity show the first increasing and then slowly decreasing attraction. The reduced second virial coefficient (B_2/B_2^{HS}) values are lower with Y^{3+} instead of La^{3+} or with D_2O instead of H_2O. The solvent isotope effect was further investigated by monitoring the change of the critical solution temperature for increasing D_2O solvent fraction. In the accessible solvent fraction range, the critical solution temperature decreases linearly. The attraction between the protein molecules is driven by the entropy that is released when ion bridges are formed. In D_2O the rearrangement of the hydration waters around carboxy groups and trivalent cations thus seems to result in a higher entropy gain as in H_2O.

Another parameter which influences the strength of the attraction between BSA

molecules in aqueous solutions of BSA and trivalent salt is the nature of the anion. Two anions that are quite close in the Hofmeister series were studied, namely Cl^- and NO_3^-. Despite their close proximity in the Hofmeister series and although salt concentrations below 50 mM were used, the exchange of Cl^- by NO_3^- strongly affects the phase behavior. The B_2/B_2^{HS} values are lower with NO_3^- than with Cl^-. Furthermore, the reentrant condensation which is complete in BSA with $LaCl_3$ is only partial in BSA with $La(NO_3)_3$. Samples with BSA and $La(NO_3)_3$ show strong aggregation and in a certain salt concentration-protein concentration (c_s-c_p) regime also LLPS. Samples with BSA and $LaCl_3$ turn only slightly turbid and show no LLPS at room temperature. All findings show that, compared to Cl^-, NO_3^- enhances the attraction. The probability for ion bridge formation increases strongly. Because the attraction is so strong, the system does not become repulsive again.

Experiments with colloids and computer simulations have shown that cluster formation occurs when a long-range repulsion is combined with a short-range attraction. Motivated by these findings, cluster formation in protein solutions is debated. The combination of SAXS, NSE and NBS provides a new framework to study macromolecular clusters. In this thesis clustering in pure BLG protein solutions was studied. The static SAXS data can be modeled using an ellipsoid form factor and either a Screened Coulombic or a Two-Yukawa potential. The two different potentials yield a different scaling of the correlation peak vs. volume fraction. The correlation peaks that were extracted from the Two-Yukawa potential yield a scaling which is comparable to the scaling of the correlation peaks that were extracted from the experimental structure factor. The model free structure factor from NSE helps to further nail down the Two-Yukawa potential as the model that describes the system correctly. The scaling of the correlation peak vs. volume fraction allows to estimate the number density of clusters in each sample. With NBS it is possible to access the hydrodynamic radius of the clusters. By combining the static (SAXS) and dynamic (NBS) results, the scaling of the hydrodynamic radius vs. the number of dimers per cluster is obtained. This scaling shows that the clusters are compact and static on the observation timescale. The upper limit of the observation timescale is set by the range in which the NSE data decays exponentially and is approximately 50 ns. The NSE and NBS data that were taken show further that NSE and NBS are compatible. The large q limit of the NSE data converges to the results obtained using NBS. Note also that the clustering behavior of BLG did not show a difference when D_2O was used instead of H_2O. SAXS measurements were performed with BLG in both solvents. The dependence of the position of the correlation peak q_c on the protein volume fraction φ was the same. In contrast to the solutions with BSA and trivalent salt where the solvent isotope has a strong effect, the interactions in the pure BLG solutions seem to not be influenced by the solvent isotope.

In the aqueous BSA system with trivalent salt cluster formation in regimes I and III was studied using dynamic light scattering. At protein concentrations from 5 to 25 mg/ml BSA, the intermediate scattering function shows two modes. The faster

one is tentatively assigned to monomers, the slower one to clusters. Consistently with the finding that the second regime is narrower in $LaCl_3$, the cluster collective diffusion coefficient in $LaCl_3$ increases again in regime III at c_s/c_p ratios where the cluster collective diffusion coefficient in YCl_3 is still large. Due to multiple scattering effects the data taken in regime II for BSA with $LaCl_3$ has to be interpreted with caution. Tentatively, it can be concluded that c^* is not a spinodal line because the collective diffusion coefficient does not go to zero but instead levels off at a nonzero value.

Chapter 9

Outlook

The microscopic origin of the strong difference in the attraction between proteins in the BSA system with trivalent salt in H_2O vs. D_2O is not yet known in detail. Probably the difference is due to a difference in the enthalpies and entropies of hydration. Moreover, there might be a difference in the strength of the hydrogen bonds. The existing literature on this topic does not allow for a final conclusion. What might help to elucidate this point is a comparative calorimetry study in both H_2O and D_2O, similar to the experiments performed by Matsarskaia et al.[45]. A comparison of the binodals in H_2O and D_2O has been started (Focus Module of Andreas Dörr). It would be interesting to see how much the LCST changes. This change could be compared to work by other groups (Bucciarelli et al.[110]).

The combination of static and dynamic methods, namely SAXS, NBS and NSE, allows to study cluster formation in macromolecular solutions. The established method has to be applied to further systems. One system is that of BSA in solution with trivalent salts. Another possible system is the lysozyme system. So far there is no NBS study using lysozyme. A method has to be found to prevent corrosion of the aluminium sample holder as lysozyme solutions generally have an acidic pH.

Note in this context that not every protein does show cluster formation when the volume fraction is increased. BSA is an example for a system in which the constituents remain monomeric[155]. The reason for this difference between BSA and BLG is another topic for future research.

The light scattering measurements could be extended to further systems. Samples with $LaCl_3$ in D_2O could be measured or samples with $La(NO_3)_3$ instead of $LaCl_3$. Inter alia, this would show whether there is a systematic relationship between the onset of collective cluster formation in regime I and the strength of the effective attraction. In solutions with $LaCl_3$ the clustering monitored by DLS starts at a lower salt concentration-protein concentration (c_s/c_p) ratio than in YCl_3. The reason for this remains to be resolved, considering also the fact that the self-diffusion coefficients measured by NBS show the opposite trend (cf. work by Christian Beck).

To complete the collected data that shows the effect of exchanging Cl^- by NO_3^-, further experiments can be performed. The protein concentration in the supernatant could additionally be monitored in BSA with $Y(NO_3)_3$. Furthermore, a series of zeta potential measurements with both $LaCl_3$ and $La(NO_3)_3$ which shows how the surface potential evolves with the two salts would be helpful.

Part IV

Appendix

Chapter 10

Supporting Information for Publication A

10.1 SAXS data analysis

10.1.1 Form factor and screened Coulombic potential

As form factor a rotational ellipsoid, defined by the two radii R_a and R_b, is used. The rotation axis of the ellipsoid is in direction of R_a and the ratio between R_a and R_b determines whether the ellipsoid has an oblate or a prolate shape. The form factor is calculated as[80;174]

$$P(q) = c \cdot \Delta\rho^2 \int_0^1 \frac{3j_1(z)}{z} dx. \tag{10.1}$$

Herein $z = qR_b\sqrt{(1 + x^2[(R_a/R_b)^2 - 1])}$ and $j_1(z)$ is the first-order spherical Bessel function.

The screened Coulombic potential[54;55;80] is given by:

$$\beta U(r) = \begin{cases} \infty & r \leq \sigma \\ \frac{\beta Z^2}{\pi\epsilon\epsilon_0(2+\kappa\sigma)^2} \cdot \frac{e^{-\kappa(r-\sigma)}}{r} & r > \sigma. \end{cases} \tag{10.2}$$

Z is the charge of the particles, ϵ_0 and ϵ are the dielectric constants in vacuo and of the solvent. σ is the diameter of the particles and κ is the inverse Debye screening length[175],

$$\kappa = \sqrt{\frac{\sum_i c_i z_i^2}{\epsilon\epsilon_0 k_B T}}, \tag{10.3}$$

with c_i the ion concentration in the bulk solution and z_i the charge of the ion. The sum runs over all ions present in the solution.

10.1.2 Fitting parameters for 85 and 87 mg/ml BSA with $LaCl_3$ in H_2O and D_2O

For the ellipsoid form factor the rotation axis R_a was set to 18 Å. The size of the second axis R_b was set to either 42 Å (salt concentrations from 0 to 4 mM) or to 61 Å for higher salt concentrations. The scattering length density was fixed to $1.24 \cdot 10^{-5}$ Å^{-2}. The volume fraction ϕ was set to $\phi = 0.733 \cdot c_p/1000$, where c_p of a reference sample was determined using UV-vis spectroscopy. The background intensity was set to the (mean) value the data takes at high q. For the SC potential the temperature was set to 298 K and the dielectric constant to $\epsilon = 81$ As/Vm. For the SHS potential (see main text) the perturbation parameter δ was fixed to 0.01.

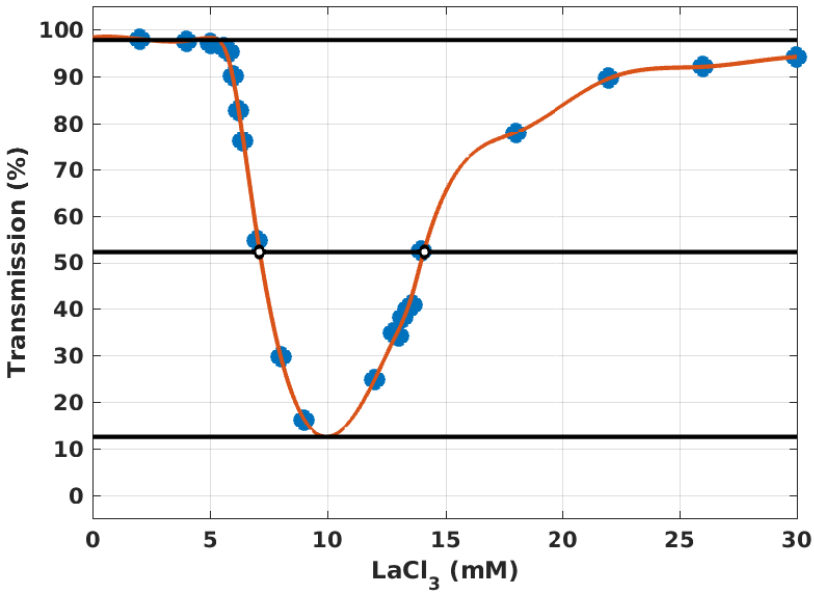

Figure 10.1: *Example UV-vis absorption plot of BSA with $LaCl_3$ in pure H_2O. The central black line was used to determine c^* and c^{**}. This line was located by determining the mean of the first few points and the minimum of an interpolant (upper and lower black lines). The central black line is located in between the other two lines. As a reference a measurement for 20 mg/ml BSA with YCl_3 in H_2O was performed. The state diagram of BSA with YCl_3 in H_2O is established very well and in this system the boundaries may also be determined by visual inspection. The transmission measurement method works well for protein concentrations below 100 mg/ml.*

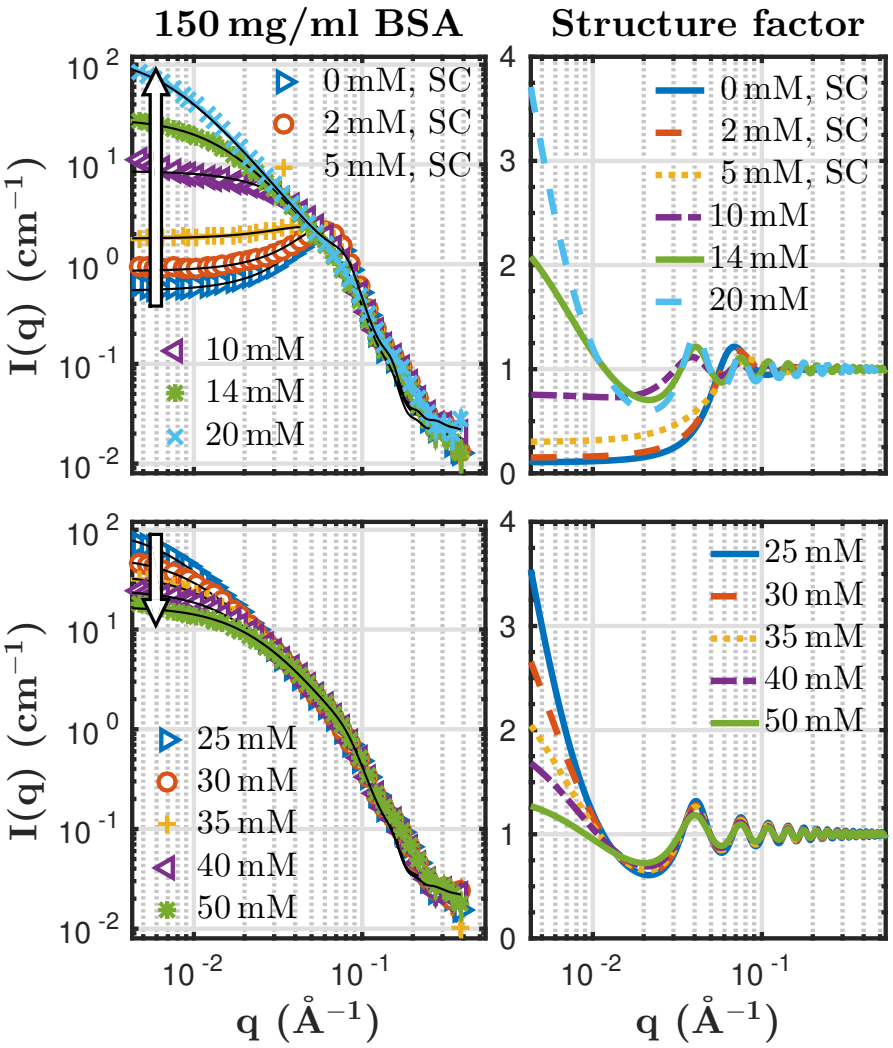

Figure 10.2: *SAXS intensities for 150 mg/ml BSA in H_2O and corresponding structure factors for different concentrations of $LaCl_3$. In the legend, SC indicates that the screened Columbic potential was used for data fitting. The other data were fitted using the SHS potential. In the upper part the scattering intensity at low q increases with increasing salt concentration. In the lower part it decreases with increasing salt concentration. For the ellipsoid form factor the rotation axis R_a was set to 18 Å. The size of the second axis R_b was set to either 42 Å (salt concentrations from 0 to 5 mM) or to 61 Å for higher salt concentrations. The scattering length density was fixed to $1.24 \cdot 10^{-5}$ Å^{-2}. The volume fraction ϕ was set to $\phi = 0.733 \cdot c_p/1000$, where c_p of a reference sample was determined using UV-vis spectroscopy. The background intensity was set to the (mean) value the data takes at high q. For the SC potential the temperature was set to 298 K and the dielectric constant to $\epsilon = 81$ As/Vm. For SHS potential the perturbation parameter δ was fixed to 0.01.*

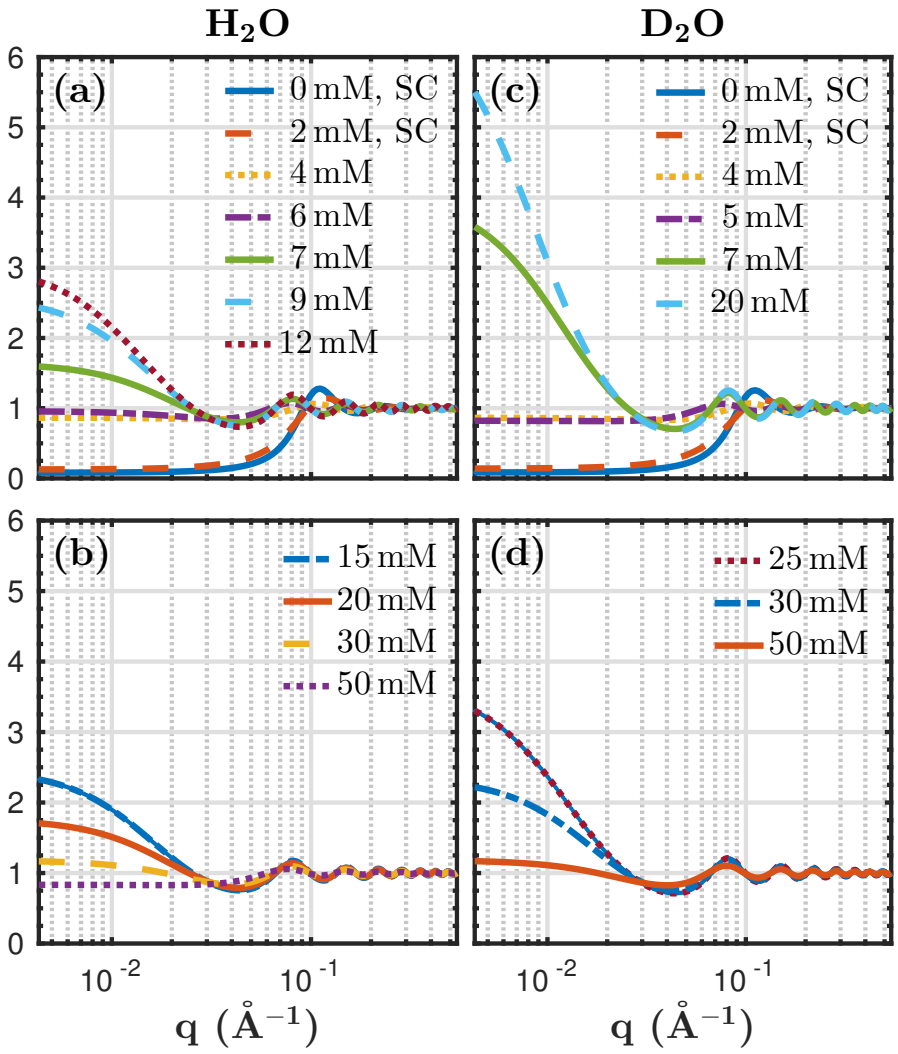

Figure 10.3: *Structure factors corresponding the to the SAXS data presented in Fig. 3 in the main text.* **(a, c)***: With increasing salt concentration $S(q \to 0)$ increases.* **(b, d)***: With increasing salt concentration $S(q \to 0)$ decreases. $S(q \to 0)$ becomes attractive around c^*. The c^* value is about 7.5 mM for 85 mg/ml BSA in H_2O. In D_2O the c^* value is 6.0±1.0 mM.*

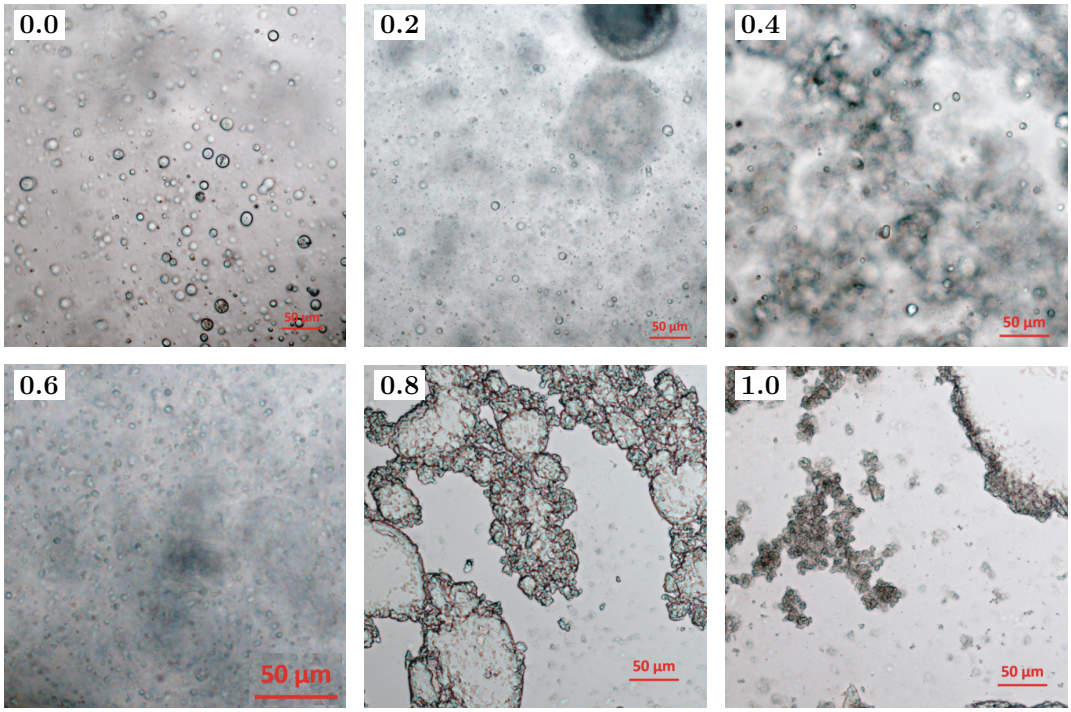

Figure 10.4: *Series of microsope pictures for samples with 91.7 mg/ml BSA, 12 mM YCl_3 and varying solvent fractions of D_2O (the solvent fraction is indicated in the white boxes in the figures).*

10.2 Values of the fit parameters for the BSA with $LaCl_3$ and BSA with YCl_3 data

Table 10.1: *Fit parameters for 87 mg/ml BSA with $LaCl_3$ in D_2O. The perturbation parameter ϵ for the SHS potential is given by $\epsilon = \Delta/(\sigma + \Delta)$. See the main text of the paper for further information on the potential. Fixed parameters or parameters that ended in one of the given borders are written in blue.*

c_s (mM)	0	2	4	5	7	8	10	12
Vol. frac.	6.70e-02	6.70e-02	6.70e-02	6.70e-02	6.70e-02	3.70e-02	2.00e-02	2.30e-02
R_a(Å)	18	18	18	18	18	18	18	18
R_b(Å)	42	42	42	61	61	61	61	61
ρ_{ell}(Å^{-2})	1.24e-05	1.24e-05	1.24e-05	1.24e-05	1.24e-05	1.24e-05	1.24e-05	1.24e-05
ρ_{solv}(Å^{-2})	1.037e-05	1.030e-05	1.025e-05	1.036e-05	1.026e-05	1.011e-05	9.906e-06	1.006e-05
Pert. par. ϵ			0.01	0.01	0.01	0.01	0.01	0.01
Stickiness τ			3.17e-01	3.64e-01	9.78e-02	8.25e-02	6.78e-02	7.19e-02
Charge (e)	16.3	8.71						
Monov. Salt (mM)	6.18	8.59						
Temp. (K)	298	298						
Dielectric const. ϵ	81	81						
incoh. bkg.	1.1675e-02	1.1675e-02	1.1675e-02	1.1675e-02	1.1675e-02	6.50e-03	3.50e-03	4.00e-03
u_0 (k_BT)			3.27	3.13	4.45	4.62	4.81	4.75
B_2/B_2^{HS}			0.210	0.313	-1.56	-2.03	-2.69	-2.48

Table 10.2: *Fit parameters for 87 mg/ml BSA with $LaCl_3$ in D_2O. The perturbation parameter ϵ for the SHS potential is given by $\epsilon = \Delta/(\sigma + \Delta)$. See the main text of the paper for further information on the potential. Fixed parameters or parameters that ended in one of the given borders are written in blue.*

c_s (mM)	15	20	25	27	30	50
Vol. frac.	3.10e-02	6.70e-02	6.70e-02	6.70e-02	6.70e-02	6.70e-02
R_a(Å)	18	18	18	18	18	18
R_b(Å)	61	61	61	61	61	61
ρ_{ell}(Å^{-2})	1.24e-05	1.24e-05	1.24e-05	1.24e-05	1.24e-05	1.24e-05
ρ_{solv}(Å^{-2})	1.006e-05	1.025e-05	1.022e-05	1.025e-05	1.03e-05	
Pert. par. ϵ	0.01	0.01	0.01	0.01	0.01	0.01
Stickiness τ	7.66e-02	9.32e-01	9.92e-02	1.04e-01	1.11e-01	1.81e-01
Charge (e)						
Monov. Salt (mM)						
Temp. (K)						
Dielectric const. ϵ						
incoh. bkg.	5.40e-03	1.1675e-02	1.1675e-02	1.1675e-02	1.1675e-02	1.1675e-02
u_0 (k_BT)	4.69	4.49	4.43	4.38	4.32	3.83
B_2/B_2^{HS}	-2.26	-1.68	-1.52	-1.40	-1.25	-0.379

Table 10.3: *Fit parameters for 85 mg/ml BSA with $LaCl_3$ in H_2O. The perturbation parameter ϵ for the SHS potential is given by $\epsilon = \Delta/(\sigma + \Delta)$. See the main text of the paper for further information on the potential. Fixed parameters or parameters that ended in one of the given borders are written in blue.*

c_s (mM)	0	2	4	6	7	8	9	10
Vol. frac.	6.20e-02	6.20e-02	6.20e-02	6.20e-02	6.20e-02	6.20e-02	6.20e-02	6.20e-02
R_a(Å)	18	18	18	18	18	18	18	18
R_b(Å)	42	42	42	61	61	61	61	61
ρ_{ell}(Å^{-2})	1.24e-05	1.24e-05	1.24e-05	1.24e-05	1.24e-05	1.24e-05	1.24e-05	1.24e-05
ρ_{solv}(Å^{-2})	1.035e-05	1.028e-05	1.025e-05	1.034e-05	1.032e-05	1.029e-05	1.028e-05	1.024e-05
Pert. par. ϵ			0.01	0.01	0.01	0.01	0.01	0.01
Stickiness τ			3.27e-01	2.55e-01	1.30e-01	1.11e-01	1.05e-01	1.01e-01
Charge (e)	18.1	10.3						
Monov. Salt (mM)	7.41	10.3						
Temp. (K)	298	298						
Dielectric const. ϵ	81	81						
incoh. bkg.	1.20e-02	1.20e-02	1.20e-02	1.20e-02	1.20e-02	1.20e-02	1.20e-02	1.20e-02
u_0 (k_BT)			3.24	3.49	4.16	4.32	4.38	4.41
B_2/B_2^{HS}			0.235	2.05e-02	-0.921	-1.25	-1.39	-1.48

Table 10.4: *Fit parameters for 85 mg/ml BSA with $LaCl_3$ in H_2O. The perturbation parameter ϵ for the SHS potential is given by $\epsilon = \Delta/(\sigma + \Delta)$. See the main text of the paper for further information on the potential. Fixed parameters or parameters that ended in one of the given borders are written in blue.*

c_s (mM)	12	15	18	20	25	30	50
Vol. frac.	6.20e-02	6.20e-02	6.20e-02	6.20e-02	6.20e-02	6.20e-02	6.20e-02
R_a(Å)	18	18	18	18	18	18	18
R_b(Å)	61	61	61	61	61	61	61
ρ_{ell}(Å^{-2})	1.24e-05	1.24e-05	1.24e-05	1.24e-05	1.24e-05	1.24e-05	1.24e-05
ρ_{solv}(Å^{-2})	1.025e-05	1.026e-05	1.026e-05	1.028e-05	1.03e-05	1.03e-05	1.036e-05
Pert. par. ϵ	0.01	0.01	0.01	0.01	0.01	0.01	0.01
Stickiness τ	1.00e-01	1.06e-01	1.15e-01	1.24e-01	1.49e-01	1.80e-01	3.66e-01
Charge (e)							
Monov. Salt (mM)							
Temp. (K)							
Dielectric const. ϵ							
incoh. bkg.	1.20e-02	1.20e-02	1.20e-02	1.20e-02	1.20e-02	1.20e-02	1.20e-02
u_0 (k_BT)	4.42	4.36	4.28	4.21	4.02	3.84	3.13
B_2/B_2^{HS}	-1.50	-1.35	-1.18	-1.01	-0.673	-0.391	0.317

Table 10.5: *Fit parameters for 85 mg/ml BSA with YCl_3 in H_2O. The perturbation parameter ϵ for the SHS potential is given by $\epsilon = \Delta/(\sigma + \Delta)$. See the main text of the paper for further information on the potential. Fixed parameters or parameters that ended in one of the given borders are written in blue.*

c_s (mM)	0	2	4	5	6	7	8	9
Vol. frac.	6.20e-02	6.20e-02	6.20e-02	6.20e-02	6.20e-02	6.20e-02	6.20e-02	6.20e-02
R_a(Å)	18	18	18	18	18	18	18	18
R_b(Å)	42	42	42	61	61	61	61	61
ρ_{ell}(Å^{-2})	1.24e-05	1.24e-05	1.24e-05	1.24e-05	1.24e-05	1.24e-05	1.24e-05	1.24e-05
ρ_{solv}(Å^{-2})	1.035e-05	1.029e-05	1.023e-05	1.039e-05	1.035e-05	1.032e-05	1.033e-05	1.028e-05
Pert. par. ϵ			0.01	0.01	0.01	0.01	0.01	0.01
Stickiness τ			3.27e-01	2.55e-01	1.30e-01	1.11e-01	1.05e-01	1.01e-01
Charge (e)	19.8	10.3						
Monov. Salt (mM)	9.44	12.0						
Temp. (K)	298	298						
Dielectric const. ϵ	81	81						
incoh. bkg.	1.17e-02	1.17e-02	1.17e-02	1.17e-02	1.17e-02	1.17e-02	1.17e-02	1.17e-02
u_0 (k_BT)			2.81	2.90	4.07	4.38	4.39	4.48
B_2/B_2^{HS}			0.500	0.453	-0.751	-1.40	-1.42	-1.66

Table 10.6: *Fit parameters for 85 mg/ml BSA with YCl_3 in H_2O. The perturbation parameter ϵ for the SHS potential is given by $\epsilon = \Delta/(\sigma + \Delta)$. See the main text of the paper for further information on the potential. Fixed parameters or parameters that ended in one of the given borders are written in blue.*

c_s (mM)	10	12	15	20	25	27	30	50
Vol. frac.	5.20e-02	4.50e-02	4.50e-02	5.80e-02	6.20e-02	6.20e-02	6.20e-02	6.20e-02
R_a(Å)	18	18	18	18	18	18	18	18
R_b(Å)	61	61	61	61	61	61	61	61
ρ_{ell}(Å^{-2})	1.24e-05	1.24e-05	1.24e-05	1.24e-05	1.24e-05	1.24e-05	1.24e-05	1.24e-05
ρ_{solv}(Å^{-2})	1.026e-05	1.028e-05	1.026e-05	1.023e-05	1.025e-05	1.025e-05	1.027e-05	1.030e-05
Pert. par. ϵ	0.01	0.01	0.01	0.01	0.01	0.01	0.01	0.01
Stickiness τ	8.97e-02	8.65e-02	8.60e-02	9.03e-02	9.44e-02	9.58e-02	9.93e-02	
Charge (e)								
Monov. Salt (mM)								
Temp. (K)								
Dielectric const. ϵ								
incoh. bkg.	9.80e-03	8.50e-03	8.40e-03	1.09e-02	1.17e-02	1.17e-02	1.17e-02	1.17e-02
u_0 (k_BT)	4.53	4.57	4.57	4.52	4.48	4.47	4.43	4.22
B_2/B_2^{HS}	-1.79	-1.89	-1.91	-1.77	-1.65	-1.61	-1.52	-1.03

Table 10.7: *Fit parameters for 150 mg/ml BSA with $LaCl_3$ in H_2O. The perturbation parameter ϵ for the SHS potential is given by $\epsilon = \Delta/(\sigma + \Delta)$. See the main text of the paper for further information on the potential. Fixed parameters or parameters that ended in one of the given borders are written in blue.*

c_s (mM)	0	2	5	10	14	20	25	30
Vol. frac.	1.10e-01	1.10e-01	1.10e-01	1.10e-01	8.90e-02	1.10e-01	1.10e-01	1.10e-01
R_a(Å)	18	18	18	18	18	18	18	18
R_b(Å)	42	42	42	61	61	61	61	61
ρ_{ell}(Å^{-2})	1.24e-05	1.24e-05	1.24e-05	1.24e-05	1.24e-05	1.24e-05	1.24e-05	1.24e-05
ρ_{solv}(Å^{-2})	1.056e-05	1.045e-05	1.038e-05	1.049e-05	1.032e-05	1.032e-05	1.032e-05	1.035e-05
Pert. par. ϵ				0.01	0.01	0.01	0.01	0.01
Stickiness τ				3.17e-01	1.17e-01	1.03e-01	1.04e-01	1.12e-01
Charge (e)	16.4	15.9	6.15					
Monov. Salt (mM)	9.67	19.2	15.3					
Temp. (K)	298	298	298					
Dielectric const. ϵ	81	81	81					
incoh. bkg.	2.10e-02	2.10e-02	2.10e-02	2.10e-02	1.70e-02	2.10e-02	2.10e-02	2.10e-02
u_0 (k_BT)				3.27	4.27	4.40	4.38	4.31
B_2/B_2^{HS}				0.212	-1.14	-1.44	-1.40	-1.24

Table 10.8: *Fit parameters for 150 mg/ml BSA with $LaCl_3$ in H_2O. The perturbation parameter ϵ for the SHS potential is given by $\epsilon = \Delta/(\sigma + \Delta)$. See the main text of the paper for further information on the potential. Fixed parameters or parameters that ended in one of the given borders are written in blue.*

c_s (mM)	35	40	50
Vol. frac.	1.20e-01	1.10e-01	1.10e-01
R_a(Å)	18	18	18
R_b(Å)	61	61	61
ρ_{ell}(Å^{-2})	1.24e-05	1.24e-05	1.24e-05
ρ_{solv}(Å^{-2})	1.044e-05	1.040e-05	1.043e-05
Pert. par. ϵ	0.01	0.01	0.01
Stickiness τ	1.25e-01	1.36e-01	1.65e-01
Charge (e)			
Monov. Salt (mM)			
Temp. (K)			
Dielectric const. ϵ			
incoh. bkg.	2.20e-02	2.05e-02	2.10e-02
u_0 (k_BT)	4.20	4.11	3.92
B_2/B_2^{HS}	-1.01	-0.832	-0.519

Chapter 11

Supporting Information for Publication B

11.1 List of samples measured on IN16B and fit results

Table 11.1: *Fit parameters for fits shown in Fig. 5.1 in the main article. The data are fitted by $q_c = a * \varphi^b$. SC and 2Y represent the Screened-Coulomb and Two-Yukawa model, respectively.*

	a ($\mathring{A}^{-1}$)	da ($\mathring{A}^{-1}$)	b	db
Int.	0.058	0.004	0.11	0.03
SC	0.14	0.01	0.28	0.03
exp.	0.075	0.007	0.13	0.03
2Y	0.068	0.006	0.10	0.03

Table 11.2: *List of samples measured at IN16B and the resulting diffusion coefficients and calculated hydrodynamic radii from different models. 2Y represents the Two-Yukawa model.*

BLG (g/l)	φ	D ($\frac{\mathring{A}^2}{ns}$)	dD ($\frac{\mathring{A}^2}{ns}$)	$R_h^{\text{exp.}}$ ($\mathring{A}$)	$dR_h^{\text{exp.}}$ ($\mathring{A}$)	R_h^{2Y} ($\mathring{A}$)	dR_h^{2Y} ($\mathring{A}$)
76	0.054	5.67	0.26	33.4	0.9	33.5	1.0
110	0.076	5.02	0.20	35.0	0.7	35.4	0.8
140	0.095	4.70	0.21	35.6	0.7	36.1	0.8
161	0.11	3.86	0.24	38.3	0.9	39.0	1.0
200	0.13	3.58	0.20	38.7	0.7	39.6	0.8
250	0.16	3.07	0.24	39.9	0.9	41.2	1.0
300	0.18	2.70	0.16	40.8	0.6	42.2	0.7

11.2 Additional SAXS data

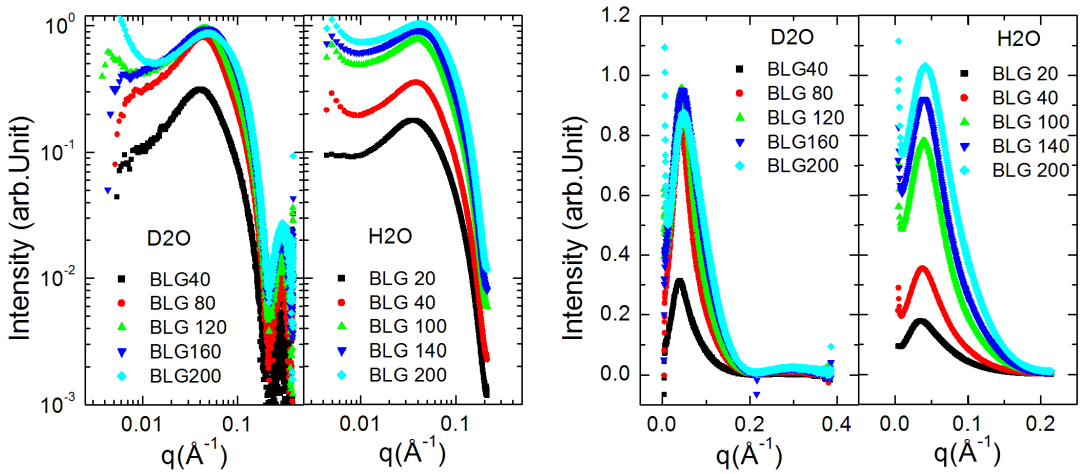

Figure 11.1: *SAXS data for BLG solutions in H_2O and D_2O, respectively, in both linear and log scales. In both cases, the peak position shifts slightly to higher q with increasing protein concentration. Note that the first few data points at low q for samples with low protein concentrations may be affected by large systematic errors due to the background correction as they are very close to the beam-stop. The low-q values thus should not be considered for the overall trend.*

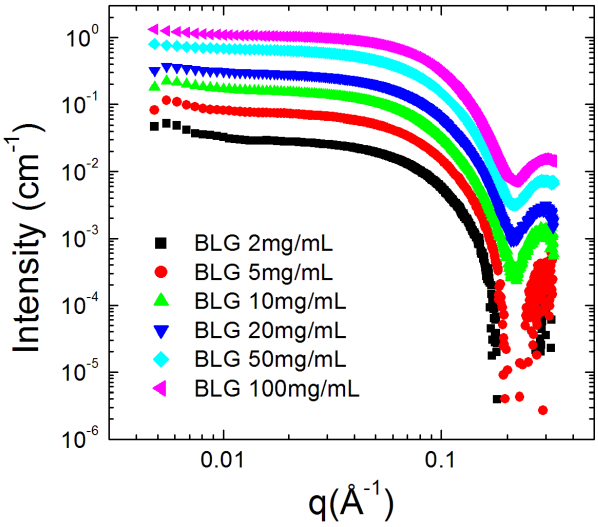

Figure 11.2: *SAXS data for BLG solutions with a concentration series from 2 to 100 mg/ml in buffer (20 mM HEPES buffer and 150 mM NaCl). The similar shape of the SAXS profiles suggests the dominance of one type of particle in the solution.*

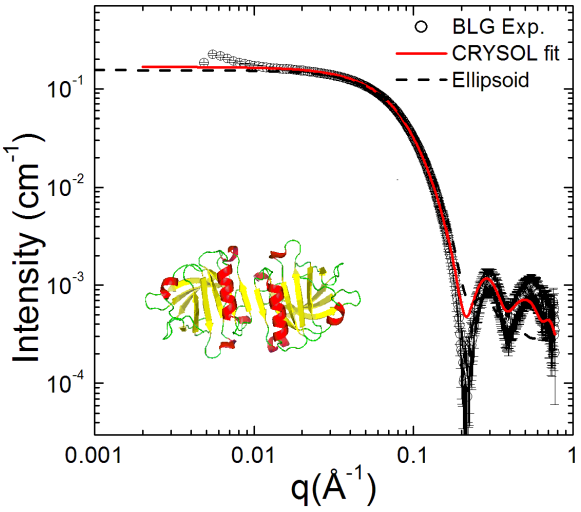

Figure 11.3: *Form factor of the BLG dimer. BLG 10 mg/mL in 20 mM HEPES buffer with 150 mM NaCl. SAXS measurements at ID2, ESRF were performed with two sample-to-detector distances (1m and 5m), thus covering a broad q-range. The merged data is presented together with a CRYSOL fit[176] using the crystal structure of the BLG dimer (PDB code: 1BEB). This result together with the concentration series in Fig. 11.2 corroborates the dominance of BLG dimers in solution[177]. The ellipsoid form factor (rotation axis $R_a = 38$ Åand $R_b = 19$ Å) for the direct model fit is also shown for comparison. It is evident that both form factors fit the experimental SAXS data well in the range of q from 0.01 to 0.15 Å^{-1}.*

11.3 Radial hydrogen density distribution function

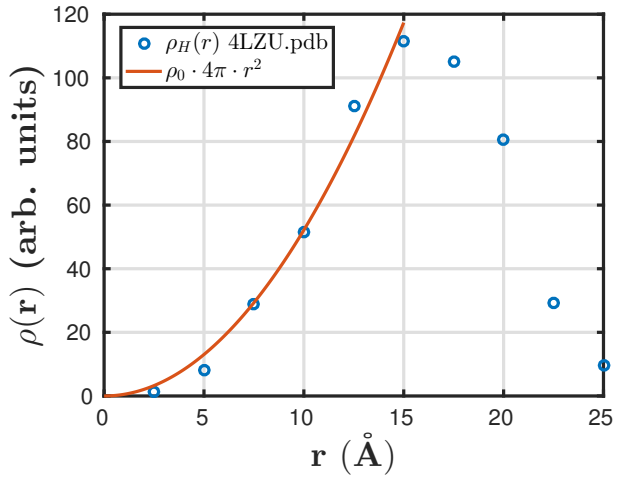

Figure 11.4: *Radial hydrogen density distribution function as calculated using GROMACS[178] (blue symbols). Solid line: fit of the quadratic part by* $\rho_0 \cdot 4\pi \cdot r^2$.

11.4 Purity of the BLG protein sample

The actual purities of the BLG samples by Sigma-Aldrich are generally much above the specification of 90% purity. We have used BLG L3908, batch number SLBP0421V. The certificate of analysis provided by Sigma-Aldrich states that using gel electrophoresis, no impurities were found in this batch.

Our characterization of the protein used in this study by Size Exclusion Chromatography (using a Superdex 200 Increase 3.2/300 column) and 12% SDS-polyacrylamide gel electrophoresis confirm a highly monodisperse sample, dominated by the beta-lactoglobulin dimer (Figure S5). The additional SAXS measurements reported in Figure 11.3 further confirm that the BLG dimer is the main ingredient.

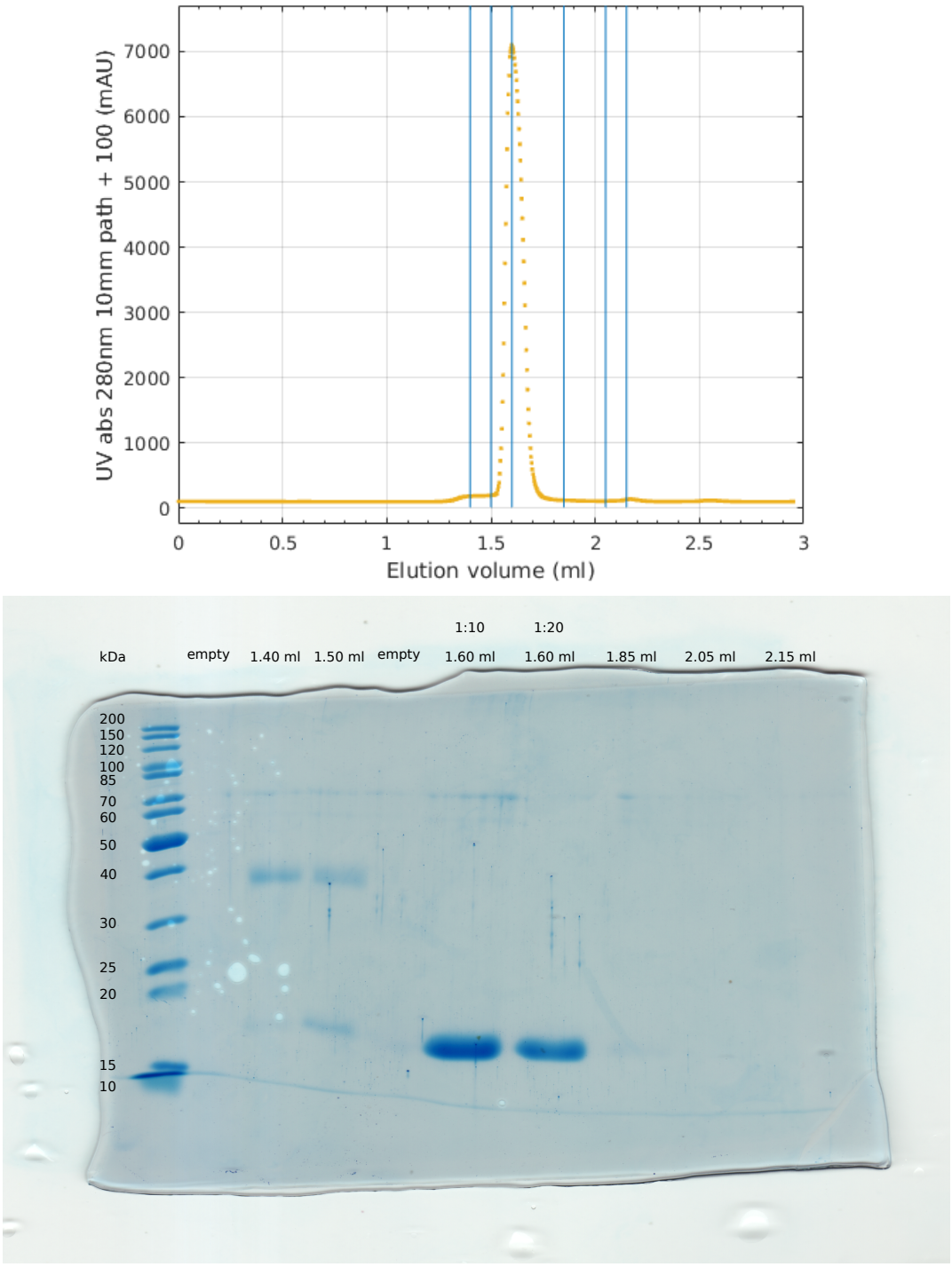

Figure 11.5: *Size exclusion chromatography (top) and gel electrophoresis (bottom) of the used protein BLG show a highly monodisperse sample dominated by the BLG dimer. Lines in the top graph outline the fractions shown in the bottom graph.*

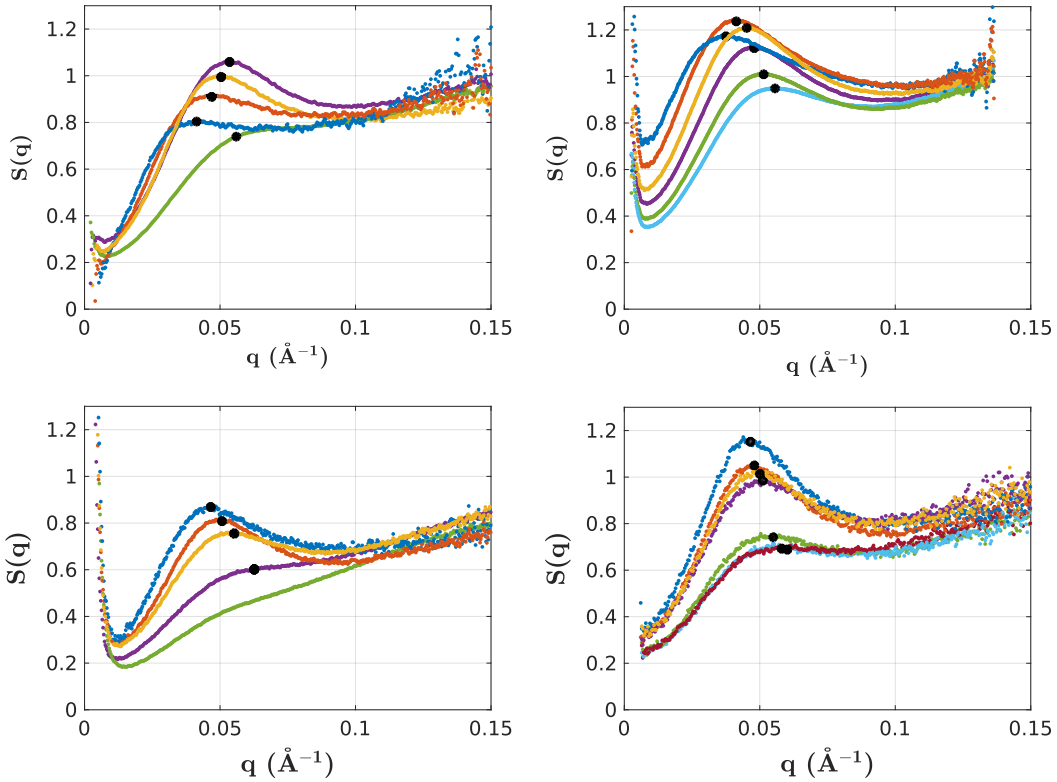

Figure 11.6: *Experimental structure factors. The measured intensity was divided by the BLG dimer form factor. From left to right, top to bottom: SC3139_RT, SC3274, SC3858, inh_201608. The peak positions are marked by black circles.*

11.5 Fits and structure factors obtained for different data sets

Here, the fits and the corresponding structure factors that were obtained for the different BLG data sets are shown. The *SC3139* data was measured end of March, beginning of April 2011 at ID02 (ESRF). The *SC3274* data was measued in November 2011 at ID02 (ESRF). The *SC3858* data was measured in September 2014 at ID02 (ESRF). The *inh_201608* data set was measured at the laboratory X-ray source in August 2016. *inh* stands for "inhouse" and denotes the laboratory X-ray source.

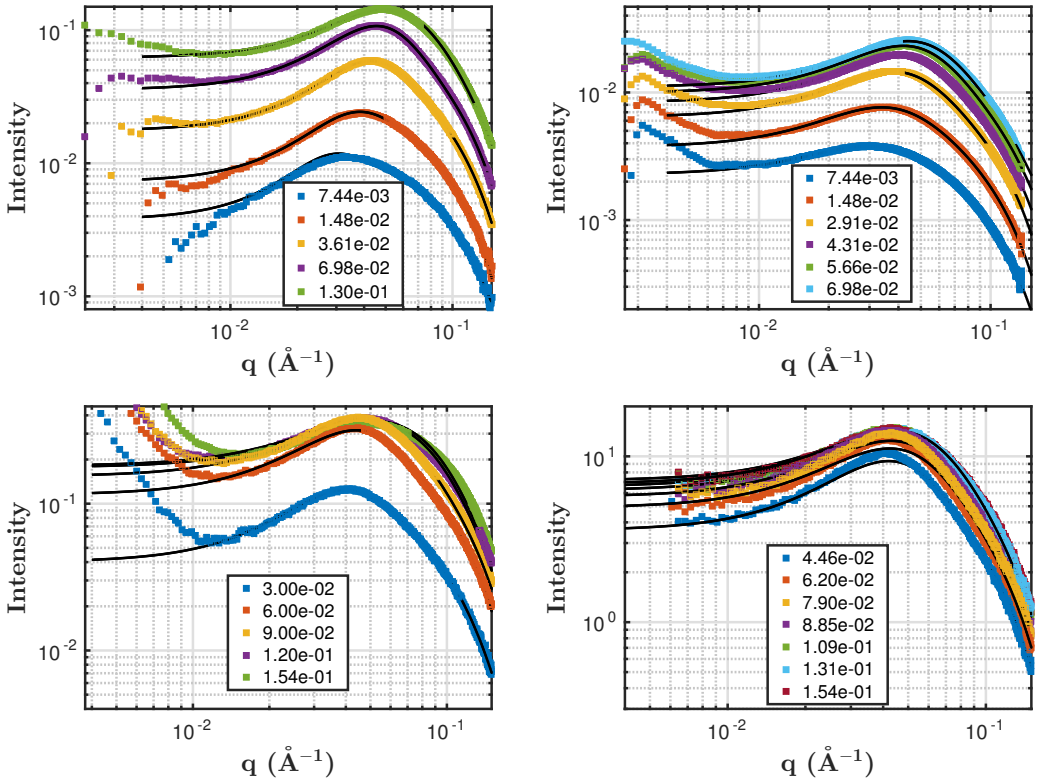

Figure 11.7: *Screened Coulomb fits (black lines). From left to right, top to bottom: SC3139_RT, SC3274, SC3858, inh_201608.*

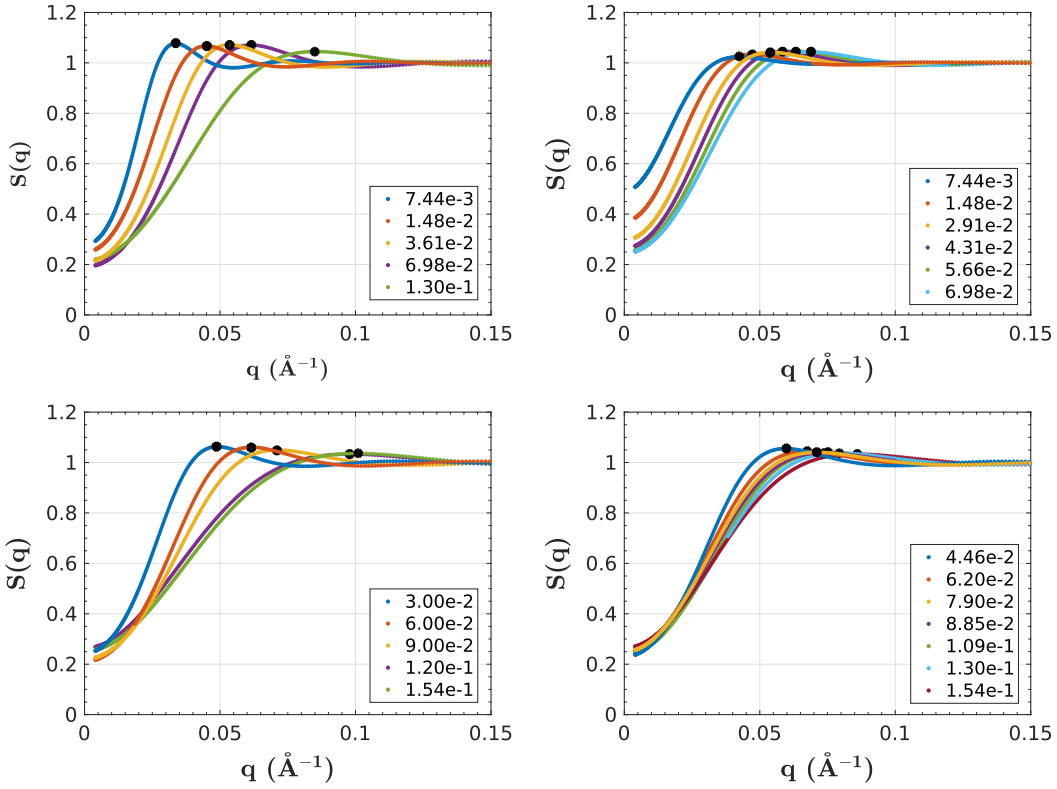

Figure 11.8: *Screened Coulomb structure factors. From left to right, top to bottom: SC3139_RT, SC3274, SC3858, inh_201608. The peak positions are marked by black circles.*

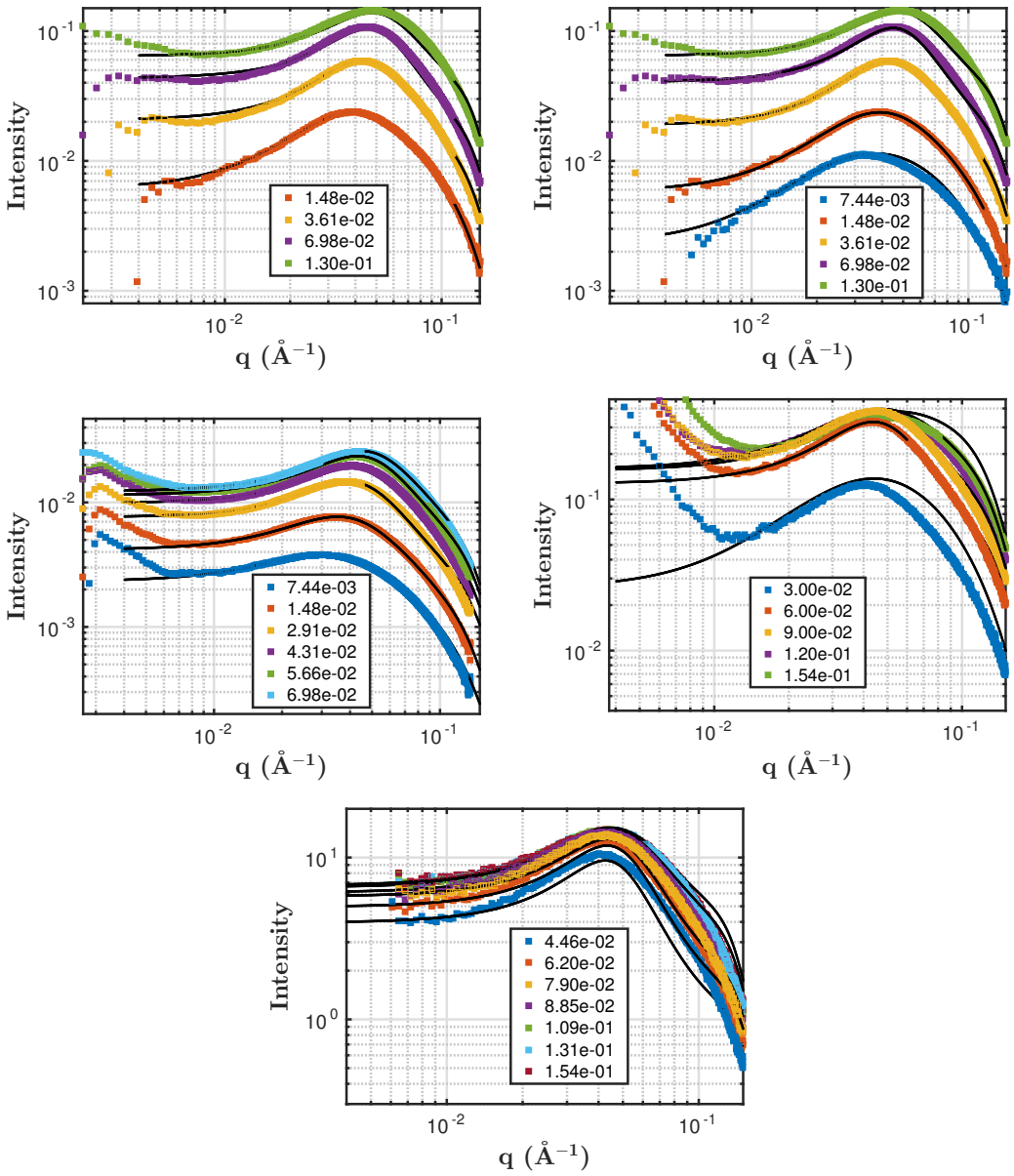

Figure 11.9: *Two-Yukawa fits (black lines). From left to right, top to bottom: SC3139_lowT, SC3139_RT, SC3274, SC3858, inh_201608.*

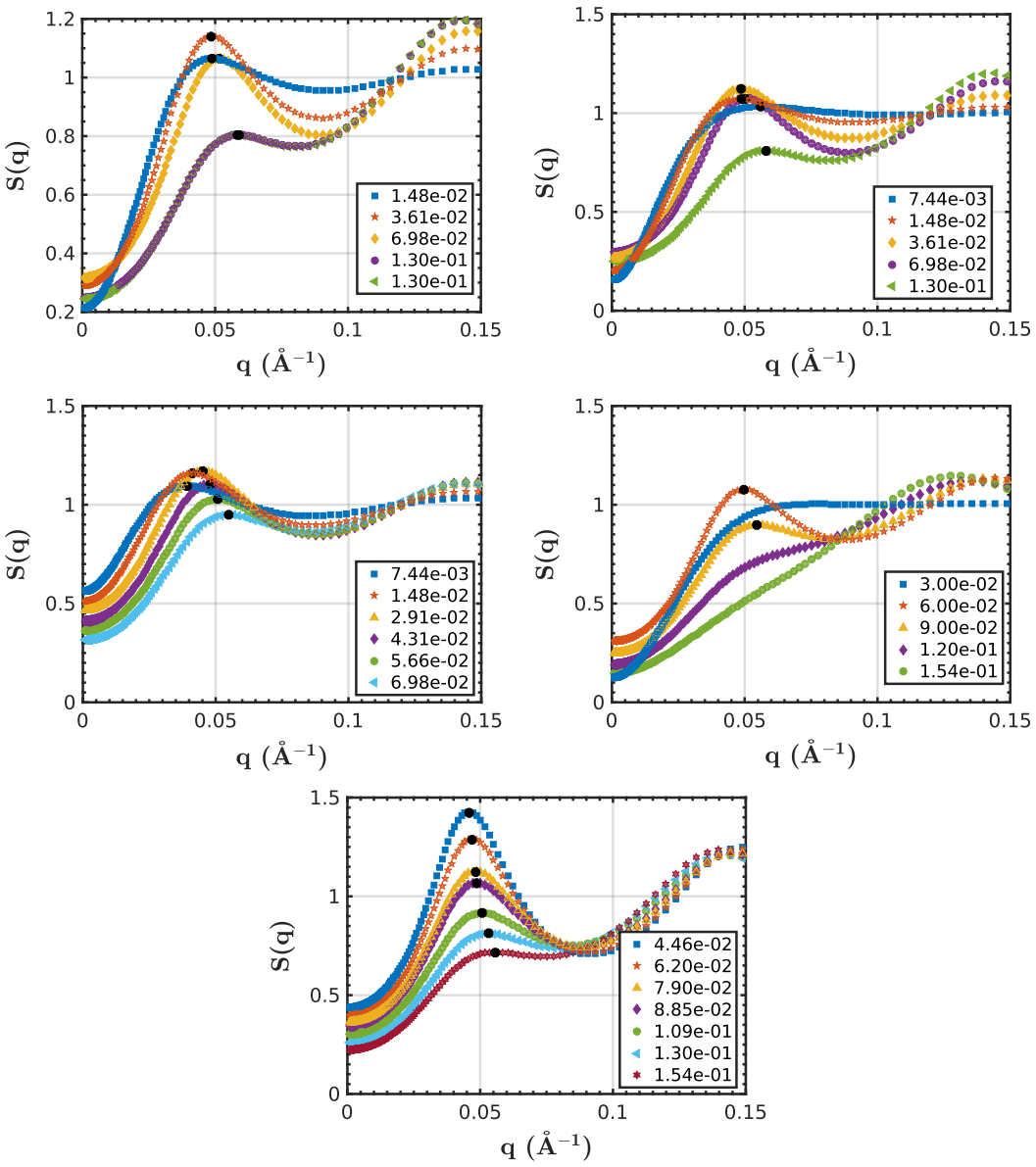

Figure 11.10: *Two-Yukawa structure factors. From left to right, top to bottom: SC3139_lowT, SC3139_RT, SC3274, SC3858, inh_201608. The peak positions are marked by black circles.*

11.6 Values of the fit parameters for the available BLG data sets from different beamtimes

In this section the fit parameters for the BLG data are listed. The data together with the fits is shown in the previous section. During beamtime SC3139 BLG samples were measured both at low temperature (8 and 10 °C) and at room temperature. There was no difference. The room temperature data was fitted with both the SC and the Two-Yukawa (2Y) potential. The low temperature data was only fitted with the 2Y potential.

11.6.1 SC potential

Table 11.3: *Fit parameters for SC potential fitted to RT data from beamtime SC3139 at ID02. Fixed parameters or parameters that ended in one of the given borders are written in blue. The salt is monovalent.*

c_p (mg/ml)	10	20	50	100	200
Temperature	RT	RT	RT	RT	RT
Vol. frac. calc.	7.44e-03	1.48e-02	3.61e-02	6.98e-02	1.30e-01
Vol. frac. fit	3.30e-03	7.78e-03	1.83e-02	3.49e-02	6.02e-02
R_a(Å)	39	39	46.77	54.22	47.13
R_b(Å)	19	19	19	19	19
ρ_{ell}(Å^{-2})	1.19e-05	1.19e-05	1.19e-05	1.19e-05	1.19e-05
ρ_{solv}(Å^{-2})	1.27e-05	1.27e-05	1.27e-05	1.27e-05	1.27e-05
Charge (e)	23.46	14.37	11.71	9.80	6.15
Salt (mM)	3.00	3.00	3.00	3.00	3.00
T (K)	298	298	298	298	298
ϵ	78	78	78	78	78
incoh. bkg.	3.06e-04	-3.98e-05	3.04e-04	7.69e-04	3.25e-03

Table 11.4: *Fit parameters for SC potential fitted to data from beamtime SC3274 at ID02. Fixed parameters or parameters that ended in one of the given borders are written in blue. The salt is monovalent.*

c_p (mg/ml)	10	20	40	60	80	100
Vol. frac. calc.	7.44e-03	1.48e-02	2.91e-02	4.31e-02	5.66e-02	6.98e-02
Vol. frac. fit	4.13e-03	8.47e-03	1.68e-02	2.34e-02	2.94e-02	3.42e-02
R_a(Å)	46.28	49.18	53.14	54.32	53.35	50.93
R_b(Å)	19	19	19	19	19	19
ρ_{ell}(Å^{-2})	1.19e-05	1.19e-05	1.19e-05	1.19e-05	1.19e-05	1.19e-05
ρ_{solv}(Å^{-2})	1.15e-05	1.15e-05	1.15e-05	1.15e-05	1.15e-05	1.15e-05
Charge (e)	11.22	10.47	9.37	8.78	8.13	7.45
Salt (mM)	3.00	3.00	3.00	3.00	3.00	3.00
T (K)	298	298	298	298	298	298
ϵ	78	78	78	78	78	78
incoh. bkg.	7.68e-06	-2.45e-06	3.75e-05	1.90e-04	4.59e-01	7.51e-04

Table 11.5: *Fit parameters for SC potential fitted to data from beamtime SC3858 at ID02. Fixed parameters or parameters that ended in one of the given borders are written in blue. The salt is monovalent.*

c_p (mg/ml)	40	80	120	160	204.86
Vol. frac. calc.	3.00e-02	6.00e-02	9.00e-02	1.20e-01	1.54e-01
Vol. frac. fit	1.22e-02	3.32e-02	4.39e-02	5.53e-02	5.87e-02
R_a(Å)	45.07	55	52.88	40.97	39
R_b(Å)	19	19	19	19	19
ρ_{ell}(Å^{-2})	1.19e-05	1.19e-05	1.19e-05	1.19e-05	1.19e-05
ρ_{solv}(Å^{-2})	1.05e-05	1.05e-05	1.05e-05	1.05e-05	1.05e-05
Charge (e)	12.35	9.18	7.44	4.83	4.79
Salt (mM)	3.00	3.00	3.00	3.00	3.00
T (K)	298	298	298	298	298
ϵ	78	78	78	78	78
incoh. bkg.	3.70e-04	7.65e-04	2.74e-03	4.56e-03	6.22e-03

Table 11.6: *Fit parameters for SC potential fitted to data from inhouse measurement 2016-08. Fixed parameters or parameters that ended in one of the given borders are written in blue. The Salt is monovalent.*

c_p (mg/ml)	76	110	140	161	200	250	300
Vol. frac. calc.	4.46e-02	6.20e-02	7.90e-02	8.85e-02	1.09e-01	1.30e-01	1.54e-01
Vol. frac. fit	2.82e-02	3.56e-02	4.14e-02	4.49e-02	4.94e-02	5.18e-02	5.31e-02
R_a(Å)	55	55	55	55	55	52.97	50.22
R_b(Å)	19	19	19	19	19	19	19
ρ_{ell}(Å^{-2})	1.19e-05	1.19e-05	1.19e-05	1.19e-05	1.19e-05	1.19e-05	1.19e-05
ρ_{solv}(Å^{-2})	2.00e-05	2.00e-05	2.00e-05	2.00e-05	2.00e-05	2.00e-05	2.00e-05
Charge (e)	9.21	7.51	6.93	6.61	6.61	6.14	5.47
Salt (mM)	3.00	3.00	3.00	3.00	3.00	3.00	3.00
T (K)	298	298	298	298	298	298	298
ϵ	78	78	78	78	78	78	78
incoh. bkg.	3.99e-02	6.23e-02	8.06e-02	1.03e-01	1.51e-01	1.61e-01	1.74e-01

11.6.2 2Y potential

Table 11.7: *Fit parameters for 2Y potential fitted to low temperature data from beamtime SC3139 at ID02. Fixed parameters or parameters that ended in one of the given borders are written in blue.*

c_p (mg/ml)	20	50	100	200	200
Temperature	8	8	10	10	20
Vol. frac. calc.	1.48e-02	3.61e-02	6.98e-02	1.30e-01	1.30e-01
Vol. frac. fit	1.48e-02	3.61e-02	6.98e-02	1.30e-01	1.30e-01
R_a(Å)	37.6	37.6	37.6	37.6	37.6
R_b(Å)	19.2	19.2	19.2	19.2	19.2
ρ_{ell}(Å^{-2})	1.19e-05	1.19e-05	1.19e-05	1.19e-05	1.19e-05
ρ_{solv}(Å^{-2})	1.13e-05	1.13e-05	1.13e-05	1.13e-05	1.13e-05
K_1	9.45	13.11	11.62	6.64	6.51
Z_1	10.00	10.00	10.00	10.00	10.00
K_2	-3.36	-3.59	-3.51	-1.99	-1.90
Z_2	0.73	1.55	2.32	2.30	2.20
incoh. bkg.	1.00e-04	3.93e-04	8.01e-04	1.54e-03	1.42e-03

Table 11.8: *Fit parameters for 2Y potential fitted to RT data from beamtime SC3139 at ID02. Fixed parameters or parameters that ended in one of the given borders are written in blue.*

c_p (mg/ml)	10	20	50	100	200
Vol. frac. calc.	7.44e-03	1.48e-02	3.61e-02	6.98e-02	1.30e-01
Vol. frac. fit	7.44e-03	1.48e-02	3.61e-02	6.98e-02	1.30e-01
R_a(Å)	37.6	37.6	37.6	37.6	37.6
R_b(Å)	19.2	19.2	19.2	19.2	19.2
ρ_{ell}(Å^{-2})	1.19e-05	1.19e-05	1.19e-05	1.19e-05	1.19e-05
ρ_{solv}(Å^{-2})	1.13e-05	1.13e-05	1.13e-05	1.13e-05	1.13e-05
K_1	4.00	9.97	11.81	11.18	6.83
Z_1	10.00	10.00	10.00	10.00	10.00
K_2	-4.20	-3.47	-3.27	-3.17	-2.02
Z_2	0.45	0.71	1.40	2.10	2.30
incoh. bkg.	1.00e-04	1.00e-04	1.60e-04	4.29e-04	1.60e-03

Table 11.9: *Fit parameters for 2Y potential fitted to data from beamtime SC3274 at ID02. Fixed parameters or parameters that ended in one of the given borders are written in blue.*

c_p (mg/ml)	10	20	40	60	80	100
Vol. frac. calc.	7.44e-03	1.48e-02	2.91e-02	4.31e-02	5.66e-02	6.98e-02
Vol. frac. fit	7.44e-03	1.48e-02	2.91e-02	4.31e-02	5.66e-02	6.98e-02
R_a(Å)	37.6	37.6	37.6	37.6	37.6	37.6
R_b(Å)	19.2	19.2	19.2	19.2	19.2	19.2
ρ_{ell}(Å^{-2})	1.19e-05	1.19e-05	1.19e-05	1.19e-05	1.19e-05	1.19e-05
ρ_{solv}(Å^{-2})	1.16e-05	1.16e-05	1.16e-05	1.16e-05	1.16e-05	1.16e-05
K_1	19.28	19.69	17.02	12.56	9.60	7.03
Z_1	10.00	10.00	10.00	10.00	10.00	
K_2	-2.99	-3.62	-3.97	-3.24	-2.66	-2.08
Z_2	0.99	1.39	1.92	2.02	2.03	1.92
incoh. bkg.	4.00e-05	4.00e-05	2.00e-04	2.00e-04	2.00e-04	2.00e-04

Table 11.10: *Fit parameters for 2Y potential fitted to data from beamtime SC3858 at ID02. Fixed parameters or parameters that ended in one of the given borders are written in blue.*

c_p (mg/ml)	40	80	120	160	204.86
Vol. frac. calc.	3.00e-02	6.00e-02	9.00e-02	1.20e-02	1.54e-01
Vol. frac. fit	3.00e-02	6.00e-02	9.00e-02	1.20e-02	1.54e-01
R_a(Å)	37.6	37.6	37.6	37.6	37.6
R_b(Å)	19.2	19.2	19.2	19.2	19.2
ρ_{ell}(Å^{-2})	1.19e-05	1.19e-05	1.19e-05	1.19e-05	1.19e-05
ρ_{solv}(Å^{-2})	1.08e-05	1.08e-05	1.08e-05	1.08e-05	1.08e-05
K_1	1.34	10.75	6.17	3.08	1.68
Z_1	10.00	10.00	10.00	10.00	10.00
K_2	-1.96	-2.90	-1.70	-0.94	-0.67
Z_2	0.58	1.90	1.67	1.29	1.12
incoh. bkg.	1.00e-04	6.65e-04	2.10e-03	3.35e-03	3.62e-03

Table 11.11: *Fit parameters for 2Y potential fitted to data from inhouse measurement 2016-08. Fixed parameters or parameters that ended in one of the given borders are written in blue.*

c_p (mg/ml)	76	110	140	161	200	250	300
Vol. frac. calc.	4.46e-02	6.20e-02	7.90e-02	8.85e-02	1.09e-01	1.30e-01	1.54e-01
Vol. frac. fit	4.46e-02	6.20e-02	7.90e-02	8.85e-02	1.09e-01	1.30e-01	1.54e-01
R_a(Å)	37.6	37.6	37.6	37.6	37.6	37.6	37.6
R_b(Å)	19.2	19.2	19.2	19.2	19.2	19.2	19.2
ρ_{ell}(Å^{-2})	1.19e-05	1.19e-05	1.19e-05	1.19e-05	1.19e-05	1.19e-05	1.19e-05
ρ_{solv}(Å^{-2})	6.10e-06	6.10e-06	6.10e-06	6.10e-06	6.10e-06	6.10e-06	6.10e-06
K_1	29.26	20.15	13.74	11.92	8.23	6.54	5.49
Z_1	10.00	10.00	10.00	10.00	10.00	10.00	10.00
K_2	-8.65	-5.90	-3.86	-3.26	-2.10	-1.60	-1.26
Z_2	2.90	2.80	2.60	2.50	2.20	2.00	1.80
incoh. bkg.	1.53e-01	1.56e-01	1.31e-01	1.42e-01	1.36e-01	6.66e-02	1.00e-02

Chapter 12

Supporting Information for Results Part C

12.1 Transmission measurements

(Time dependent) transmission measurements were used to discuss the multiple scattering for DLS measurements in regime II. The results can also be used to double check the boundary c* and c**. The measurements were performed by Pinelopi Christodoulou.

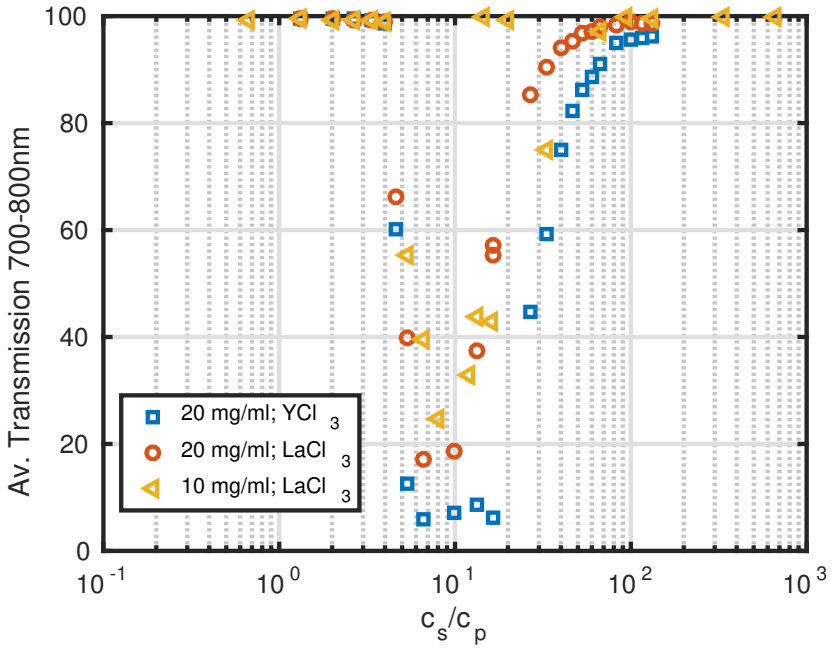

Figure 12.1: *UV-vis transmission of 10 and 20 mg/ml BSA with $LaCl_3$ and 20 mg/ml BSA with YCl_3.*

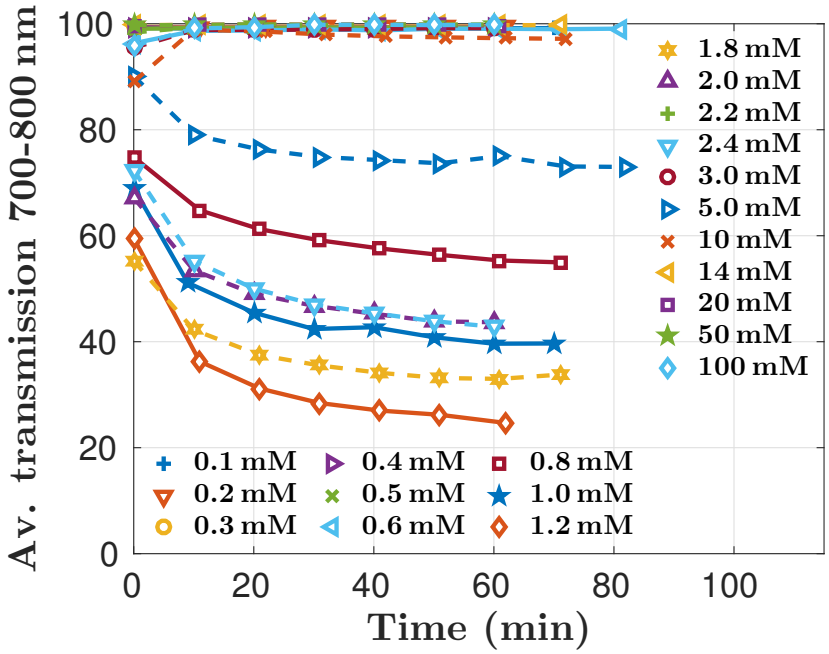

Figure 12.2: *Time dependent UV-vis transmission of 10 mg/ml BSA with different $LaCl_3$ concentrations. The $LaCl_3$ concentrations are given in the legend. The transmission starts to drop at 0.8 mM $LaCl_3$. From 0.1 to 1.2 mM the dataseries are connected by solid lines. At 1.2 mM the transmission reaches a minimum value. Then it increases again. At 14 mM it reaches ∼100% again. Starting from 1.8 mM the dataseries are connected by dashed lines. For an unknown reason, the 2.2 and 3.0 mM dataseries have a transmission close to 100%. The data shows that for the samples in the second regime (low transmission) it took up to 30 min until the final transmission value was reached.*

12.2 Regime II for BSA-$LaCl_3$ in H_2O

Table 12.1: *c^* and c^{**} boundaries for BSA-$LaCl_3$ in H_2O. Use 66.5 kDa as molecular weight of BSA to calculate c^*/c_p and c^{**}/c_p.*

BSA (mg/ml)	c^* (mM) $LaCl_3$	c^{**} (mM) $LaCl_3$	c^*/c_p $LaCl_3$	c^{**}/c_p $LaCl_3$
15	1.1±0.1	4.0±0.4	4.9±0.4	18±1.8
20	1.5±0.1	4.5±0.5	5.0±0.3	15±1.7
25	1.9±0.1	5.5±0.5	5.1±0.3	15±1.3
50	4.0±0.4	9.0±1.0	5.3±0.5	12±1.3
80	7.5±0.5	16.0±2.0	6.2±0.4	13±1.7
100	9.5±0.5	16.5±1.5	6.3±0.3	11±1.0
150	12.5±0.5	32±2.0	5.5±0.2	14±0.89

12.3 Binned collective diffusion coefficients

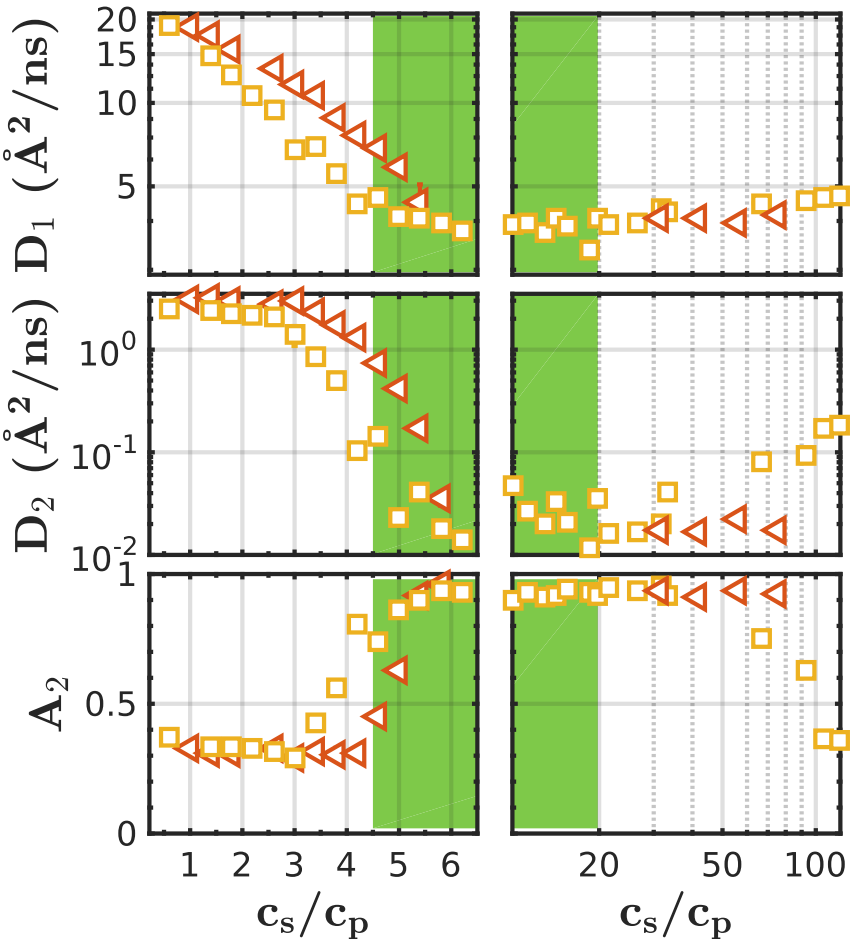

Figure 12.3: *Binned results for collective diffusion coefficients. Red triangles: BSA with YCl_3. Squares: BSA with $LaCl_3$. The BSA-YCl_3 data shown in the left part of the Figure was taken by D. Soraruf[3].*

Chapter 13

Supporting Information for Results Part D

13.1 Further protein stability measurements

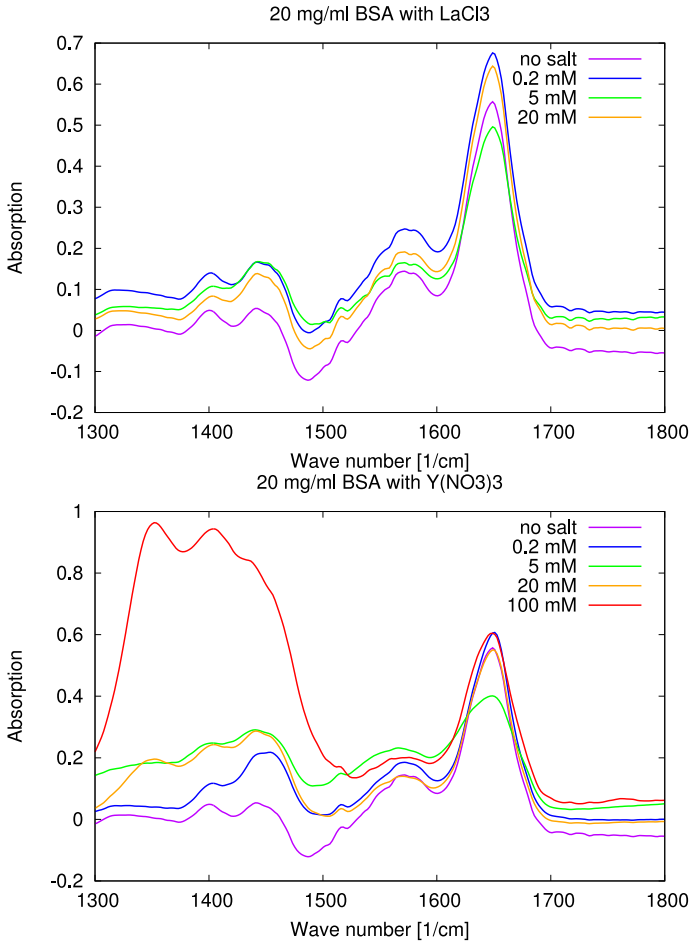

Figure 13.1: *FTIR measurements with different salt concentrations. (a) HSA with $LaCl_3$, (b) BSA with the hydrate salt $Y(NO_3)_3$.*

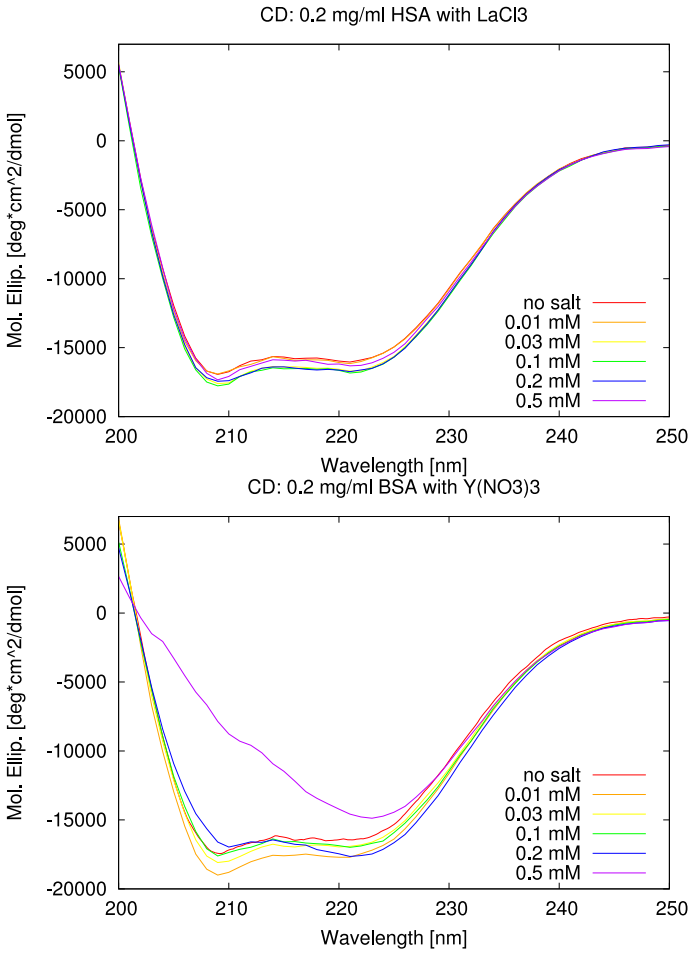

Figure 13.2: *Circular dichroism measurements with different salt concentrations. (a) HSA with $LaCl_3$, (b) BSA with $Y(NO_3)_3$.*

13.2 Values of the fit parameters for the BSA with $La(NO_3)_3$ data

Table 13.1: *Fit parameters for 50 mg/ml BSA with $La(NO_3)_3$. The perturbation parameter ϵ for the SHS potential is given by $\epsilon = \Delta/(\sigma + \Delta)$. See the main text of the paper for further information on the potential. Fixed parameters or parameters that ended in one of the given borders are written in blue.*

c_s (mM)	0	2	4	4.5	5	5.5	6	6.5
Vol. frac.	2.00e-02	2.63e-02	3.56e-02	3.57e-02	3.45e-02	2.96e-02	2.63e-02	2.21e-02
R_a(Å)	18	18	18	18	18	18	18	18
R_b(Å)	38	49	52	52	51	50	51	49
ρ_{ell}(Å^{-2})	1.24e-05	1.24e-05	1.24e-05	1.24e-05	1.24e-05	1.24e-05	1.24e-05	1.24e-05
ρ_{solv}(Å^{-2})	7.68e-06	8.77e-06	8.98e-06	8.98e-06	8.91e-06	8.84e-06	8.91e-06	8.77e-06
Pert. par. ϵ			0.01	0.01	0.01	0.01	0.01	0.01
Stickiness τ			9.29e-02	8.04e-02	7.73e-02	7.34e-02	7.05e-02	6.63e-02
Charge (e)	100	100						
Monov. Salt (mM)	31.3	81.6						
Temp. (K)	298	298						
Dielectric const. ϵ	78	78						
incoh. bkg.	1.22e-02	1.22e-02	1.22e-02	1.22e-02	1.22e-02	1.22e-02	1.22e-02	1.22e-02
u_0 (k_BT)			4.50	4.64	4.68	4.73	4.77	4.83
B_2/B_2^{HS}			-1.69	-2.11	-2.23	-2.41	-2.55	-2.77

Table 13.2: *Fit parameters for 50 mg/ml BSA with $La(NO_3)_3$. The perturbation parameter ϵ for the SHS potential is given by $\epsilon = \Delta/(\sigma + \Delta)$. See the main text of the paper for further information on the potential. Fixed parameters or parameters that ended in one of the given borders are written in blue.*

c_s (mM)	7	8	9	10	11	12	14	16
Vol. frac.	2.10e-02	2.00e-02	2.00e-02	2.03e-02	2.02e-02	2.03e-02	2.10e-02	2.18e-02
R_a(Å)	18	18	18	18	18	18	18	18
R_b(Å)	49	50	51	52	50	50	50	53
ρ_{ell}(Å^{-2})	1.24e-05	1.24e-05	1.24e-05	1.24e-05	1.24e-05	1.24e-05	1.24e-05	1.24e-05
ρ_{solv}(Å^{-2})	8.77e-06	8.84e-06	8.91e-06	8.98e-06	8.84e-06	8.84e-06	8.84e-06	9.05e-06
Pert. par. ϵ	0.01	0.01	0.01	0.01	0.01	0.01	0.01	0.01
Stickiness τ	6.52e-02	6.42e-02	6.45e-02	6.53e-02	6.47e-02	6.47e-02	6.58e-02	7.00e-02
incoh. bkg.	1.22e-02	1.22e-02	1.22e-02	1.22e-02	1.22e-02	1.22e-02	1.22e-02	1.22e-02
u_0 (k_BT)	4.85	4.87	4.86	4.85	4.86	4.86	4.84	4.78
B_2/B_2^{HS}	-2.83	-2.90	-2.88	-2.83	-2.86	-2.86	-2.80	-2.57

Table 13.3: *Fit parameters for 50 mg/ml BSA with $La(NO_3)_3$. The perturbation parameter ϵ for the SHS potential is given by $\epsilon = \Delta/(\sigma + \Delta)$. See the main text of the paper for further information on the potential. Fixed parameters or parameters that ended in one of the given borders are written in blue.*

c_s (mM)	20	24	28	32	40	52
Vol. frac.	2.28e-02	2.28e-02	2.55e-02	2.18e-02	2.19e-02	2.25e-02
R_a(Å)	18	18	18	18	18	18
R_b(Å)	51	52	56	51	52	55
ρ_{ell}(Å^{-2})	1.24e-05	1.24e-05	1.24e-05	1.24e-05	1.24e-05	1.24e-05
ρ_{solv}(Å^{-2})	8.91e-06	8.98e-06	9.23e-06	8.91e-06	8.98e-06	9.17e-06
Pert. par. ϵ	0.01	0.01	0.01	0.01	0.01	0.01
Stickiness τ	6.99e-02	7.24e-02	8.37e-02	7.11e-02	7.37e-02	8.02e-02
incoh. bkg.	1.22e-02	1.22e-02	1.22e-02	1.22e-02	1.22e-02	1.22e-02
u_0 (k_BT)	4.78	4.75	4.60	4.76	4.73	4.64
B_2/B_2^{HS}	-2.58	-2.45	-1.99	-2.51	-2.39	-2.12

List of Figures

List of Tables

Abbreviations

ASP amorphous solid particle

BLG β-lactoglobulin

BSA bovine serum albumin

CD circular dichroism spectroscopy

DLCA diffusion limited cluster aggregation

DLS dynamic light scattering

ESRF European Synchrotron Radiation Facility

FTIR Fourier transform infrared spectroscopy

ILL Institut Laue-Langevin

IRO intermediate range order

ISF intermediate scattering function

LCST lower critical solution temperature

LLPS liquid-liquid phase separation

MC Monte Carlo

MD molecular dynamics

NBS neutron backscattering

NCNR NIST Center for Neutron Research

NIST National Institute of Standards and Technology

NSE neutron spin-echo

PMMA poly(methylmethacrylate)

RC reentrant condensation

RLCA reaction limited cluster aggregation

SALR short-range attractive, long-range repulsive

SAXS small angle X-ray scattering

SC screened Coulombic

SD sample-to-detector

SHS sticky hard sphere

SLS static light scattering

USAXS ultra small angle X-ray scattering

Nomenclature

$\mathbf{c}^{**}$ upper salt concentration boundary of the RC

$\mathbf{c}_p$ protein concentration

$\mathbf{c}_s$ salt concentration

$\mathbf{c}^{*}$ lower salt concentration boundary of the RC

Bibliography

[1] F. Zhang, S. Weggler, M. J. Ziller, L. Ianeselli, B. S. Heck, A. Hildebrandt, O. Kohlbacher, M. W. A. Skoda, R. M. J. Jacobs, and F. Schreiber. Universality of protein reentrant condensation in solution induced by multivalent metal ions. *Proteins*, 78(16):3450–3457, 2010.

[2] F. Zhang, F. Roosen-Runge, A. Sauter, M. Wolf, R. M. J. Jacobs, and F. Schreiber. Reentrant condensation, liquid-liquid phase separation and crystallization in protein solutions induced by multivalent metal ions. *Pure Appl. Chem.*, 86:191–202, 2014.

[3] D. Soraruf, F. Roosen-Runge, M. Grimaldo, F. Zanini, R. Schweins, T. Seydel, F. Zhang, R. Roth, M. Oettel, and F. Schreiber. Protein cluster formation in aqueous solution in the presence of multivalent metal ions - a light scattering study. *Soft Matter*, 10:894–902, 2014.

[4] R. J. Ellis. Macromolecular crowding: Obvious but underappreciated. *Trends Biochem. Sci.*, 26(10):597–604, 2001.

[5] M. Grimaldo, F. Roosen-Runge, M. Hennig, F. Zanini, F. Zhang, M. Zamponi, N. Jalarvo, F. Schreiber, and T. Seydel. Salt-induced universal slowing down of the short-time self-diffusion of a globular protein in aqueous solution. *J. Phys. Chem. Lett.*, 6:2577–2582, 2015.

[6] Y. Saricay, S. K. Dhayal, P. A. Wierenga, and R. de Vries. Protein cluster formation during enzymatic cross-linking of globular proteins. *Faraday Discuss.*, 158:51–63, 2012.

[7] G. P. Petrova, Y. M. Petrusevich, and A. N. Evseevicheva. Molecular clusters in water protein solutions in the presence of heavy metal ions. *Gen. Physiol. Biophys.*, 17:97–104, 1998.

[8] P. Baglioni, E. Fratini, B. Lonetti, and S. H. Chen. Structural arrest in concentrated cytochrome C solutions: the effect of pH and salts. *J. Phys. Cond. Matter*, 16(42):S5003, 2004.

[9] S. Bucciarelli, J. S. Myung, B. Farago, S. Das, G. A. Vliegenthart, O. Holderer, R. G. Winkler, P. Schurtenberger, G. Gompper, and A. Stradner. Dramatic

influence of patchy attractions on short-time protein diffusion under crowded conditions. *Science Advances*, 2:e1601432, 2016.

[10] D. Erdemir, A. Y. Lee, and A. S. Myerson. Nucleation of crystals from solution: Classical and two-step models. *Acc. Chem. Res.*, 42(5):621–629, 2009.

[11] Y. Georgalis, P. Umbach, W. Saenger, B. Ihmels, and D. M. Soumpasis. Ordering of fractal clusters in crystallizing lysozyme solutions. *J. Am. Chem. Soc.*, 121(8):1627–1635, 1999.

[12] M. Sleutel and A. E. S. van Driessche. Role of clusters in nonclassical nucleation and growth of protein crystals. *Proc. Natl. Acad. Sci. U.S.A*, 111(5):E546–E553, 2014.

[13] O. Gliko, N. Neumaier, W. Pan, I. Haase, M. Fischer, A. Bacher, S. Weinkauf, and P. G. Vekilov. A metastable prerequisite for the growth of lumazine synthase crystals. *J. Am. Chem. Soc.*, 127(10):3433–3438, 2005.

[14] O. Gliko, W. Pan, P. Katsonis, N. Neumaier, O. Galkin, S. Weinkauf, and P. G. Vekilov. Metastable liquid clusters in super- and undersaturated protein solutions. *J. Phys. Chem. B*, 111(12):3106–3114, 2007.

[15] T. Yamazaki, Y. Kimura, P. G. Vekilov, E. Furukawa, M. Shirai, H. Matsumoto, A. E. S. Van Driessche, and K. Tsukamoto. Two types of amorphous protein particles facilitate crystal nucleation. *Proc. Natl. Acad. Sci. U.S.A*, 114(9):2154–2159, 2017.

[16] W. Pan, O. Galkin, L. Filobelo, R. L. Nagel, and P. G. Vekilov. Metastable mesoscopic clusters in solutions of sickle-cell hemoglobin. *Biophys. J.*, 92(1):267–277, 2007.

[17] W. Pan, P. G. Vekilov, and V. Lubchenko. Origin of anomalous mesoscopic phases in protein solutions. *J. Phys. Chem. B*, 114(22):7620–7630, 2010.

[18] J. F. Lutsko. Mechanism for the stabilization of protein clusters above the solubility curve: the role of non-ideal chemical reactions. *J. Phys. Cond. Matter*, 28:244020, 2016.

[19] Y. Georgalis, A. Zouni, W. Eberstein, and W. Saenger. Formation dynamics of protein precrystallization fractal clusters. *J. Cryst. Growth*, 126:245–260, 1993.

[20] S. Banjade and M. K. Rosen. Phase transitions of multivalent proteins can promote clustering of membrane receptors. *eLife*, 3:e04123, 2014.

[21] P. Li, S. Banjade, H.-C. Cheng, S. Kim, B. Chen, L. Guo, M. Llaguno, J. V. Hollingsworth, D. S. Kind, S. F. Banani, P. S. Russo, Q.-X. Jiang, B. T. Nixon, and M. K. Rosen. Phase transitions in the assembly of multivalent signalling proteins. *Nature*, 483:336, 2014.

[22] N. Meilhac and N. Destainville. Clusters of proteins in biomembranes: Insights into the roles of interaction potential shapes and of protein diversity. *J. Phys. Chem. B*, 115:7190–7199, 2011.

[23] J. Groenewold and W. K. Kegel. Anomalously large equilibrium clusters of colloids. *J. Phys. Chem. B*, 105(47):11702–11709, 2001.

[24] Y. Liu, W.-R. Chen, and S.-H. Chen. Cluster formation in two-Yukawa fluids. *J. Chem. Phys.*, 122(4):044507, 2005.

[25] A. Imperio and L. Reatto. A bidimensional fluid system with competing interactions: Spontaneous and induced pattern formation. *J. Phys. Cond. Matter*, 16:S3769–S3789, 2004.

[26] S. Mossa, F. Sciortino, P. Tartaglia, and E. Zaccarelli. Ground-state clusters for short-range attractive and long-range repulsive potentials. *Langmuir*, 20(24):10756–10763, 2004.

[27] A. I. Campbell, V. J. Anderson, J. S. van Duijneveldt, and P. Bartlett. Dynamical arrest in attractive colloids: the effect of long-range repulsion. *Phys. Rev. Lett.*, 94:208301, 2005.

[28] R. Sanchez and P. Bartlett. Equilibrium cluster formation and gelation. *J. Phys. Cond. Matter*, 17:S3551–S3556, 2005.

[29] A. D. Dinsmore and D. A. Weitz. Direct imaging of three-dimensional structure and topology of colloidal gels. *J. Phys. Cond. Matter*, 14:7581–7597, 2002.

[30] F. Carlsson, M. Malmsten, and P. Linse. Protein-polyelectrolyte cluster formation and redissolution: a monte carlo study. *J. Am. Chem. Soc.*, 125:3140–3149, 2003.

[31] A. Stradner, H. Sedgwick, F. Cardinaux, W. C. K. Poon, S. U. Egelhaaf, and P. Schurtenberger. Equilibrium cluster formation in concentrated protein solutions and colloids. *Nature*, 432:492–495, 2004.

[32] A. Stradner, F. Cardinaux, and P. Schurtenberger. A small-angle scattering study on equilibrium clusters in lysozyme solutions. *J. Phys. Chem. B*, 110(42):21222–31, 2006.

[33] A. Shukla, E. Mylonas, E. Di Cola, S. Finet, P. Timmins, T. Narayanan, and D. I. Svergun. Absence of equilibrium cluster phase in concentrated lysozyme solutions. *Proc. Natl. Acad. Sci. U.S.A*, 105(13):5075–5080, 2008.

[34] L. Porcar, P. Falus, W.-R. Chen, A. Faraone, E. Fratini, K. Hong, P. Baglioni, and Y. Liu. Formation of the dynamic clusters in concentrated lysozyme protein solutions. *J. Phys. Chem. Lett.*, 1(1):126–129, 2010.

[35] Y. Liu, L. Porcar, J. Chen, W.-R. Chen, P. Falus, A. Faraone, E. Fratini, K. Hong, and P. Baglioni. Lysozyme protein solution with an intermediate range order structure. *J. Phys. Chem. B*, 115(22):7238–7247, 2011.

[36] P. D. Godfrin, R. Castañeda Priego, Y. Liu, and N. J. Wagner. Intermediate range order and structure in colloidal dispersions with competing interactions. *J. Chem. Phys.*, 139:154904, 2013.

[37] A. Fierro, T. Abete, A. Coniglio, and A. de Candia. Clusters in colloidal systems. *J. Phys. Chem. B*, 115(22):7281–7287, 2011.

[38] F. Carlsson, M. Malmsten, and P. Linse. Monte carlo simulations of lysozyme self-association in aqueous solution. *J. Phys. Chem. B*, 105:12189–12195, 2001.

[39] F. Cardinaux, A. Stradner, P. Schurtenberger, F. Sciortino, and E. Zaccarelli. Modeling equilibrium clusters in lysozyme solutions. *Europhys. Lett.*, 77:48004, 2007.

[40] F. Cardinaux, E. Zaccarelli, A. Stradner, S. Bucciarelli, B. Farago, S. U. Egelhaaf, F. Sciortino, and P. Schurtenberger. Cluster-driven dynamical arrest in concentrated lysozyme solutions. *J. Phys. Chem. B*, 115(22):7227–7237, 2011.

[41] P. Kowalczyk, A. Ciach, P. Gauden, and A. Terzyk. Equilibrium clusters in concentrated lysozyme protein solutions. *J. Colloid Interface Sci.*, 363(2):579–584, 2011.

[42] P. D. Godfrin, N. E. Valadez-Pérez, R. Castañeda Priego, N. J. Wagner, and Y. Liu. Generalized phase behavior of cluster formation in colloidal dispersions with competing interactions. *Soft Matter*, 10:5061, 2014.

[43] J. A. Bollinger and T. M. Truskett. Fluids with competing interactions. I. Decoding the structure factor to detect and characterize self-limited clustering. *J. Chem. Phys.*, 145:064902, 2016.

[44] J. A. Bollinger and T. M. Truskett. Fluids with competing interactions. II. Validating a free energy model for equilibrium cluster size. *J. Chem. Phys.*, 145:064903, 2016.

[45] O. Matsarskaia, M. K. Braun, F. Roosen-Runge, M. Wolf, F. Zhang, R. Roth, and F. Schreiber. Cation-induced hydration effects cause lower critical solution temperature behavior in protein solutions. *J. Phys. Chem. B*, 120(31):7731–7736, 2016.

[46] F. Roosen-Runge, F. Zhang, F. Schreiber, and R. Roth. Ion-activated attractive patches as a mechanism for controlled protein interactions. *Sci. Rep.*, 4:7016, 2014.

[47] F. Zhang, G. Zocher, A. Sauter, T. Stehle, and F. Schreiber. Novel approach to controlled protein crystallization through ligandation of yttrium cations. *J. Appl. Crystallogr.*, 44(4):755–762, 2011.

[48] F. Zhang, R. Roth, M. Wolf, F. Roosen-Runge, M. W. A. Skoda, R. M. J. Jacobs, M. Sztucki, and F. Schreiber. Charge-controlled metastable liquid-liquid phase separation in protein solutions as a universal pathway towards crystallization. *Soft Matter*, 8:1313–1316, 2012.

[49] P. Lindner and T. Zemb. *Neutrons, X-rays, and Light: Scattering Methods Applied to Soft Condensed Matter*. Elsevier North-Holland, 2002.

[50] J. Als-Nielsen and D. McMorrow. *Elements of Modern X-Ray Physics*. John Wiley & Sons, West Sussex, United Kingdom, 2011.

[51] NIST Center for Neutron Research. *SANS Model Function Documentation*, 2010.

[52] G. Nägele. *The Physics of Colloidal Soft Matter*. Institute of Fundamental Technological Research, Warsaw, Poland, 2004.

[53] Wikipedia. Ornstein-Zernike equation. https://en.wikipedia.org/wiki/ornstein-zernike_equation, December 21st, 2017.

[54] J.-P. Hansen and J. B. Hayter. A rescaled MSA structure factor for dilute charged colloidal dispersions. *Mol. Phys.*, 46(3):651–656, 1982.

[55] J. B. Hayter and J. Penfold. An analytic structure factor for macroion solutions. *Mol. Phys.*, 42(1):109–118, 1981.

[56] R. J. Baxter. Percus–Yevick equation for hard spheres with surface adhesion. *J. Chem. Phys.*, 49(6):2770–2774, 1968.

[57] S. V. G. Menon, C. Manohar, and K. S. Rao. A new interpretation of the sticky hard sphere model. *J. Chem. Phys.*, 95(12):9186–9190, 1991.

[58] B. J. Berne and R. Pecora. *Dynamic Light Scattering*. Dover Publications Inc., 2000.

[59] W. Demtröder. *Experimentalphysik 2 - Elektrizität und Optik*. Springer, 2006.

[60] M. Bée. *Quasielastic Neutron Scattering*. Adam Hilger, Bristol, 1988.

[61] F. Mezei. *Neutron Spin Echo Spectroscopy: Basics, Trends, and Applications*, chapter Fundamentals of Neutron Spin Echo Spectroscopy, pages 5–14. Springer Verlag, 2003.

[62] A. Bujacz. Structures of bovine, equine and leporine serum albumin. *Acta Crystallogr.*, D68(10):1278–1289, 2012.

[63] S. Brownlow, J. H. M. Cabral, R. Cooper, D. R. Flower, S. J. Yewdall, I. Polikarpov, A. C. T. North, and L. Sawyer. Bovine β-lactoglobulin at 1.8 Å resolution - still an enigmatic lipocalin. *Structure*, 5(4):481–495, 1997.

[64] G. Kontopidis, C. Holt, and L. Sawyer. Invited review: β-lactoglobulin: Binding properties, structure, and function. *Journal of Dairy Science*, 87:785–796, 2004.

[65] A. L. Lehninger, D. L. Nelson, and M. M. Cox. *Lehninger Biochemie*. Berlin; Heidelberg: Springer, 4th edition, 2009.

[66] H. A. Sober. *CRC Handbook of Biochemistry: Selected data for molecular biology*. The Chemical Rubber Co. Cleveland, Ohio, 1970.

[67] M. Hesse, H. Meier, and B. Zeeh. *Spektroskopische Methoden in der organischen Chemie*. Thieme, 2005.

[68] European Synchrotron Radiation Facility, Grenoble, France. ID02 beamline layout. http://www.esrf.eu/home/usersandscience/experiments/cbs/id02/-beamlinelayout.html, September 25th, 2017.

[69] T. Narayanan, O. Diat, and P. Bösecke. SAXS and USAXS on the high brilliance beamline at the ESRF. *Nucl. Instrum. Methods*, A467-A468:1005–1009, 2001.

[70] Xenocs SAS, 38360 Sassenage, France. http://www.xenocs.com/en/solutions-/xeuss-saxs-waxs-laboratory-beamline/#gallery, December 14th, 2017.

[71] *Xeuss 2.0 Operation Manual*. XENOCS SA, 19 rue François Blumet, 38360 Sassenage, France, 2015.

[72] *GeniX^{3D} - Installation and operation manual*. XENOCS SA, 19 rue François Blumet, 38360 Sassenage, France, 2014.

[73] *ALV-Technical Documentation*. ALV-GmbH, Siemensstraße 4, 63225 Langen, Germany, 2007.

[74] Institut Laue-Langevin, Grenoble, France. IN16B instrument layout. https://www.ill.eu/instruments-support/instruments-groups/instruments-/in16b/description/instrument-layout/, September 27th, 2017.

[75] Institut Laue-Langevin, Grenoble, France. IN15 instrument layout. https://www.ill.eu/instruments-support/instruments-groups/instruments-/in15/description/instrument-layout/, October 4th, 2017.

[76] P. Schleger, B. Alefeld, J. Barthelemy, G. Ehlers, B. Farago, P. Giraud, C. Hayes, A. Kollmar, C. Lartigue, F. Mezei, and D. Richter. The long-wavelength neutron spin-echo spectrometer IN15 at the Institut Laue-Langevin. *Physica B: Condensed Matter*, 241:164 – 165, 1998.

[77] P. Schleger, G. Ehlers, A. Kollmar, B. Alefeld, J. F. Barthelemy, H. Casalta, B. Farago, P. Giraud, C. Hayes, C. Lartigue, F. Mezei, and D. Richter. The sub-neV resolution NSE spectrometer IN15 at the Institue Laue-Langevin. *Physica B: Condensed Matter*, 266:49 – 55, 1999.

[78] C. A. Dreiss, K. S. Jack, and A. P. Parker. On the absolute calibration of bench-top small-angle x-ray scattering instruments: a comparison of different standard methods. *J. Appl. Crystallogr.*, 39:32–38, 2006.

[79] A. Sauter, M. Oelker, G. Zocher, F. Zhang, T. Stehle, and F. Schreiber. Nonclassical pathways of protein crystallization in the presence of multivalent metal ions. *Crystal Growth & Design*, 14(12):6357–6366, 2014.

[80] S. R. Kline. Reduction and analysis of SANS and USANS data using IGOR Pro. *J. Appl. Crystallogr.*, 39(6):895–900, 2006.

[81] M. Grimaldo, F. Roosen-Runge, N. Jalarvo, M. Zamponi, F. Zanini, M. Hennig, F. Zhang, F. Schreiber, and T. Seydel. High-resolution neutron spectroscopy on protein solution samples. *EPJ Web of Conferences*, 83:02005, 2015.

[82] J. Gunton, A. Shiryayev, and D. Pagan. *Protein Condensation: Kinetic Pathways to Crystallization and Disease*. Cambridge University Press, 2007.

[83] S. D. Durbin and G. Feher. Protein crystallization. *Annu. Rev. Phys. Chem.*, 47(1):171–204, 1996.

[84] P. G. Vekilov. Dense liquid precursor for the nucleation of ordered solid phases from solution. *Crystal Growth & Design*, 4(4):671–685, 2004.

[85] R. Piazza. Interactions and phase transitions in protein solutions. *Curr. Opin. Colloid Interface Sci.*, 5(1-2):38–43, 2000.

[86] R. P. Sear. Interactions in protein solutions. *Curr. Opin. Colloid Interface Sci.*, 11(1):35–39, 2006.

[87] M. Muschol and F. Rosenberger. Liquid–liquid phase separation in supersaturated lysozyme solutions and associated precipitate formation/crystallization. *J. Chem. Phys.*, 107(6):1953–1962, 1997.

[88] O. Annunziata, O. Ogun, and G. B. Benedek. Observation of liquid–liquid phase separation for eye lens γS-crystallin. *Proc. Natl. Acad. Sci. U.S.A.*, 100(3):970–974, 2003.

[89] N. R. Asherie. Protein crystallization and phase diagrams. *Methods*, 34(3):266–272, 2004.

[90] O. Galkin, K. Chen, R. L. Nagel, R. E. Hirsch, and P. G. Vekilov. Liquid–liquid separation in solutions of normal and sickle cell hemoglobin. *Proc. Natl. Acad. Sci. U.S.A.*, 99(13):8479–8483, 2002.

[91] A. Pande, J. Pande, N. Asherie, A. Lomakin, O. Ogun, J. King, and G. B. Benedek. Crystal cataracts: Human genetic cataract caused by protein crystallization. *Proc. Natl. Acad. Sci. U.S.A.*, 98(11):6116–6120, 2001.

[92] Y. Wang, A. Lomakin, J. J. McManus, O. Ogun, and G. B. Benedek. Phase behavior of mixtures of human lens proteins gamma D and beta B1. *Proc. Natl. Acad. Sci. U.S.A*, 107(30):13282–13287, 2010.

[93] J. F. Lutsko and G. Nicolis. Theoretical evidence for a dense fluid precursor to crystallization. *Phys. Rev. Lett.*, 96:046102, 2006.

[94] P. R. ten Wolde and D. Frenkel. Enhancement of protein crystal nucleation by critical density fluctuations. *Science*, 277(5334):1975–1978, 1997.

[95] R. Piazza. Protein interactions and association: an open challenge for colloid science. *Curr. Opin. Colloid Interface Sci.*, 8(6):515–522, 2004.

[96] R. A. Curtis, H. W. Blanch, and J. M. Prausnitz. Calculation of phase diagrams for aqueous protein solutions. *J. Phys. Chem. B*, 105(12):2445–2452, 2001.

[97] R. A. Curtis, J. M. Prausnitz, and H. W. Blanch. Protein–protein and protein–salt interactions in aqueous protein solutions containing concentrated electrolytes. *Biotechnol. Bioeng.*, 57(1):11–21, 1998.

[98] K. D. Collins. Ions from the Hofmeister series and osmolytes: Effects on proteins in solution and in the crystallization process. *Methods*, 34(3):300–311, 2004.

[99] D. Rosenbaum, P. Zamora, and C. Zukoski. Phase behavior of small attractive colloidal particles. *Phys. Rev. Lett.*, 76(1):150–153, 1996.

[100] M. Muschol and F. Rosenberger. Interactions in undersaturated and supersaturated lysozyme solutions: Static and dynamic light scattering results. *J. Chem. Phys*, 103:10424, 1995.

[101] A. Tardieu, A. Le Verge, M. Malfois, F. Bonneté, S. Finet, M. Riès-Kautt, and L. Belloni. Proteins in solution: from X-ray scattering intensities to interaction potentials. *J. Cryst. Growth*, 196(2–4):193–203, 1999.

[102] O. D. Velev, E. W. Kaler, and A. M. Lenhoff. Protein interactions in solution characterized by light and neutron scattering: Comparison of lysozyme and chymotrypsinogen. *Biophys. J.*, 75(6):2682–2697, December 1998.

[103] J. A. Thomson, P. Schurtenberger, G. M. Thurston, and G. B. Benedek. Binary liquid phase separation and critical phenomena in a protein/water solution. *Proc. Natl. Acad. Sci. U.S.A*, 84(20):7079–7083, 1987.

[104] Y. Liu, E. Fratini, P. Baglioni, W.-R. Chen, and S.-H. Chen. Effective long-range attraction between protein molecules in solutions studied by small angle neutron scattering. *Phys. Rev. Lett.*, 95:118102, 2005.

[105] M. H. J. Hagen and D. Frenkel. Determination of phase diagrams for the hard-core attractive Yukawa system. *J. Chem. Phys.*, 101(5):4093–4097, 1994.

[106] N. R. Asherie, A. Lomakin, and G. B. Benedek. Phase diagram of colloidal solutions. *Phys. Rev. Lett.*, 77(23):4832–4835, 1996.

[107] M. G. Noro and D. Frenkel. Extended corresponding-states behavior for particles with variable range attractions. *J. Chem. Phys.*, 113(8):2941–2944, 2000.

[108] F. Platten, J. Hansen, D. Wagner, and S. U. Egelhaaf. Second virial coefficient as determined from protein phase behavior. *J. Phys. Chem. Lett.*, 7:4008–4014, 2016.

[109] C. Gripon, L. Legrand, I. Rosenman, O. Vidal, M. C. Robert, and F. Boué. Lysozyme solubility in H_2O and D_2O solutions: a simple relationship. *J. Cryst. Growth*, 177:238–247, 1997.

[110] S. Bucciarelli, N. Mahmoudi, L. Casal-Dujat, M. Jhannin, C. Jud, and A. Stradner. Extended law of corresponding states applied to solvent isotope effect on a globular protein. *J. Phys. Chem. Lett.*, 7:1610–1615, 2016.

[111] Y. M. Efimova, S. Haemers, B. Wierczinski, W. Norde, and A. A. V. Well. Stability of globular proteins in H_2O and D_2O. *Biopolymers*, 85(3):264–273, 2006.

[112] M. J. Parker, C. E. Dempsey, M. Lorch, and A. R. Clarke. Acquisition of native β-strand topology during the rapid collapse phase of protein folding. *Biochemistry*, 36:13396–13405, 1997.

[113] L. Fu, S. Villette, S. Petoud, F. Fernandez-Alonso, and M.-L. Saboungi. H/D isotope effects in protein thermal denaturation: the case of bovine serum albumin. *J. Phys. Chem. B*, 115:1881–1888, 2011.

[114] L. C. Antonino, R. A. Kautz, N. Takayuki, R. O. Fox, and A. L. Fink. Cold denaturation and ^2H_2O stabilization of a staphylococcal nuclease mutant. *Proc. Natl. Acad. Sci. U.S.A.*, 88:7715–7718, 1991.

[115] B. M. P. Huyghues-Despointes, J. M. Scholtz, and C. N. Pace. Protein conformational stabilities can be determined from hydrogen exchange rates. *Nature Struct. Biol.*, 6(10):910–912, October 1999.

[116] Y. Cho, L. B. Sagle, S. Iimura, Y. Zhang, J. Kherb, A. Chilkoti, J. M. Scholtz, and P. S. Cremer. Hydrogen bonding of β-turn structure is stabilized in D_2O. *J. Am. Chem. Soc.*, 131(42):15188–15193, 2009.

[117] M. Jasnin, M. Moulin, M. Haertlein, G. Zaccai, and M. Tehei. In vivo measurement of internal and global macromolecular motions in Escherichia coli. *Biophys. J.*, 95(2):857–864, 2008.

[118] C. Gripon, L. Legrand, I. Rosenman, O. Vidal, M. C. Robert, and F. Boué. Lysozyme-lysozyme interactions in under- and super-saturated solutions: a simple relation between the second virial coefficients in H_2O and D_2O. *J. Cryst. Growth*, 178:575–584, 1997.

[119] I. Broutin, M. Riès-Kautt, and A. Ducruix. Lysozyme solubility in h_2o and d_2o solutions as a function of sodium cholride concentration. *J. Appl. Crystallogr.*, 28:614–617, 1995.

[120] F. Platten, N. E. Valadez-Pérez, R. Castañeda Priego, and S. U. Egelhaaf. Extended law of corresponding states for protein solutions. *J. Chem. Phys.*, 142:174905, 2015.

[121] F. Zhang, M. W. A. Skoda, R. M. J. Jacobs, S. Zorn, R. A. Martin, C. M. Martin, G. F. Clark, S. Weggler, A. Hildebrandt, O. Kohlbacher, and F. Schreiber. Reentrant condensation of proteins in solution induced by multivalent counterions. *Phys. Rev. Lett.*, 101(14):148101, 2008.

[122] F. Roosen-Runge, B. S. Heck, F. Zhang, O. Kohlbacher, and F. Schreiber. Interplay of pH and binding of multivalent metal ions: Charge inversion and reentrant condensation in protein solutions. *J. Phys. Chem. B*, 117(18):5777–5787, 2013.

[123] F. Zhang, F. Roosen-Runge, M. W. A. Skoda, R. M. J. Jacobs, M. Wolf, P. Callow, H. Frielinghaus, V. Pipich, S. Prévost, and F. Schreiber. Hydration and interactions in protein solutions containing concentrated electrolytes studied by small-angle scattering. *Phys. Chem. Chem. Phys.*, 14:2483–2493, 2012.

[124] A. Kubíčková, T. Křížek, P. Coufal, M. Vazdar, E. Wernersson, J. Heyda, and P. Jungwirth. Overcharging in biological systems: Reversal of electrophoretic mobility of aqueous polyaspartate by multivalent cations. *Phys. Rev. Lett.*, 108:186101, 2012.

[125] S. Fujihara and R. Akiyama. Attractive interaction between macroanions mediated by multivalent cations in biological fluids. *J. Mol. Liq.*, A200:89–94.

[126] R. Akiyama, T. Yamashita, and S. Fujihara. Hidden peak of radial distribution function and effective attraction between like-charged proteins caused by translational motion of solvent molecules. *J. Mol. Liq.*, A200:72–76.

[127] R. Akiyama and R. Sakata. An integral equation study of reentrant behavior in attractive interactions between like-charged macroions immersed in an electrolyte solution. *J. Phys. Soc. Jpn.*, 80(12):123602, 2011.

[128] E. Jordan, F. Roosen-Runge, S. Leibfarth, F. Zhang, M. Sztucki, A. Hildebrandt, O. Kohlbacher, and F. Schreiber. Competing salt effects on phase behavior of protein solutions: Tailoring of protein interaction by the binding of multivalent ions and charge screening. *J. Phys. Chem. B*, 118(38):11365–11374, 2014.

[129] T. Narayanan. *Soft Matter Characterization*, chapter 17: Synchroton Small-Angle X-Ray Scattering. Springer New York, 2008.

[130] L. Ianeselli, F. Zhang, M. W. A. Skoda, R. M. J. Jacobs, R. A. Martin, S. Callow, S. Prévost, and F. Schreiber. Protein-protein interactions in ovalbumin solutions studied by small-angle scattering: Effect of ionic strength and the chemical nature of cations. *J. Phys. Chem. B*, 114(11):3776–3783, 2010.

[131] G. A. Vliegenthart and H. N. W. Lekkerkerker. Predicting the gas–liquid critical point from the second virial coefficient. *J. Chem. Phys.*, 112(12):5364–5369, 2000.

[132] M. Wolf, F. Roosen-Runge, F. Zhang, R. Roth, M. W. A. Skoda, R. M. J. Jacobs, M. Sztucki, and F. Schreiber. Effective interactions in protein–salt solutions approaching liquid–liquid phase separation. *J. Mol. Liq.*, 200:20–27, 2014.

[133] A. Sauter, F. Roosen-Runge, F. Zhang, G. Lotze, R. M. J. Jacobs, and F. Schreiber. Real-time observation of nonclassical protein crystallization kinetics. *J. Am. Chem. Soc.*, 137(4):1485–1491, 2015.

[134] A. K. Soper and C. J. Benmore. Quantum differences between heavy and light water. *Phys. Rev. Lett.*, 101:065502, August 2008.

[135] S. Scheiner and M. Čuma. Relative stability and of hydrogen and deuterium bonds. *J. Am. Chem. Soc.*, 118:1511–1521, 1996.

[136] T. Steiner. The hydrogen bond in the solid state. *Angew. Chem. Int. Ed.*, 41:48–76, 2002.

[137] G. Némethy and H. A. Scheraga. Structure of water and hydrophobic bonding in proteins. IV. The thermodynamic properties of liquid deuterium oxide. *J. Chem. Phys.*, 41(3):680–689, 1964.

[138] P. Kujawa and F. M. Winnik. Volumetric studies of aqueous polymer solutions using pressure perturbation calorimetry: a new look at the temperature-induced phase transition of poly(N-isopropylacrylamide) in water and D_2O. *Macromolecules*, 34(12):4130–4135, 2001.

[139] Y. Zhang, S. Furyk, D. E. Bergbreiter, and P. S. Cremer. Specific ion effects on the water solubility of macromolecules: PNIPAM and the Hofmeister series. *J. Am. Chem. Soc.*, 127(41):14505–14510, 2005.

[140] S. Moelbert and P. De Los Rios. Hydrophobic interaction model for upper and lower critical solution temperatures. *Macromolecules*, 36(15):5845–5853, 2003.

[141] A. D. Dinsmore, P. L. Dubin, and G. M. Grason. Clustering in complex fluids. *J. Phys. Chem. B*, 115:7173–7174, 2011.

[142] K. P. Johnston, J. A. Maynard, T. M. Truskett, A. U. Borwankar, M. A. Miller, B. K. Wilson, A. K. Dinin, T. A. Khan, and K. J. Kaczorowski. Concentrated dispersions of equilibrium protein nanoclusters that reversibly dissociate into active monomers. *ACS Nano*, 6(2):1357–1369, 2012.

[143] S. Bucciarelli, L. Casal-Dujat, C. De Michele, F. Sciortino, J. Dhont, J. Bergenholtz, B. Farago, P. Schurtenberger, and A. Stradner. Unusual dynamics of concentration fluctuations in solutions of weakly attractive globular proteins. *J. Phys. Chem. Lett.*, 6(22):4470–4474, 2015.

[144] P. G. Vekilov. The two-step mechanism of nucleation of crystals in solution. *Nanoscale*, 2:2346–2357, 2010.

[145] S. Barhoum and A. Yethiraj. NMR detection of an equilibrium phase consisting of monomers and clusters in concentrated lysozyme solutions. *J. Phys. Chem. B*, 114:17062–17067, 2010.

[146] Y. Liu, X. Wang, and C. B. Ching. Toward further understanding of lysozyme crystallization: Phase diagram, protein-protein interaction, nucleation kinetics, and growth kinetics. *Crystal Growth & Design*, 10(2):548–558, 2010.

[147] F. Sciortino, S. Mossa, E. Zaccarelli, and P. Tartaglia. Equilibrium cluster phases and low-density arrested disordered states: the role of short-range attraction and long-range repulsion. *Phys. Rev. Lett.*, 93:055701, 2004.

[148] S. B. Hutchens and Z.-G. Wang. Metastable cluster intermediates in the condensation of charged macromolecule solutions. *J. Chem. Phys.*, 127(8):084912, 2007.

[149] R. B. Jadrich, J. A. Bollinger, B. A. Lindquist, and T. M. Truskett. Equilibrium cluster fluids: Pair interactions via inverse design. *Soft Matter*, 11:9342–9354, 2015.

[150] W. Häußler, A. Wilk, J. Gapinski, and A. Patkowski. Interparticle correlations due to electrostatic interactions: a small angle X-ray and dynamic light scattering study. I. Apoferritin. *J. Chem. Phys.*, 117:413, 2002.

[151] W. Häußler. Neutron spin echo studies on ferritin: Free-particle diffusion and interacting solutions. *Eur. Biophys. J.*, 37:563–571, 2008.

[152] F. Roosen-Runge, M. Hennig, T. Seydel, F. Zhang, M. W. A. Skoda, S. Zorn, R. M. J. Jacobs, M. Maccarini, P. Fouquet, and F. Schreiber. Protein diffusion in crowded electrolyte solutions. *BBA Proteins*, 1804:68–75, 2010.

[153] J. C. Lee and S. N. Timasheff. Partial specific volumes and interactions with solvent components of proteins in guanidine hydrochloride. *Biochemistry*, 13:257–265, 1974.

[154] M. Grimaldo, F. Roosen-Runge, F. Zhang, T. Seydel, and F. Schreiber. Diffusion and dynamics of γ-globulin in crowded aqueous solutions. *J. Phys. Chem. B*, 118:7203–7209, 2014.

[155] F. Roosen-Runge, M. Hennig, F. Zhang, R. M. J. Jacobs, M. Sztucki, H. Schober, T. Seydel, and F. Schreiber. Protein self-diffusion in crowded solutions. *Proc. Natl. Acad. Sci. U.S.A.*, 108(29):11815–11820, 2011.

[156] A. Ortega, D. Amorós, and J. García de la Torre. Prediction of hydrodynamic and other solution properties of rigid proteins from atomic- and residue-level models. *Biophys. J.*, 101:892–898, 2011.

[157] R. Piazza and S. Iacopini. Transient clustering in a protein solution. *Eur. Phys. J. E*, 7(1):45–48, 2002.

[158] C. Le Bon, T. Nicolai, and D. Durand. Kinetics of aggregation and gelation of globular proteins after heat-induced denaturation. *Macromolecules*, 32(19):6120–6127, 1999.

[159] M. Verheul, J. S. Pedersen, S. P. F. M. Roefs, and K. G. de Kruif. Association behavior of native β-lactoglobulin. *Biopolymers*, 49(1):11–20, 1999.

[160] U. M. Elofsson, M. A. Paulsson, and T. Arnebrant. Adsorption of β-lactoglobulin A and B in relation to self-association: Effect of concentration and pH. *Langmuir*, 13(6):1695–1700, 1997.

[161] B. Farago, P. Falus, I. Hoffmann, M. Gradzielski, F. Thomas, and C. Gomez. The IN15 upgrade. *Neutron News*, 26(3):15–17, 2015.

[162] B. Frick, E. Mamontov, L. van Eijck, and T. Seydel. Recent backscattering instrument developments at the ILL and SNS. *Z. Phys. Chem.*, 224:33–60, 2010.

[163] M. Hennig, B. Frick, and T. Seydel. Optimum velocity of a phase-space transformer for cold-neutron backscattering spectroscopy. *J. Appl. Crystallogr.*, 44(3):467–472, 2011.

[164] M. Tokuyama and I. Oppenheim. Dynamics of hard-sphere suspensions. *Phys. Rev. E*, 50:R16–R19, 1994.

[165] A. J. Banchio and G. Nägele. Short-time transport properties in dense suspensions: from neutral to charge-stabilized colloidal spheres. *J. Chem. Phys.*, 128(10):104903, 2008.

[166] W. Schärtl. *Light scattering from polymer solutions and nanoparticle dispersions*. Springer, 2007.

[167] F. Schreiber. *Lecture notes on Grundlagen der Röntgen- und Neutronenbeugung*. Max-Planck-Institute Stuttgart.

[168] M. K. Braun, M. Wolf, O. Matsarskaia, S. Da Vela, F. Roosen-Runge, M. Sztucki, R. Roth, F. Zhang, and F. Schreiber. Strong isotope effects on effective interactions and phase behavior in protein solutions in the presence of multivalent ions. *J. Phys. Chem. B*, 121:1731–1739, 2017.

[169] J.-P. Hansen and I. R. McDonald. *Theory of Simple Liquids*. Academic Press Amsterdam, 3rd edition, 2006.

[170] Y. Zhang and P. S. Cremer. Interactions between macromolecules and ions: the Hofmeister series. *Curr. Opin. Chem. Biol.*, 10:658–663, 2006.

[171] J. M. Fox, K. Kang, W. Sherman, A. Héroux, G. M. Sastry, M. Baghbanzadeh, M. R. Lockett, and G. M. Whitesides. Interactions between Hofmeister anions and the binding pocket of a protein. *J. Am. Chem. Soc.*, 137:3859–3866, 2015.

[172] Y. Zhang and P. S. Cremer. Chemistry of Hofmeister anions and osmolytes. *Annu. Rev. Phys. Chem.*, 61:63–83, 2010.

[173] M. R. Fries, D. Stopper, M. K. Braun, A. Hinderhofer, F. Zhang, R. M. J. Jacobs, M. W. A. Skoda, H. Hansen-Goos, R. Roth, and F. Schreiber. Multivalent-ion-activated protein adsorption reflecting bulk reentrant behavior. *Phys. Rev. Lett.*, 119:228001, 2017.

[174] L. A. Feigin and D. I. Svergun. *Structure Analysis by Small-Angle X-Ray and Neutron Scattering.* Plenum Press, New York, 1987.

[175] J. Israelachvili. *Intermolecular and Surface Forces.* Academic Press, London, 1991.

[176] D. Svergun, C. Barberato, and M. H. J. Koch. *CRYSOL* – a program to evaluate X-ray solution scattering of biological macromolecules from atomic coordinates. *J. Appl. Crystallogr.*, 28(6):768–773, 1995.

[177] F. Zhang, F. Roosen-Runge, A. Sauter, R. Roth, M. W. A. Skoda, R. Jacobs, M. Sztucki, and F. Schreiber. The role of cluster formation and metastable liquid-liquid phase separation in protein crystallization. *Faraday Discuss.*, 159:313–325, 2012.

[178] H. J. C. Berendsen, D. van der Spoel, and R. van Drunen. GROMACS: a message-passing parallel molecular dynamics implementation. *Computer Physics Communications*, 91:43–56, 1995.

List of Own Publications

The publications this thesis is based on are marked with **[A]**-**[D]**.

[A] M. K. Braun, M. Wolf, O. Matsarskaia, S. Da Vela, F. Roosen-Runge, M. Sztucki, R. Roth, F. Zhang and F. Schreiber.
Strong Isotope Effects on Effective Interaction and Phase Behavior in Protein Solutions in the Presence of Multivalent Ions.
J. Phys. Chem. B **121** (2017), 1731–1739.

[B] M. K. Braun, M. Grimaldo, F. Roosen-Runge, I. Hoffmann, O. Czakkel, M. Sztucki, F. Zhang, F. Schreiber and T. Seydel
Crowding-Controlled Cluster Size in Concentrated Aqueous Protein Solutions: Structure, Self- and Collective Diffusion.
J. Phys. Chem. Lett. **8** (2017), 2590–2596.

[C] M. K. Braun, R. Schweins, T. Seydel, M. Sztucki, F. Zhang and F. Schreiber.
Effective Interactions, Collective Diffusion and Cluster Formation in Protein Solutions in the Presence of Trivalent Salts.
In preparation.

[D] M. K. Braun, A. Sauter, M. Sztucki, F. Zhang and F. Schreiber.
Reentrant Phase Behavior in Protein Solutions Induced by Multivalent Salts: Effect of Anions Cl^- versus NO_3^-.
In preparation.

- M. R. Fries, D. Stopper, M. K. Braun, A. Hinderhofer, F. Zhang, R. M. J. Jacobs, M. W. A. Skoda, H. Hansen-Goos, R. Roth and F. Schreiber.
  Multivalent-Ion-Activated Protein Adsorption Reflecting Bulk Reentrant Behavior.
  Phys. Rev. Lett. **119** (2017), 228001.

- S. Da Vela, M. K. Braun, A. Dörr, A. Greco, J. Möller, Z. Fu, F. Zhang, and F. Schreiber.
  Kinetics of liquid-liquid phase separation in protein solutions exhibiting LCST phase behavior studied by time-resolved USAXS and VSANS.
  Soft Matter **12** (2016), 9334–9341.

- O. Matsarskaia, M. K. Braun, F. Roosen-Runge, M. Wolf, F. Zhang, R. Roth and F. Schreiber.
  Cation-Induced Hydration Effects Cause Lower Critical Solution Temperature Behavior in Protein Solutions.
  J. Phys. Chem. B **120** (2016), 7731–7736.

Acknowledgment

I thank my supervisors Prof. Dr. Frank Schreiber and PD Dr. Fajun Zhang for their support and advice during my time as a PhD student. To Prof. Dr. Frank Schreiber, PD Dr. Fajun Zhang, Dr. Tilo Seydel, Dr. Felix Roosen-Runge, Prof. Dr. Martin Oettel and Prof. Dr. Roland Roth I am grateful for many helpful scientific discussions. Dr. Marco Grimaldo, Olga Matsarskaia and Dr. Stefano Da Vela as well as all other group members in Tübingen and in Grenoble I thank for scientific discussions as well and for being the good colleagues they were. Christian Beck, Dr. Marco Grimaldo and Olga Matsarskaia proofread the basics and experimental chapters as well as the introduction. Dr. Marco Grimaldo especially helped me to structure the sections on neutron backscattering and on neutron-spin-echo in the chapter on basic principles of small angle scattering and spectroscopy. I thank Pinelopi Christodoulou, Niels Scheffzyk and Simon Schoenberg who helped with the work in the lab. Klaus-Hagdorn Wittern, Bernd Hofferberth and Ralf Zenke provided technical assistance. Hanna Maurer and Aleksandra Rötschke helped with the administrative and organizational work. Finally, I thank the instrument and laboratory responsibles at the ILL and the ESRF, especially Dr. Tilo Seydel (IN16B), Dr. David Hess (ILL chemistry labs), Dr. Ralf Schweins (ALV SLS and DLS device at the ILL), Dr. Gudrun Lotze, Dr. Michael Sztucki and Dr. Theyencheri Narayanan (ID02 at the ESRF).